

Key factors determining nightside energetic electron losses driven by whistler-mode waves

Ethan Tsai¹, Anton V Artemyev², Qianli Ma³, Didier Mourenas⁴, Oleksiy Agapitov⁵, Xiao-Jia Zhang⁶, and Vassilis Angelopoulos³

¹UCLA

²UCLA IGPP

³University of California Los Angeles

⁴CEA

⁵Space Science Laboratory, UC Berkeley

⁶The University of Texas at Dallas

December 9, 2023

Abstract

Energetic electron losses by pitch-angle scattering and precipitation to the atmosphere from the radiation belts are controlled, to a great extent, by resonant wave particle interactions with whistler-mode waves. The efficacy of such precipitation is primarily controlled by wave intensity, although its relative importance, compared to other wave and plasma parameters, remains unclear. Precipitation spectra from the low-altitude, polar-orbiting ELFIN mission have previously been demonstrated to be consistent with energetic precipitation modeling derived from empirical models of field-aligned wave power across a wide-swath of local-time sectors. However, such modeling could not explain the intense, relativistic electron precipitation observed on the nightside. Therefore, this study aims to additionally consider the contributions of three modifications – wave obliquity, frequency spectrum, and local plasma density – to explain this discrepancy on the nightside. By incorporating these effects into both test particle simulations and quasi-linear diffusion modeling, we find that realistic implementations of each individual modification result in only slight changes to the electron precipitation spectrum. However, these modifications, when combined, enable more accurate modeling of ELFIN-observed spectra. In particular, a significant reduction in plasma density enables lower frequency waves, oblique, or even quasi-field aligned waves to resonate with near ~ 1 MeV electrons closer to the equator. We demonstrate that the levels of modification required to accurately reproduce the nightside spectra of whistler-mode wave-driven relativistic electron precipitation match empirical expectations, and should therefore be included in future radiation belt modeling.

Key factors determining nightside energetic electron losses driven by whistler-mode waves

Ethan Tsai¹, Anton Artemyev¹, Qianli Ma^{2,3}, Didier Mourenas^{4,5}, Oleksiy Agapitov⁶, Xiao-Jia Zhang^{7,1}, Vassilis Angelopoulos¹

¹Earth, Planetary, and Space Sciences, University of California, Los Angeles, Los Angeles, CA 90095, USA

²Department of Atmospheric and Oceanic Sciences, University of California, Los Angeles, Los Angeles, USA

³Boston University, Boston, MA, United States

⁴CEA, DAM, DIF, Arpajon, France

⁵Laboratoire Matière en Conditions Extrêmes, Paris-Saclay University, CEA, Bruyères-le-Châtel, France

⁶Space Sciences Laboratory, University of California, Berkeley, CA, USA

⁷Department of Physics, The University of Texas at Dallas, Richardson, TX, USA

Key Points:

- Comparing ELFIN data with test particle and quasi-linear simulations, we investigate whistler-driven electron precipitation on the nightside
- A reduction in background plasma density is key to enabling whistler-mode waves to efficiently scatter electrons up to 1 MeV
- Decreasing wave frequency as a function of latitude and wave obliquity, are both integral to capturing realistic nightside electron losses

Corresponding author: Ethan Tsai, ethantsai@ucla.edu

Abstract

Energetic electron losses by pitch-angle scattering and precipitation to the atmosphere from the radiation belts are controlled, to a great extent, by resonant wave particle interactions with whistler-mode waves. The efficacy of such precipitation is primarily controlled by wave intensity, although its relative importance, compared to other wave and plasma parameters, remains unclear. Precipitation spectra from the low-altitude, polar-orbiting ELFİN mission have previously been demonstrated to be consistent with energetic precipitation modeling derived from empirical models of field-aligned wave power across a wide-swath of local-time sectors. However, such modeling could not explain the intense, relativistic electron precipitation observed on the nightside. Therefore, this study aims to additionally consider the contributions of three modifications – wave obliquity, frequency spectrum, and local plasma density – to explain this discrepancy on the nightside. By incorporating these effects into both test particle simulations and quasi-linear diffusion modeling, we find that realistic implementations of each individual modification result in only slight changes to the electron precipitation spectrum. However, these modifications, when combined, enable more accurate modeling of ELFİN-observed spectra. In particular, a significant reduction in plasma density enables lower frequency waves, oblique, or even quasi-field aligned waves to resonate with near ~ 1 MeV electrons closer to the equator. We demonstrate that the levels of modification required to accurately reproduce the nightside spectra of whistler-mode wave-driven relativistic electron precipitation match empirical expectations, and should therefore be included in future radiation belt modeling.

Plain Language Summary

Whistler-mode waves are a type of electromagnetic wave that mediate electron dynamics in Earth’s radiation belts and are simultaneously important for energizing electrons and driving loss mechanisms. Most radiation belt models today do not adequately capture the effects of these waves on relativistic electrons, which are important to study because these energetic electrons are often called “Killer Electrons” for their ability to degrade spacecraft electronics. Additionally, when lost into Earth’s atmosphere, these electrons can also change atmospheric chemistry and ionospheric properties, making them an important input parameters for atmospheric, ionospheric, and magnetospheric modeling. This study uses two different modeling methods to determine which properties of whistler-mode waves are most important for accurately capturing these wave-particle interactions on the nightside, where plasma interactions are more dynamic. The results agree well with statistical results from the Electron Losses and Fields INvestigation (ELFİN) mission, allowing us to fully explain the mechanisms behind whistler-mode wave-driven electron losses on the nightside.

1 Introduction

Earth’s inner magnetosphere is filled with energetic electron fluxes injected from the plasma sheet, that are then further accelerated via resonant interactions with electromagnetic whistler-mode (chorus) waves (Millan & Baker, 2012; Shprits et al., 2008). These wave-particle interactions are, in great part, also responsible for energetic electron pitch-angle scattering into the loss cone and subsequent electron loss through precipitation into Earth’s atmosphere (Millan & Thorne, 2007; Shprits et al., 2008). This contribution to both acceleration and pitch-angle scattering of energetic electrons makes the whistler-mode wave a crucial element of outer radiation belt dynamics (Bortnik & Thorne, 2007; Thorne, 2010; Li & Hudson, 2019). Not only do energetic radiation belt electrons serve as an important space weather proxy (Horne et al., 2013), relativistic electron can also penetrate deep into the thermosphere/mesosphere (Xu et al., 2020) contributing to ozone depletion (Thorne, 1980; Lam et al., 2010; Turunen et al., 2016). Un-

71 understanding the mechanisms behind the global distribution of energetic electron losses
72 is therefore important for studying radiation belt dynamics and atmospheric chemistry.

73 Energetic ($\gtrsim 100$ keV) electron losses due to whistler-mode waves is one such topic
74 that has yet to be fully investigated. It is known that these waves can scatter electrons
75 up to 1 MeV (O’Brien et al., 2004; Thorne et al., 2005; Blake & O’Brien, 2016; Shumko
76 et al., 2018; Breneman et al., 2017), which is problematic because current radiation belt
77 models typically only incorporate diffusive losses of sub-relativistic electrons (up to \sim
78 500 keV). Additionally, previous research (Tsai et al., 2023) has revealed a day-night dif-
79 ference in energetic electrons scattered by whistler-mode waves, with more intense elec-
80 tron precipitation on the dayside than on the nightside. This is attributed to two system-
81 level properties – (1) nightside regions generally have a lower plasma density and (2) night-
82 side wave activity is generally more confined to the equatorial plane (Meredith et al., 2001,
83 2003; Agapitov et al., 2013) – which both cause strong resonant wave particle interac-
84 tions to preferentially occur on the dayside, resulting in more extreme energetic electron
85 losses (e.g., Thorne et al., 2005; Mourenas, Artemyev, Agapitov, & Krasnoselskikh, 2014;
86 Wang & Shprits, 2019; Aryan et al., 2020). This is supported by Tsai et al. (2023), which
87 used modeled electron precipitation spectra derived from statistically-averaged wave in-
88 tensity distributions from Agapitov et al. (2018) to directly compare with statistical ob-
89 servations of electron precipitating fluxes from ELFIND (Angelopoulos et al., 2020). Al-
90 though these model-data comparisons showed good agreement between electron precipi-
91 tation and wave power in the dusk and daysides, ELFIND-measured nightside relativistic
92 ($\gtrsim 500$ keV) precipitating flux rates were substantially larger than anticipated (i.e.
93 modeled) and nearly comparable to that on the dayside. Understanding mechanisms that
94 can cause such intense energetic precipitation is a prerequisite for accurately modeling
95 electron loss in the radiation belts, therefore motivating the need to explore what key
96 factors actually determine nightside electron losses.

97 There are a few prime candidates that determine the efficiency of wave-particle res-
98 onant interactions (and, particularly, the energy dependence of whistler-mode wave driven
99 electron scattering):

- 100 1. Wave intensity distribution along magnetic field lines (see discussion in Thorne
101 et al., 2005; Wang & Shprits, 2019).
- 102 2. Obliquity of wave propagation relative to the background magnetic field (see dis-
103 cussion in Lorentzen et al., 2001; Mourenas, Artemyev, Agapitov, & Krasnosel-
104 skikh, 2014; Artemyev et al., 2016).
- 105 3. Wave frequency spectrum and its variation along magnetic field lines (see discus-
106 sion in Agapitov et al., 2018)
- 107 4. Equatorial plasma density magnitude (see discussion in Thorne et al., 2013; Agapi-
108 tov et al., 2019; Allison & Shprits, 2020) and its variation along magnetic field lines
109 (see discussion in Summers & Ni, 2008; Artemyev et al., 2013).

110 Having already examined the importance of wave amplitude in Tsai et al. (2023), we now
111 study the remaining three mechanisms which could potentially modulate nightside elec-
112 tron precipitating spectra. First, intense nightside whistler-mode waves are typically as-
113 sociated with strong plasma sheet injections (Tao et al., 2011; Fu et al., 2014; X. Zhang
114 et al., 2018) which are often accompanied by the enhanced convection electric field which
115 transports cold plasma Earthward, thereby decreasing equatorial plasma density (Vasko,
116 Agapitov, Mozer, Bonnell, et al., 2017; Agapitov et al., 2019). A lower plasma density
117 results in a lower plasma frequency; a lower plasma frequency to gyrofrequency ratio,
118 f_{pe}/f_{ce} yields a higher cyclotron resonance energy $E_R \propto (f_{ce}/f_{pe})^2$ to f_{ce}/f_{pe} (from
119 low to high energy) of electrons for given wave frequencies, wave normal angles, and elec-
120 tron pitch-angles (Stix, 1962; Summers et al., 2007; Li, Thorne, Nishimura, et al., 2010;
121 Allison et al., 2021). This nightside localized density reduction can thus potentially in-
122 crease the scattering rate of relativistic electrons.

123 Second, statistical observations have shown a clear trend of average wave frequency
 124 decreasing with latitude along field lines (i.e. increasing distance from the equatorial plane)
 125 (Agapitov et al., 2018). This is likely caused by preferential Landau damping of higher-
 126 frequency waves resonating with suprathermal electrons (L. Chen et al., 2013; Watt et
 127 al., 2013; Maxworth & Golkowski, 2017). A lower normalized wave frequency f/f_{ce} means
 128 a higher cyclotron resonance energy $E_R \propto (f_{ce}/f)(1-f/f_{ce})^3$ to $(f_{ce}/f)^{1/2}(1-f/f_{ce})^{3/2}$
 129 from low to high energy (Li, Thorne, Nishimura, et al., 2010; Mourenas et al., 2012). Thus,
 130 this reduction in the mean wave frequency in the nightside off-equatorial region may also
 131 increase the scattering rate of relativistic electrons.

132 Third, plasma injections are often associated with enhanced electrostatic turbu-
 133 lence (Mozer et al., 2015; Agapitov et al., 2015; Vasko, Agapitov, Mozer, Artemyev, et
 134 al., 2017; Malaspina et al., 2018) that forms a plateau in the field-aligned velocity distri-
 135 bution and significantly reduces Landau damping of oblique whistler-mode waves (see
 136 discussion in Mourenas et al., 2015; Ma et al., 2017; Artemyev & Mourenas, 2020). In
 137 this regime, oblique (with wave normal angles below the Gendrin angle $\theta_G \approx \text{acos}(2f/f_{ce})$)
 138 and very oblique (with wave normal angle up to the resonant cone angle $\theta_r \approx \text{acos}(f/f_{ce})$)
 139 waves may survive Landau damping (see Min et al., 2014; R. Chen et al., 2019; Sauer
 140 et al., 2020; Ke et al., 2022). These waves then become oblique off the equatorial plane
 141 (Bortnik et al., 2007; L. Chen et al., 2013), or, in more unusual cases, are generated within
 142 the equatorial source region (Artemyev et al., 2016; Li, Mourenas, et al., 2016; Agapi-
 143 tov et al., 2016). Wave obliquity not only increases the resonant interaction energy with
 144 electrons as $E_R \propto 1/k_{\parallel}^2 \propto 1/\cos^2\theta$ (e.g., Verkhoglyadova et al., 2010; Mourenas et
 145 al., 2015), but also allows for interactions with electrons at higher-order cyclotron res-
 146 onances ($n \gg 1$, e.g., Shklyar & Matsumoto, 2009; Mourenas et al., 2012; Artemyev
 147 et al., 2013; Albert, 2017) which can drastically increase the resonance energy $E_R \propto n^2$
 148 (e.g., Lorentzen et al., 2001; Gan et al., 2023). Thus, nightside whistler-mode wave obli-
 149 quity could also potentially increase the scattering rate of relativistic electrons.

150 Here, we examine each of these three mechanisms to see whether they can explain
 151 the enhanced precipitation of relativistic electrons in the nightside MLT sector using a
 152 combination of statistics from ELFIN observations (Angelopoulos et al., 2020), test par-
 153 ticle simulations (Tsai et al., 2022, 2023), and quasi-linear diffusion code (Ma et al., 2012,
 154 2015). This paper is organized as follows: Section 2 details ELFIN observations/statistics
 155 and presents observational evidence of intense nightside precipitation of relativistic elec-
 156 trons; Section 3 describes the basics of the test particle simulation and quasi-linear dif-
 157 fusion codes; Section 4 compares ELFIN data to results from a variety of runs explor-
 158 ing the three main modifications – reduced plasma density, wave obliquity, wave frequency
 159 variation along magnetic field lines; finally, Section 5 summarizes and discusses the ob-
 160 tained results.

161 2 Data Sets

162 The ELFIN CubeSats (ELFIN A and B) are identically equipped with an Ener-
 163 getic Particle Detector for Electrons (EPDE), capable of measuring energy and pitch-
 164 angle distributions of energetic electrons with $\Delta E/E = 40\%$ across 16 logarithmically
 165 spaced energy channels between 50 keV and 5 MeV (Angelopoulos et al., 2020). Spin-
 166 ning at just over 21 revolutions per minute (spin period ≈ 2.8 sec), ELFIN’s 16 sectors
 167 per spin yields a spin phase resolution of $\Delta\alpha = 22.5^\circ$. The main data product used in
 168 this study is the precipitating-to-trapped flux ratio, $j_{prec}/j_{trap}(E)$, where $j_{trap}(E)$ is the
 169 locally trapped (outside of the local bounce loss-cone) electron flux and $j_{prec}(E)$ is the
 170 flux integrated over the local loss-cone with a correction to remove the backscattered fluxes
 171 from the opposite hemisphere (see details in Mourenas et al., 2021; Angelopoulos et al.,
 172 2023). Figure 1 shows two typical examples of ELFIN outer radiation belt crossings on
 173 the nightside with $j_{trap}(E)$ (a,d) and j_{prec}/j_{trap} (b,e) distributions.

174 This study utilized 30 months (January 2020 - June 2022) of ELFIN's $j_{trap}(E)$ and
 175 $j_{prec}(E)$ measurements during strong and bursty energetic electron precipitation events
 176 (for details regarding statistical coverage, see Figure 5 in Tsai et al., 2023). In order to
 177 obtain a statistical representation of whistler-mode-driven electron precipitation, data
 178 was selected based on data quality (minimum 4 counts/second for any given energy or
 179 pitch angle bin) and precipitation intensity ($j_{prec}(E)/j_{trap}(E) > 0.5$ at ELFIN's low-
 180 est energy bin of 63 keV). In addition, there were provisions to identify and remove elec-
 181 tron precipitation events driven by field-line curvature scattering, EMIC-driven precip-
 182 itation, and microbursts. Curvature scattering (Imhof et al., 1977; Sergeev et al., 1983;
 183 Büchner & Zelenyi, 1989) of plasma sheet and radiation belt electrons can be identified
 184 by its sharp energy/latitude dispersion (isotropy boundary) that results in high precipitating-
 185 to-trapped flux ratio at relativistic energies closer to the planet (see the IB precipitat-
 186 ing pattern in Fig. 1b and statistical results in Wilkins et al. (2023)). Such data, in ad-
 187 dition to the isotropic precipitation with $j_{prec}/j_{trap} \sim 1$ of < 300 keV electrons pole-
 188 ward from the isotropy boundary (Artemyev et al., 2022), are removed from our statis-
 189 tics. Next, electromagnetic ion cyclotron (EMIC) waves, which are caused by nightside
 190 ion injections (Jun et al., 2019; Kim et al., 2021) and efficiently scatter and precipitate
 191 relativistic electrons (e.g., Blum, Halford, et al., 2015; Blum, Li, & Denton, 2015; Yah-
 192 nin et al., 2016, 2017; Capannolo et al., 2019, 2023), are excluded. These EMIC-driven
 193 observations are identified by precipitating-to-trapped ratios that reach their peak at \geq
 194 500 keV energy (see examples in X. An et al., 2022; Grach et al., 2022; Capannolo et al.,
 195 2023; Angelopoulos et al., 2023). Additionally, whistler-mode hiss waves provide a wide
 196 energy range of scattering, from weak scattering further from the plasmasphere to pre-
 197 cipitation of relativistic electrons within the plasmasphere (see discussion of ELFIN ob-
 198 servations of such precipitation in Mourenas et al., 2021; Angelopoulos et al., 2023; X.-
 199 C. Shen et al., 2023); these hiss precipitation events are also eliminated. Figure 1e shows
 200 this particular pattern, which is recognizable by a low j_{prec}/j_{trap} ratio peaking at ≥ 500
 201 keV energy at low L -shells. Finally, we exclude all precipitation patterns showing microburst-
 202 like flux variation within one spin (such events are characterized by precipitating-to-trapped
 203 flux ratio exceeding one for relativistic electron energies, see X.-J. Zhang et al., 2022, for
 204 further examples).

205 All these effects are programmatically eliminated from statistics leaving us with
 206 only one type of precipitating energy distribution: a precipitating-to-trapped ratio mono-
 207 tonically decreasing with energy, observed primarily within L -shells $\in [4, 8]$, correspond-
 208 ing to the outer radiation belt outside the plasmasphere (e.g., Mourenas et al., 2021).
 209 This type of precipitation can only be caused by whistler-mode waves (see more details
 210 and examples in Tsai et al., 2022; X.-J. Zhang et al., 2022, 2023), and is demonstrated
 211 in Figure 1(b,e).

212 We combine all ELFIN observations from the nightside MLT sector (27950 spins
 213 across 4458 radiation belt crossings) and plot the averaged precipitating-to-trapped flux
 214 spectra for three geomagnetic activity levels and two L -shell domains (4.5–5.5 and 5.5–
 215 7.5) for $AE \in [100, 300]$ nT in Fig. 2d. Fig. 2(a-c) show that the precipitating-to-trapped
 216 electron flux ratio j_{prec}/j_{trap} above 100 keV increases significantly as AE increases. The
 217 precipitating-to-trapped flux ratio reaches $j_{prec}/j_{trap} \sim 0.1$ up to 200–400 keV when
 218 $AE > 300$ nT. This result is consistent with past observations of stronger energetic elec-
 219 tron injections from the plasma sheet during periods of higher AE (Tao et al., 2011; Runov
 220 et al., 2015; Gabrielse et al., 2014), leading to even more intense whistler-mode waves
 221 (Meredith et al., 2001; X. J. Zhang et al., 2018) which can efficiently precipitate 50 –
 222 500 keV electrons (Summers et al., 2004; Thorne et al., 2005; Aryan et al., 2020; Agapi-
 223 tov et al., 2018). The ratio j_{prec}/j_{trap} is also higher at $L = 5.5–7.5$ than at $L = 4.5–$
 224 5.5 in Fig. 2, in agreement with the higher chorus wave power at higher $L > 5.0–5.5$
 225 in the night sector in spacecraft statistics (Agapitov et al., 2018; Meredith et al., 2020).
 226 The smooth decrease of j_{prec}/j_{trap} as electron energy increases in Fig. 2d is consistent
 227 with the expectation that at higher latitudes, wave power decreases while minimum cy-

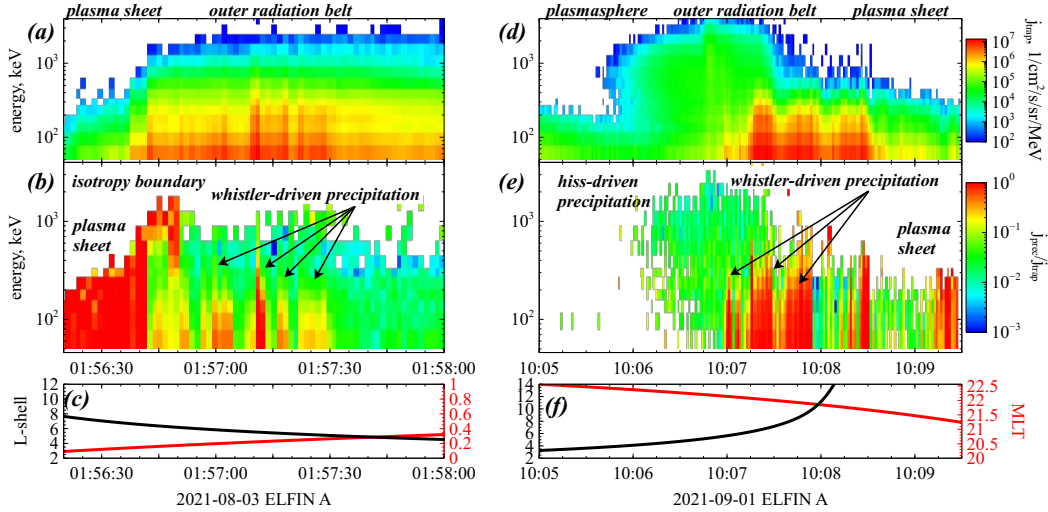


Figure 1. Two examples of ELFIN observations with strong precipitation of energetic electrons in the nightside MLT sector showing locally trapped electron fluxes (a,d), precipitating-to-trapped flux ratio (b,e), and ELFIN’s MLT, L -shell coordinates from (Tsyganenko, 1989) model (c,f).

228 electron resonance energy increases, therefore precipitating higher energy electrons at lower
 229 absolute flux levels (Agapitov et al., 2018; Meredith et al., 2020).

230 3 Simulation

231 Calculating the precipitating-to-trapped flux ratios is useful because it eliminates
 232 the trapped flux variability (which can vary by orders of magnitude). The slope of the
 233 ratio’s energy spectra now represents only the relative effects of resonant interactions with
 234 whistler-mode waves. To then compare with ELFIN statistics, we obtain modeled precipitating-
 235 to-trapped flux ratios using two different types of simulations: (1) a configurable large-
 236 ensemble test particle simulation for electron resonant interactions, as used in previous
 237 work (Tsai et al., 2022, 2023) and (2) a quasi-linear diffusion code which has been used
 238 in previous radiation belt simulations (Ma et al., 2012, 2015). The test particle simu-
 239 lations include potential non-linear resonant effects and consider only purely monochro-
 240 matic waves, whereas the quasi-linear diffusion code models electron scattering by an en-
 241 semble of oblique waves with higher order resonant interactions across a distribution of
 242 frequencies. Thus, by comparing results obtained by these two approaches, we can fully
 243 capture the importance of different resonant effects for electron scattering and losses.

244 3.1 Test particle simulation

245 Our test particle simulation (Tsai et al., 2022, 2023) is designed to compute the
 246 expected energy distribution of the electron precipitation flux ratio given realistic wave
 247 parameters. In order to obtain enough statistics – especially at higher energies where
 248 it is less likely for electrons to be scattered into the loss cone – we use a large number
 249 of particles for all test particle simulations in this study with $N = 5 \times 10^6$. For this
 250 to run in a reasonable amount of time, we parallelize the code and implement it in Ju-
 251 lia 1.9.3 (Bezanson et al., 2017) using the differential equations package (Rackauckas &
 252 Nie, 2017). The Hamiltonian formulation for wave-particle resonant interactions (Albert
 253 et al., 2013; Vainchtein et al., 2018) incorporates nonlinear effects such as phase bunch-

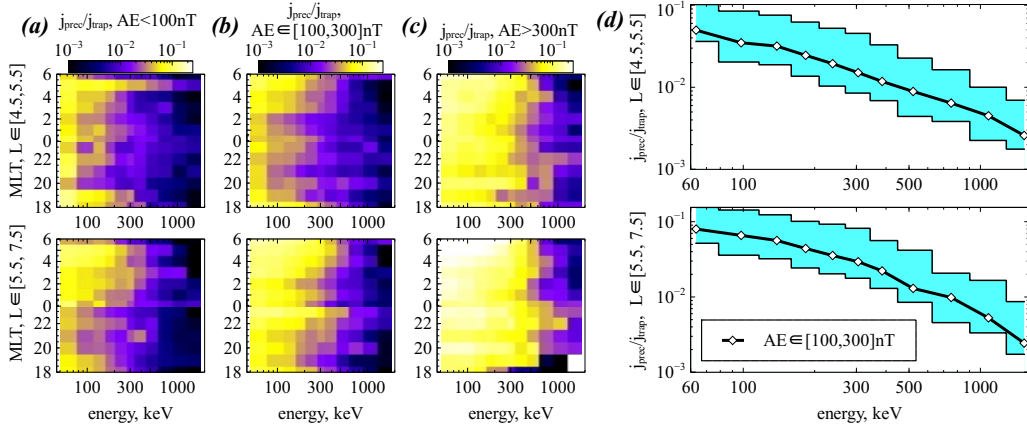


Figure 2. Plots (a-c) show the statistical distributions of precipitating-to-trapped electron spectra in (MLT, energy) space for several levels of geomagnetic activity. Plots (d) show energy profiles of precipitating-to-trapped fluxes for three geomagnetic activity levels in the nightside MLT $\in [18, 4]$. The shaded blue range regions represent the upper ($AE > 300$ nT) and lower ($AE < 100$ nT) bounds of geomagnetic activity levels while the central black curve depicts $AE \in [100, 300]$ nT.

254 ing, phase trapping, and anomalous trapping (Demekhov et al., 2006; Bortnik et al., 2008;
 255 Katoh et al., 2008; Omura et al., 2007; Kitahara & Katoh, 2019; Albert et al., 2021). The
 256 simulation uses monochromatic waves, which is generally valid for describing diffusive
 257 scattering in a background dipolar magnetic field due to its strong magnetic field gra-
 258 dient (Albert, 2001, 2010; Shklyar, 2021). Critically, the wave field is modified by the
 259 function $B_w(\lambda, L, \text{MLT}, Kp)$ which describes the wave amplitude variation along mag-
 260 netic field lines using an empirical chorus wave model built using 14 years of Cluster and
 261 Van Allen Probe statistics. The wave model is dependent on latitude, geographic loca-
 262 tion, and geomagnetic activity (see model and coefficients in Agapitov et al., 2018), which
 263 is necessary for realistic modeling of energetic electron losses. Further details of the test
 264 particle simulation implementation can be found in Tsai et al. (2022, 2023).

265 In this study, we have further augmented the test particle simulation to explore the
 266 latitudinal dependence of wave frequency and obliquity so that wave frequency $\omega(\lambda, \theta)$
 267 is a function of both latitude and wave normal angle. Changing into dimensionless vari-
 268 ables allows us to provide a mean normalized wave frequency $\omega_m(\lambda) = \omega(\lambda)/\Omega_{ce,eq}$ and
 269 mean wave normal angle $\theta(\lambda)$ both as functions of magnetic latitude λ (as described in
 270 Section 3.3). With dimensionless variables, the normalized plasma frequency is defined
 271 as $\Omega_{pe} = \omega_{pe,eq}/\Omega_{ce,eq}$.

272 3.2 Quasi-linear diffusion code

273 To instill further confidence in test particle simulation results, we calculate the quasi-
 274 linear diffusion coefficients using the Full Diffusion Code (Ni et al., 2008, 2011; Shprits
 275 & Ni, 2009; Ma et al., 2018) and model the precipitating electron flux using the Fokker-
 276 Planck diffusion code (Ma et al., 2012, 2015). This quasi-linear diffusion code physically
 277 differs from the test particle simulations primarily in the fact that it prescribes Gaus-
 278 sian distributions for the wave frequency (Glauert & Horne, 2005):

$$\hat{B}^2(\omega) \sim \exp\left[-\frac{(\omega - \omega_m(\lambda))^2}{\delta\omega^2}\right]$$

279 and the wave normal angle:

$$g(\theta) \sim \exp \left[-\frac{(\tan \theta - \tan \theta_m(\lambda))^2}{(\tan \delta\theta)^2} \right]$$

280 where mean values ω_m and θ_m with bandwidths $\delta\omega$ and $\delta\theta$ represent wave frequency and
 281 normal angle, respectively. These distributions are provided relative to mean values, $\omega_m(\lambda)$
 282 and $\theta_m(\lambda)$, which are given as functions of magnetic latitude λ and discussed in the next
 283 section (see details in Artemyev et al., 2013; Agapitov et al., 2018; Aryan et al., 2020).

284 We use the bounce-averaged Fokker-Planck equation to model the electron precip-
 285 itation rate (Lyons et al., 1972; Glauert & Horne, 2005):

$$\frac{\partial f}{\partial t} = \frac{1}{\tau_b(\alpha_{eq}) \sin 2\alpha_{eq}} \frac{\partial}{\partial \alpha_{eq}} \left(\tau_b(\alpha_{eq}) \sin 2\alpha_{eq} \left(\langle D_{\alpha\alpha} \rangle \frac{\partial f}{\partial \alpha_{eq}} \right) \right) - \frac{f}{\tau_{loss}} \quad (1)$$

286 where α_{eq} is the equatorial pitch angle, $\tau_b \approx 1.38 - 0.32 (\sin \alpha_{eq} + \sin^2 \alpha_{eq})$ (see Orlova
 287 & Shprits, 2011), $\langle D_{\alpha\alpha} \rangle$ is the bounce-averaged diffusion rate, and $\tau_{loss}(t)$ is the bounce
 288 loss time (and is set to be a quarter of the bounce period inside the local loss-cone and
 289 infinity outside the loss cone). We use the quasi-linear diffusion code to numerically solve
 290 Eq. (1), with diffusion rates derived from $\hat{B}^2(\omega)$ and $g(\theta)$ distributions (see Ni et al.,
 291 2008, 2011; Ma et al., 2015, 2018). Zero-gradient boundary conditions in pitch angle are
 292 set to simulate the loss cone filling of electrons due to wave scattering (Ma et al., 2022).

293 3.3 Frequency and Obliquity Models

294 In both simulations, we use the following two models to compare the effects of whistler
 295 wave frequency (normalized to the equatorial gyrofrequency) $\omega_m = \omega/\Omega_{ce,eq}$:

296 **Model 1:** normalized wave frequency held constant at $\omega_m = 0.35$, the typical frequency
 297 of whistler mode chorus waves near the equator (Agapitov et al., 2018).

298 **Model 2:** function $\omega(\lambda)$ linearly decreasing from $0.41\Omega_{ce,eq}$ at the equator until reach-
 299 ing a constant $0.16\Omega_{ce,eq}$ for $\lambda \geq 20^\circ$. This model is based on statistics of off-
 300 equatorial parallel and oblique lower-band chorus waves from the Van Allen Probes
 301 (Agapitov et al., 2018).

302 We use the following four models to describe the mean wave normal angle (WNA)
 303 θ_m . A scaling factor $\Theta(\lambda) = \lambda/(15^\circ + \lambda)$ is adopted to modify the WNA increase from
 304 0 at the equator to $\Theta(45^\circ) = 0.75$ at 45° latitude in WNA1 and WNA2.

305 **FAW:** a field-aligned wave model (with $\theta = 0^\circ$ in test particle simulations and $\theta_m =$
 306 0° , $\delta\theta = 30^\circ$ or $\delta\theta = 5^\circ$ in the quasi-linear diffusion code) that describes the
 307 most intense population of waves (Li, Santolik, et al., 2016; Agapitov et al., 2013)
 308 as they remain field-aligned off equator due to wave ducting by small-scale den-
 309 sity structures (Hanzelka & Santolik, 2019; Y. Shen et al., 2021; Ke et al., 2021;
 310 Hosseini et al., 2021).

311 **WNA1:** a moderately oblique WNA model with $\theta_1(\lambda) = \theta_G(\lambda) \cdot \Theta(\lambda)$, where $\theta_G =$
 312 $\arccos(2\omega/\Omega_{ce})$ is the Gendrin angle (Gendrin, 1961). This model describes field-
 313 aligned waves that are generated at the equator, but become mildly oblique as they
 314 propagate through the inhomogeneous plasma (e.g. Breuillard et al., 2012; L. Chen
 315 et al., 2013; Ke et al., 2017).

316 **WNA2:** a very oblique WNA model with $\theta_2(\lambda) = \theta_r(\lambda) \cdot \Theta(\lambda)$, where $\theta_r = \arccos(\omega/\Omega_{ce})$
 317 is the resonance cone angle. This describes field-aligned waves that are generated
 318 at the equator, but become very oblique as they propagate through the inhom-
 319 ogeneous plasma in the case of suppressed Landau damping (see discussion in Arte-
 320 myev & Mourenas, 2020).

321 **WNA3:** an extremely oblique WNA model with $\theta_3(\lambda) = \theta_r(\lambda) - 2^\circ$. This model de-
 322 scribes very oblique waves that are generated in the equatorial source region in
 323 the presence of field-aligned electron streams suppressing Landau damping (Mourenas
 324 et al., 2015; Li, Mourenas, et al., 2016; R. Chen et al., 2019; Kong et al., 2021).

325 The quasi-linear simulations also require a bandwidth parameter which sets the width
 326 of the wave frequency and normal angle Gaussian distributions, defined in Section 3.2.
 327 Frequency bandwidth $\delta\omega$ is set to 0.125, and the lower and upper cutoff frequencies are
 328 set to be $\omega_m - 2\delta\omega$ and 0.5, respectively. Wave normal angle bandwidth is set to either
 329 $\delta\theta = 5^\circ$ or $\delta\theta = 30^\circ$ for FAW, and $\delta\theta = 10^\circ$ for the other models; if $\theta_r(\lambda) - \theta_m(\lambda) <$
 330 20° , we set $\delta\theta = (\theta_r(\lambda) - \theta_m(\lambda))/2$. The lower (θ_{LC}) and upper (θ_{UC}) cutoff wave nor-
 331 mal angles are set as $\tan \theta_{LC} = \max(0, \tan \theta_m - 2 \tan \delta\theta)$ and $\tan \theta_{UC} = \min(\tan 89.9^\circ, \tan \theta_m +$
 332 $2 \tan \delta\theta)$, respectively.

333 Finally, the magnetic wave power distribution $B_w^2(\lambda)$ is taken from an empirical
 334 statistical model (Agapitov et al., 2018) at 23 MLT and $L = 6$ for $Kp = 3$. Note that
 335 we use $Kp = 3$ as a reasonable estimate of average geomagnetic activity level for ELFIN
 336 observations of electron precipitation driven by resonance with whistler-mode waves (see
 337 Tsai et al., 2023, for further discussion). For quiet conditions $Kp \leq 2$, the wave inten-
 338 sity provides insufficient levels of precipitating electron fluxes, which is generally corrob-
 339 orated by the extremely low levels (i.e. near background) of precipitating fluxes ELFIN
 340 observes during quiet periods. During disturbed storm times ($Kp > 4$), the precipitat-
 341 ing and locally trapped fluxes are occasionally too large and approach saturation of ELFIN's
 342 EPDE instrument (see details in X.-J. Zhang et al., 2022). Both types of ELFIN obser-
 343 vations (either background-level precipitation or nearly-saturated measurements) are ex-
 344 cluded from the statistical analysis.

345 4 Data-model comparison

346 In this section, the precipitating-to-trapped electron flux ratio j_{prec}/j_{trap} , calcu-
 347 lated through test particle simulations (TPS) or Quasi-Linear Diffusion Code (QLDC),
 348 are compared with j_{prec}/j_{trap} as measured by ELFIN. This allows us to assess the dif-
 349 ferent roles potentially played by plasma density, wave obliquity, and wave frequency based
 350 on precipitating flux ratio variation with energy.

351 For proper comparison, the simulated j_{prec}/j_{trap} flux ratio is normalized to the ob-
 352 served j_{prec}/j_{trap} flux ratio at ELFIN's second energy bin (~ 97 keV), thereby remov-
 353 ing wave amplitude variability such that the spectral slope can be compared for across
 354 various scenarios. This is valid because the $\sim 30 - 100$ keV precipitating-to-trapped
 355 electron flux ratio correlates well with the equatorial wave amplitude (Li et al., 2013; Ni
 356 et al., 2014). In addition, spurious variations in j_{prec}/j_{trap} modeled using our test par-
 357 ticle simulations tend to become larger below 97 keV, despite the large number of par-
 358 ticle runs per energy bin. These oscillations are absent from results of the quasi-linear
 359 diffusion code, which correlate well with test particle simulation results above 97 keV
 360 after normalization.

361 4.1 Role of plasma density

362 Figure 3 shows a comparison between the precipitating-to-trapped electron flux ratio
 363 j_{prec}/j_{trap} measured by ELFIN at $L > 5$ and 18-4 MLT (black) with j_{prec}/j_{trap} ob-
 364 tained from TPS (solid red) and QLDC (dashed red) with parallel (FAW model) lower-
 365 band chorus waves (adopting $\theta = 0^\circ$ in test particle simulations, $\delta\theta = 30^\circ$ in the quasi-
 366 linear diffusion code), using wave frequency Model 1 of constant frequency ($\omega_m = 0.35$)
 367 chorus waves and a typical plasma frequency to gyrofrequency ratio $\Omega_{pe} = 6.5$ at $L =$
 368 6.5 and 23 MLT (Sheeley et al., 2001). In this plot (and remaining Figures 3-7), the gray
 369 shaded regions of ELFIN data denote the boundaries of quiet (AE < 100 nT) and ac-

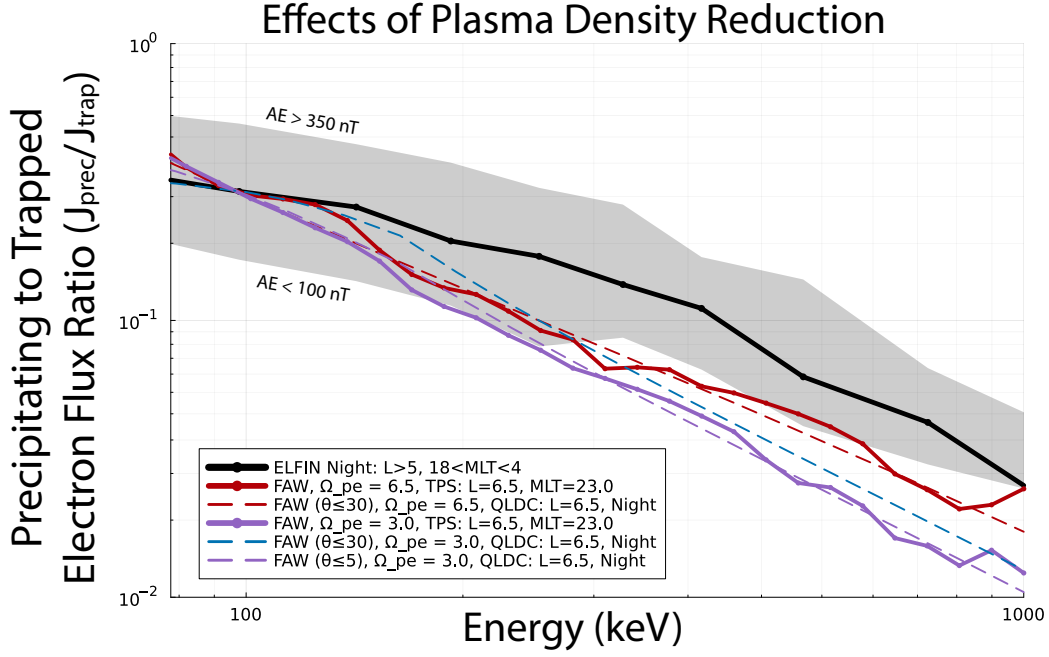


Figure 3. ELFIN-measured precipitating-to-trapped electron flux ratio at $L > 5$ on the night-side (18 – 4 MLT) as a function of energy (black curve). The corresponding j_{prec}/j_{trap} flux ratio obtained from test particle simulations is shown for parallel (FAW model, $\theta = 0^\circ$) lower-band chorus waves, using frequency Model 1 ($\omega_m = constant$) and a typical $\Omega_{pe} = 6.5$ at $L = 6.5$ and 23 MLT (solid red). Results from the quasi-linear diffusion code using the same parameters is shown in dashed red. Similarly, the cases of reduced density $\Omega_{pe} = 3$ modeled with test particle simulation (solid purple), quasi-linear diffusion code using narrow-band field aligned waves ($\delta\theta = 5^\circ$, dashed purple), and more quasi-linear field aligned waves ($\delta\theta = 30^\circ$, dashed blue), are shown. All simulation results are normalized to observations at 97 keV.

370 tive ($AE > 350$ nT) times. The normalized ratios j_{prec}/j_{trap} obtained from TPS and
 371 QLDC are quite similar (compare solid with dashed lines of the same color), validating
 372 the reliability of the quasi-linear approach (Kennel & Engelmann, 1966; Lyons et al., 1972;
 373 Albert, 2005; Glauert & Horne, 2005; Mourenas et al., 2012; Mourenas, Artemyev, Agapi-
 374 tov, & Krasnoselskikh, 2014), especially in the case of field aligned waves, as demonstrated
 375 in previous studies (Tao et al., 2012; Mourenas, Artemyev, et al., 2022; Gan et al., 2022;
 376 Z. An et al., 2022). However, despite their normalization to the measured j_{prec}/j_{trap} at
 377 97 keV, these similar ratios of j_{prec}/j_{trap} (red curves) obtained from test particle sim-
 378 ulations and from the quasi-linear diffusion code become $\sim 1.5 - 2$ times smaller than
 379 the measured j_{prec}/j_{trap} at 200–1000 keV (black), corresponding to a deficiency of pitch-
 380 angle diffusion occurring at higher energies. For reference, this baseline case (red) rep-
 381 represents the same discrepancy on the nightside as first described in Tsai et al. (2023).

382 A reduced plasma density should lower the latitude of first-order cyclotron reso-
 383 nance with chorus waves for electrons near the loss-cone (Mourenas et al., 2012). Since
 384 chorus wave power B_w^2 is higher at lower latitudes (Agapitov et al., 2018), a reduced den-
 385 sity is therefore expected to yield higher electron pitch-angle diffusion rate $D_{\alpha\alpha} \propto B_w^2$
 386 near the loss-cone leading to higher precipitation rates and fluxes at all energies. How-
 387 ever, adopting a reduced plasma density ($\Omega_{pe} = 3$) in test particle simulations (pur-
 388 ple line in Fig. 3) and normalizing the flux ratio at 97 keV leads to an even larger dis-
 389 crepancy across the 300 – 1000 keV range with a $\sim 2 - 3$ times smaller j_{prec}/j_{trap} ra-
 390 tio than ELFIN statistics show. We therefore interpret this density effect as more im-
 391 portant at lower energies (~ 100 keV) compared to higher energies (> 300 keV) due
 392 to $B_w^2(\lambda)$ increasing, in our model and in observations, more steeply towards lower lat-
 393 itudes at $\lambda \lesssim 25^\circ$ (where resonance with ~ 100 keV electrons occurs) than at $\lambda > 25^\circ$
 394 (where resonance with ~ 1 MeV electrons occurs) during disturbed periods at 21-3 MLT
 395 (Agapitov et al., 2018). Therefore, the wave power $B_w^2(\lambda)$ seen by electrons near the loss-
 396 cone increases only marginally at higher energies for both $\theta = 0^\circ$ in test-particle sim-
 397 ulations and $\theta < 5^\circ$ or $\theta < 30^\circ$ in QLDC simulations (solid/dashed purple and dashed
 398 blue lines). This then reduces the normalized pitch-angle diffusion rate $D_{\alpha\alpha}$ near the loss-
 399 cone and the normalized j_{prec}/j_{trap} flux ratio, which varies roughly like $\approx \sqrt{D_{\alpha\alpha}}$ (Kennel
 400 & Petschek, 1966; Li et al., 2013; Mourenas, Zhang, et al., 2022; Mourenas et al., 2023).

401 Adopting a more realistic spread of WNAs for quasi-field aligned waves ($\delta\theta = 30^\circ$,
 402 blue dashed line) in the quasi-linear diffusion code leads to the effects of additional, higher-
 403 order cyclotron resonances to become more significant (Artemyev et al., 2016), which is
 404 clearly shown as the difference between the blue and purple dashed lines in Figure 3. Due
 405 to moderate obliqueness, this effect is most prominent in the lower energies – resonat-
 406 ing with waves around the equator – extending now to about 180 keV. However, it is not
 407 enough to reproduce ELFIN observations up to 1 MeV, because the relative scattering
 408 efficiency decreases with the purple curve at higher energies, causing the blue curve to
 409 underestimate ELFIN statistics beyond > 250 keV. Despite the fact that, in observa-
 410 tions, the plasma frequency to gyrofrequency ratio Ω_{pe} does decrease at 18-4 MLT dur-
 411 ing disturbed periods (O’Brien & Moldwin, 2003), often down to $\Omega_{pe} \approx 3 - 4$ at $L \sim$
 412 6 when $AE > 150$ nT (Agapitov et al., 2019), results in Figure 3 show that plasma den-
 413 sity reduction alone cannot account for a relative increase of electron scattering at higher
 414 energies.

415 4.2 Role of wave frequency

416 As noted earlier, statistical observations of lower-band chorus waves show that their
 417 normalized frequency is not constant as a function of latitude (as assumed in frequency
 418 Model 1), but rather, decreasing due to preferential Landau damping affecting higher
 419 frequencies at higher latitudes (Agapitov et al., 2018; Bunch et al., 2013; L. Chen et al.,
 420 2013), as reflected by frequency Model 2. Figure 4a shows that the j_{prec}/j_{trap} ratios ob-
 421 tained for wave normal angle model FAW from test particle simulations (solid curves)

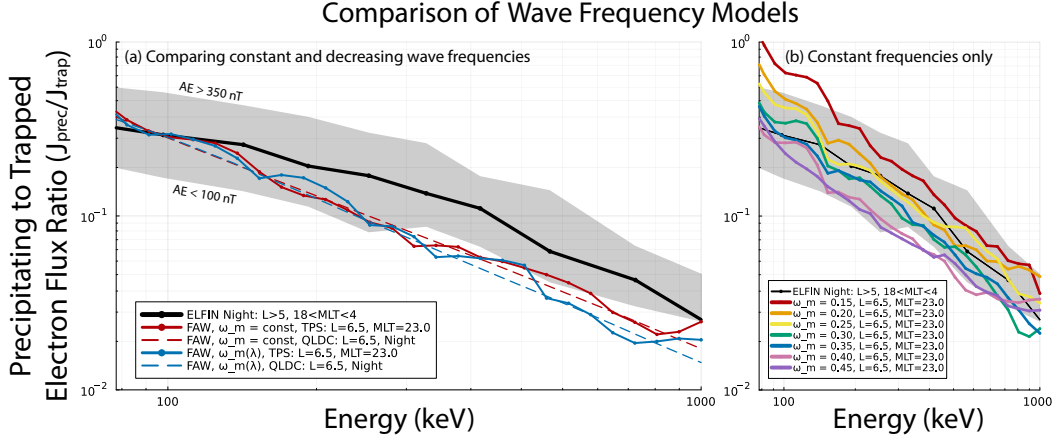


Figure 4. To compare the effects of two frequency models, precipitating-to-trapped electron flux ratio j_{prec}/j_{trap} plotted for ELFIN statistics on the nightside (black) is shown in comparison with j_{prec}/j_{trap} ratios obtained from test particle simulations (TPS, solid lines) and quasi-linear diffusion code (QLDC, dashed lines). In (a), Frequency Model 2 (frequency decreasing toward higher latitudes, blue) produces slightly higher precipitation rates at 100 keV relative to 1 MeV as compared to a constant $\omega_m = 0.35$ (red). Plot (b) shows results from a variety of normalized wave frequency values that do not vary as a function of magnetic latitude, demonstrating that absolute frequency has little effect on the slope of the precipitation energy spectra.

and from the quasi-linear diffusion code (dashed curves) are both slightly decreased at $E = 200 - 1000$ keV when wave frequency Model 2 is used (blue curves), rather than when using Model 1. This is because a reduction of wave frequency alone, when adopting a fixed plasma density $\Omega_{pe} = 6.5$ at $L = 6.5$, has essentially the same effect as decreasing plasma density in Section 4.1 – albeit weaker in magnitude – by allowing first-order cyclotron resonance for electrons near the loss-cone to occur at lower latitudes (Mourenas et al., 2012). In turn, this preferentially increases precipitation rates at low energies $E \lesssim 100$ keV, the typical resonance energies at low-latitude plasma conditions.

Figure 4b shows that decreasing the wave frequency by a fixed amount significantly increases electron precipitation rates by lowering the latitude of resonance with chorus waves. But at the same time, it leads to only a slight increase of the slope of the energy spectrum once normalized to ELFIN statistics, because the amplitude of resonant waves is slightly more increased for 100 keV electrons than for 1 MeV electrons. For a large plasma density, $\Omega_{pe} = 6.5$, this effect on the normalized j_{prec}/j_{trap} remains weak, and both wave frequency Model 1 and 2 end up giving very similar results. Therefore, the effects of frequency variation with latitude alone cannot account for the spectral shape of the precipitation ratio in ELFIN’s nightside observations.

4.3 Role of wave obliquity

Figure 5a compares ELFIN-observed precipitating-to-trapped flux ratio on the nightside (black) with that of simulations in order to explore the effects of a variety of wave-normal angle distributions paired with constant wave frequency (Model 1) and baseline plasma density (Sheeley et al., 2001). Results from test particle simulations (solid curves) and from the quasi-linear diffusion code (dashed curves) are displayed for four different models of wave normal angle: FAW (red), WNA1 (green), WNA2 (blue), and WNA3 (purple), corresponding to a progressively larger amount of wave power in oblique waves closer to the resonance cone angle (see Section 3.3). Despite the large number of particles ($N =$

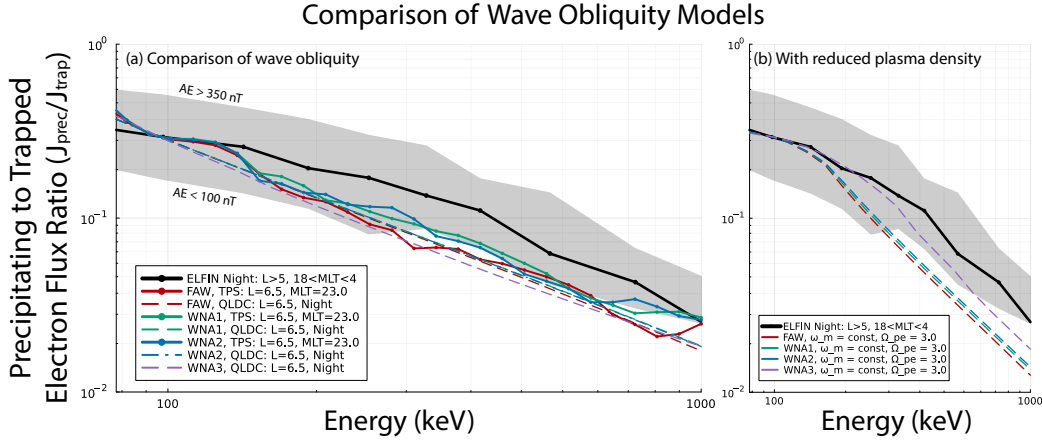


Figure 5. ELFIN-observed j_{prec}/j_{trap} flux ratio at $L > 5$ on the nightside (18 – 4 MLT) as a function of electron energy (black). The corresponding ratios j_{prec}/j_{trap} obtained from test particle simulations (TPS, solid curves) and from the quasi-linear diffusion code (QLDC, dashed curves) are displayed for lower-band chorus waves in (a), using frequency Model 1 of constant frequency, and parameterized by four wave normal angle models: FAW (red), WNA1 (green), WNA2 (blue), and WNA3 (purple), with a normalization to observations at 97 keV, adopting a typical $\Omega_{pe} = 6.5$ at $L = 6.5$ and 23 MLT. (b) shows QLDC results for the same four wave normal angle models but for a reduced plasma density of $\Omega_{pe} = 3.0$.

5 $\times 10^6$), unnatural oscillations in the test particle simulations make it difficult to quantify the exact contribution differences among the FAW, WNA1, and WNA2 models. Especially because the test particle simulation only includes first-order oblique wave interactions, it is reasonable to conclude that including wave obliquity in the TPS does not significantly alter precipitation efficiency. However, results from the quasi-linear diffusion code generally agree with test particle simulation results, indicating the reliability of the quasi-linear approach (described, e.g., by Kennel & Engelmann, 1966; Lyons et al., 1972; Albert, 2005; Glauert & Horne, 2005; Mourenas et al., 2012; Mourenas, Artemyev, Agapitov, & Krasnoselskikh, 2014). Our quasi-linear simulations show that wave obliquity is ineffective at increasing high energy electron precipitation compared to low energy electron precipitation (in the case of $\Omega_{pe} = 6.5$). Note that WNA1 and WNA2 models correspond to wave-normal angle distributions that extend up to three-quarters of the Gendrin angle and resonance cone angle, respectively, at $\lambda > 45^\circ$, while the WNA3 model corresponds to highly oblique waves, at about 2° from the resonance cone angle. Yet the results are nearly identical (dashed blue, dashed green, and dashed purple curves).

Oblique chorus waves can resonate with electrons via high-order cyclotron resonances ($n \geq 1$ or $n \leq -2$, e.g., Shklyar & Matsumoto, 2009; Mourenas et al., 2012; Artemyev et al., 2013, 2016; Albert, 2017), which can significantly increase diffusion rates at high energy (Lorentzen et al., 2001; Gan et al., 2023). However, diffusion rates near the loss cone due to higher-order cyclotron resonances rapidly decrease in magnitude as $|n|$ increases, especially from $|n| = 1$ to $|n| = 2$ (Shprits & Ni, 2009), although this reduction is weaker for highly oblique waves (Artemyev et al., 2016). To increase the ratio of 1 MeV to 100 keV pitch-angle diffusion rates near the loss cone, therefore, the waves must be sufficiently oblique and/or plasma density and wave frequency should be sufficiently low to enable only first-order resonance at ~ 100 keV, but higher-order resonances at 1 MeV (Artemyev et al., 2016; Mourenas & Ripoll, 2012; Shprits & Ni, 2009; Gan et al., 2023). Figure 5b indeed shows that when plasma density is reduced to $\Omega_{pe} = 3$ (or equiv-

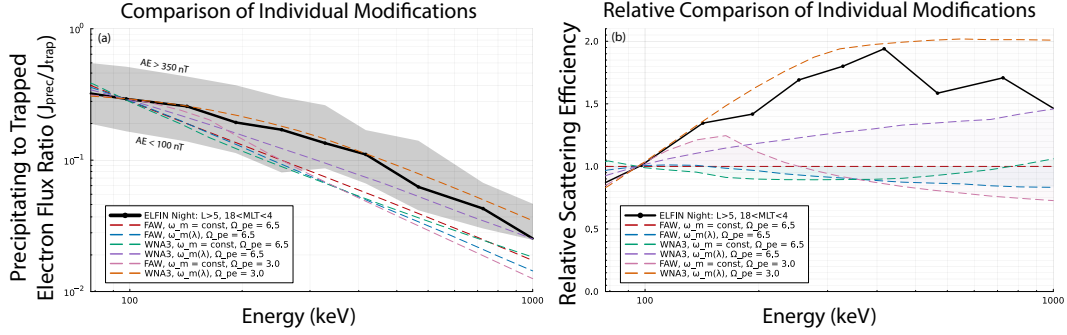


Figure 6. ELFIN-observed nightside ($18 - 4$ MLT) j_{prec}/j_{trap} electron flux ratio shown as a function of energy (black). (a) shows j_{prec}/j_{trap} flux ratios obtained from quasi-linear diffusion code (QLDC) for parallel (FAW) lower-band chorus waves (red), very oblique waves using wave normal angle model WNA3 (green), waves with a realistic wave frequency distribution (blue), WNA3 with a realistic wave frequency distribution (purple), FAW with reduced density (pink), and everything combined (orange). (b) shows the same flux ratios all normalized to the base case with no modifications (red) demonstrating which energy range each modification is most effective at on a linear scale. This shows that each effect examined alone cannot reproduce results from ELFIN individually.

475 alently, when wave frequency decreases with latitude, see Section 4.4), electron precip-
 476 itation is greatly increased at 1 MeV relative to 100 keV as wave obliquity increases, espe-
 477 cially in the case of highly oblique waves (WNA3). These results therefore suggest that
 478 wave obliquity, alone, has a near-negligible effect on the high-energy to low-energy elec-
 479 tron loss ratio; however, when combined with a density reduction, it can significantly en-
 480 hance energetic electron losses.

481 4.4 Combined results

482 Figure 6a shows comparisons between the precipitating-to-trapped electron flux ra-
 483 tio j_{prec}/j_{trap} measured by ELFIN at $L > 5$ on the nightside (black), overlaid with j_{prec}/j_{trap}
 484 obtained from the quasi-linear diffusion code for the three modifications in question –
 485 reduced plasma density $\Omega_{pe} = 3$, Frequency Model 2, and WNA3 – alone or in com-
 486 bination. As surmised in previous sections, each individual modification fails to agree
 487 with the observed spectrum. With wave frequency Model 2 (blue) and WNA3 (green)
 488 underestimating across entire energy range (i.e., increasing precipitation at 100 keV) and
 489 reduced density (pink) providing a relative efficiency bump of j_{prec}/j_{trap} only at $E <$
 490 200 keV. Interestingly, however, ELFIN’s statistical observations are only slightly un-
 491 derestimated when combining WNA3 and Frequency Model 2 (purple), and best matched
 492 when all three modifications are combined (orange). Figure 6b shows the relative dif-
 493 ference produced by each modification compared to the baseline red curve. We see that
 494 these effects synergistically enhance j_{prec}/j_{trap} flux ratios at higher energies. For exam-
 495 ple, Model 2 (blue) becomes relatively less effective at higher energy, while WNA3 (green)
 496 immediately loses effectiveness, but catches back up closer to 1 MeV. However, when com-
 497 bined (purple), the relative precipitation is drastically enhanced in the entire 200–1000
 498 keV range, leading to far better agreement with observations. Further combining WNA3
 499 and Frequency Model 2 with a reduced plasma density (orange) significantly enhances
 500 precipitation past levels observed by ELFIN (black). This is likely due to two phenom-
 501 ena: first, the combined effects of a reduced plasma density and a decreasing wave fre-
 502 quency decrease the latitude at which cyclotron resonance with quasi-parallel waves oc-

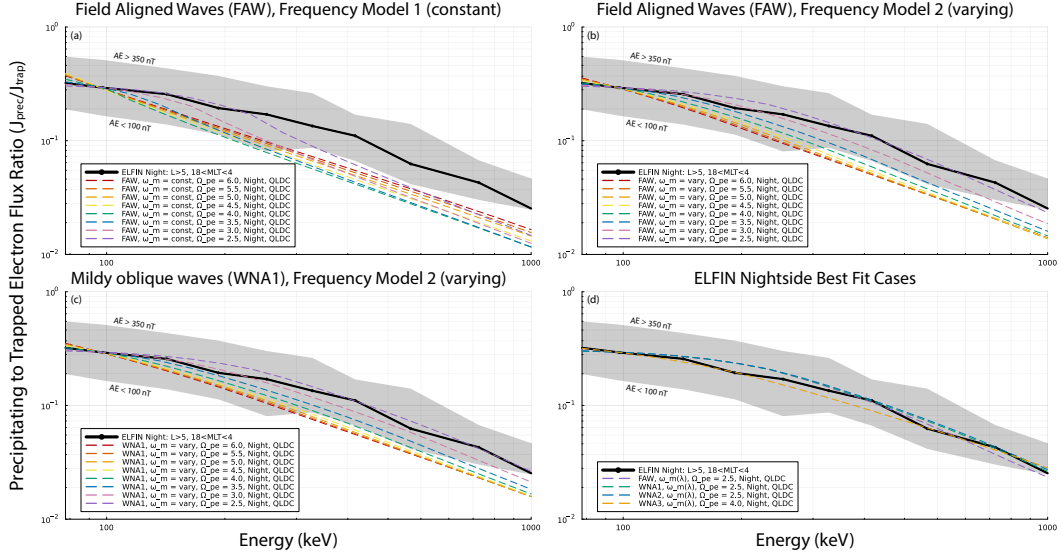


Figure 7. The comparison between observed electron precipitation ratios and simulation results using different wave frequency models, Ω_{pe} ratios, and wave normal angle models. In each plot, the black line denotes statistical averages of j_{prec}/j_{trap} flux ratios for nightside ELFEN observations with $L > 5$. Plots (a-c) show QLDC results with various modifications parameterized by Ω_{pe} : (a) shows field aligned waves with Frequency Model 1; (b) shows field aligned waves with Frequency Model 2; and (c) shows WNA1 combined with Frequency Model 2. (d) shows that all three effects – $\omega_{pe} \in [2.5, 4]$, combined with Frequency Model 2 and some level of wave obliquity – are necessary for recreating ELFEN nightside statistics.

503 curs far more significantly than each effect alone (Mourenas et al., 2012), leading to a
 504 larger increase of resonant wave power for higher energy electrons that best match ELFEN’s
 505 observed precipitation spectra; second, the supplementary higher-order cyclotron reso-
 506 nances contributing at ~ 1 MeV, but not at ~ 150 keV, are of lower order ($|n| = 2$)
 507 than for higher density or frequency, allowing for a more dramatic increase of the 1 MeV
 508 to 150 keV pitch-angle diffusion rate ratio (Artemyev et al., 2016; Mourenas & Ripoll,
 509 2012; Shprits & Ni, 2009; Gan et al., 2023).

510 Figure 7 summarizes the findings from each wave parameter combination through-
 511 out a range of reduced equatorial plasma densities for a better understanding of the inter-
 512 play between the three effects considered. Figure 7a shows that only below a certain
 513 threshold of $\Omega_{pe} \lesssim 4$ does the interaction of higher-order resonances start to increase
 514 precipitation at higher energies. Using the total electron density with $\Omega_{pe} = 2.5$, this
 515 effect becomes very pronounced above 100 keV and up to 300 keV, whereas above that
 516 energy this effect alone is still incapable of matching observations, as discussed in Sec-
 517 tion 4.1. The effect of plasma density combined with wave frequency becomes significantly
 518 more pronounced throughout the whole energy range when $\Omega_{pe} \lesssim 4$, as shown in Fig-
 519 ure 7b, and matches very well with ELFEN’s nightside observations when a more extreme
 520 $\Omega_{pe} = 2.5$ is used. Adding mild wave obliquity (Figure 7c) results in the best match
 521 with ELFEN statistics, demonstrating that all three effects combined are necessary.

522 Figure 7d shows the best fit scenarios for forward-modeling ELFEN-observed precipitating-
 523 to-trapped flux ratios, which all require the varying frequency model in addition to re-
 524 duced plasma density to various degrees. Here, we show that it is possible to obtain de-
 525 cent agreement without the need for wave obliquity by significantly reducing Ω_{pe} to 2.5

(purple). By adding moderately oblique waves (green and blue), more ~ 1 MeV electrons are precipitated, doing a marginally better job of matching observations. Using extremely oblique waves (WNA3) – which describes a population of very oblique waves generated around the equator when the Landau damping is largely reduced by field-aligned electron streams (Mourenas et al., 2015; Li, Mourenas, et al., 2016) – requires increasing plasma density $\Omega_{pe} = 4$ in order to avoid significant overestimation. Therefore, ELFIN observations of nightside electron precipitation spectra (from 50–1000 keV) can be described either under the assumption of a significant plasma density reduction or a more moderate plasma density reduction coupled with a strongly oblique wave population. This required plasma density ($\omega_{pe} \in [2.5, 4]$) is fully consistent with the average measured ω_{pe} levels at 18-4 MLT and $L = 5-6.5$ in Van Allen Probes statistics during disturbed periods with $AE \in [150, 600]$ nT (Agapitov et al., 2019). These conditions indicate the importance of plasma injections and/or enhanced convection periods and how they cause enhanced nightside electron losses. Such Earthward plasma transport (convection and injections), especially during increased geomagnetic activity, justifies our choice of the cold plasma density reduction (Agapitov et al., 2019). These injections are also associated with electron field-aligned streams caused by the electrostatic turbulence around injection regions or the ionosphere outflow of secondary electrons in response to the enhanced precipitation of plasma sheet electron fluxes (see Khazanov et al., 2014, 2018; Artemyev & Mourenas, 2020; Artemyev et al., 2020, and references therein).

5 Discussion and Conclusions

Today’s radiation belt simulations primarily rely on EMIC-driven electron precipitation to explain relativistic electron losses (see, e.g., Ma et al., 2015; Drozdov et al., 2017, and references therein), in addition to dropouts related to magnetopause shadowing loss (e.g., see Shprits et al., 2006; Turner et al., 2014; Boynton et al., 2016, 2017; Olfier et al., 2018; Xiang et al., 2018). Analysis presented here shows that the inclusion of realistic whistler-mode wave properties can meaningfully enhance relativistic electron scattering rates, thereby reducing the relative importance of EMIC waves on the nightside, at least for electrons below 1 MeV. While it has been known for a long time that whistler-mode waves can accelerate electrons to relativistic energies (Thorne et al., 2013; Li et al., 2014; Mourenas, Artemyev, Agapitov, Krasnoselskikh, & Li, 2014; Omura et al., 2015; Hsieh & Omura, 2017; Allison & Shprits, 2020), contribution of this wave mode to relativistic electron losses may be underestimated in modern-day simulations due to the lack of observations that can reliably quantify it. This has recently changed with the availability of ELFIN’s unique precipitation observations, which now allow us to quantify how well modeling – based on statistical averages of wave properties and plasma density – reflects the observed precipitation energy spectra of energetic electrons.

We previously showed that using only field-aligned, monochromatic whistler-mode waves with realistic wave amplitudes as a function of magnetic latitude was sufficient to approximate relativistic electron losses at the dawn, noon, and dusk sectors (Tsai et al., 2023). However, the modeled precipitating-to-trapped flux ratio significantly underestimated ELFIN-obtained statistics of precipitation energy spectra in the nightside MLT sector. Pertinent to ELFIN statistics, we specifically excluded all data exhibiting signatures of field-line curvature scattering, EMIC waves, and any signatures of noise or poor statistics. The resulting ELFIN statistics are 3 years of unambiguous whistler-mode wave-driven energetic electron precipitating-to-trapped flux ratios across a range of MLT, L -shells, and geomagnetic activity. At first, we used test particle simulations to examine various wave and plasma characteristics that may potentially cause this discrepancy. However, test particle simulations showed that, while some effects led to better agreement, the discrepancy was still large. However, by additionally utilizing a state-of-the-art quasi-linear diffusion code, we were able to quantify each key wave parameter – alone and in combination – relative to ELFIN observations, thereby determining the importance of

578 including empirically-obtained equatorial plasma frequency, wave-normal angle distri-
 579 butions, and wave frequency distributions. We found that, in addition to the prerequi-
 580 site, empirically-provided $B_w(\lambda)$ (Tsai et al., 2023), inclusion of all three modifications
 581 – realistic Ω_{pe} , $\omega_m(\lambda)$, and $\theta(\lambda)$ – were sufficient to recover the more intense nightside
 582 energetic precipitation observed by ELFIN. A reduced plasma density, indicative of geo-
 583 magnetically active times, results in relative enhancement of precipitation in the sub-
 584 relativistic regime (< 300 keV), while wave obliquity significantly enhances relativistic
 585 electron scattering > 500 keV. It seems that a decreasing wave frequency as a function
 586 of latitude helps balance the two out, leading to a smooth recovery of the 200–600 keV
 587 range, without severely overestimating either ends of the precipitation flux ratio spec-
 588 trum.

589 The equatorial confinement of whistler-mode waves is attributed to the increase
 590 of wave obliquity – or more precisely, the increase of statistical averages of wave normal
 591 angles – as expected from wave propagation away from their equatorial source (L. Chen
 592 et al., 2013; Breuillard et al., 2012; Agapitov et al., 2013) due to the associated severe
 593 damping by Landau resonance with suprathermal electrons (e.g., Bell et al., 2002; Bort-
 594 nik et al., 2007). This effect is substantially less important on the dayside as compared
 595 to the nightside, as evidenced by the significantly larger amplitudes of waves at higher
 596 latitudes on the dayside (Meredith et al., 2012). Reduced Landau damping is caused by
 597 a milder ambient dayside magnetic field gradient (due to magnetospheric compression)
 598 and a lower density of suprathermal electrons (Li, Thorne, Bortnik, et al., 2010; Walsh
 599 et al., 2020). As a result, waves on the dayside propagate in higher densities, are less oblique,
 600 and have a less pronounced decrease in wave frequencies, in direct opposition to what
 601 is observed on the nightside. This explains why an empirical model of $B_w(\lambda)$ and field
 602 aligned waves is sufficient for recovering dayside energetic electron precipitation (Tsai
 603 et al., 2023), while further indicating the importance of including realistic wave and back-
 604 ground plasma characteristics for such precipitation modeling on the nightside.

605 To conclude, these results highlight the importance of combining whistler-mode wave
 606 characteristics and background plasma for accurately modeling relativistic electron losses
 607 from the outer radiation belt. Specifically, we note that:

- 608 • The latitudinal distribution of wave amplitude alone cannot account for the in-
 609 tense nightside precipitation of ~ 0.1 – 1 MeV electrons scattered at mid-to-high
 610 latitudes relative to precipitation of ~ 100 keV electrons scattered near the equa-
 611 tor.
- 612 • Very oblique waves are important for scattering more energetic electrons – becom-
 613 ing more effective in the ~ 1 MeV range – but only in the presence of reduced
 614 plasma density or decreasing wave frequency.
- 615 • The decrease of wave frequency with latitude, caused by high-frequency wave damp-
 616 ing, is not very important on its own. However, together with a reduced plasma
 617 density (with or without oblique waves), it can lead to more precipitation of high
 618 energy electrons relative to ~ 100 keV electrons.
- 619 • Equatorial plasma density decrease during geomagnetically active conditions (char-
 620 acterized by enhanced whistler-mode wave intensity) improves the relative efficiency
 621 of resonant electron scattering toward the loss-cone at 100 keV compared to 1 MeV,
 622 but alone, it is in poor agreement with ELFIN statistics. However, when combined
 623 with increasing WNA and decreasing wave frequency as a function of latitude, this
 624 plasma density reduction becomes a catalyst, significantly boosting electron pre-
 625 cipitation rates across the energy range up to 1 MeV.

626 So, in order to best explain the increased precipitation observed by ELFIN on the night-
 627 side, modeled whistler-mode waves must have a realistic latitudinally-dependent wave
 628 frequency model (Model 2) coupled with a reduced plasma density ($\Omega_{pe} \in [2.5, 4]$) and
 629 an associated range of wave obliquity from quasi-field aligned ($\theta < 30^\circ$) to extremely

630 oblique (WNA3) waves. Any further investigation of these effects likely requires either
 631 detailed and comprehensive simulations using modern ray-tracing techniques (e.g., L. Chen
 632 et al., 2021, 2022; Hosseini et al., 2021; Hanzelka & Santolík, 2022; Kang et al., 2022;
 633 Kang & Bortnik, 2022) or a new generation of satellite missions equipped to make si-
 634 multaneous measurements of whistler-mode waves and precipitating/trapped electron
 635 populations.

636 Acknowledgments

637 We are grateful to NASA’s CubeSat Launch Initiative and Launch Services Program for
 638 ELFIN’s successful launch in the desired orbits. We acknowledge early support of ELFIN
 639 project by the AFOSR, under its University Nanosat Program, UNP-8 project, contract
 640 FA9453-12-D-0285, and by the California Space Grant program. Importantly, we acknowl-
 641 edge the critical contributions by numerous UCLA students who made the ELFIN mis-
 642 sion a success. A.V.A and X.-J.Z. acknowledge support from the NASA grants 80NSSC23K0089,
 643 80NSSC22K0522, 80NSSC23K0108, 80NSSC19K0844, 80NSSC23K0100 and NSF grant
 644 2329897. V. A. acknowledge support from NSF grants AGS-1242918, AGS-2019950, and
 645 AGS-2329897. Q.M. acknowledges the NASA grant 80NSSC20K0196 and NSF grant AGS-
 646 2225445. The work O.V.A. was supported by NASA grants 80NNSC19K0848, 80NSSC20K0697,
 647 80NSSC22K0433, 80NSSC22K0522, NASA’s Living with a Star (LWS) program (con-
 648 tract 80NSSC20K0218), and by NSF grant number 1914670.

649 Open Research

650 ELFIN data is available at <https://data.elfin.ucla.edu/> and online summary plots
 651 at <https://plots.elfin.ucla.edu/summary.php>.
 652 Data access and processing was done using SPEDAS V4.1, see Angelopoulos et al. (2019).
 653 Test-particle simulation code is found at <https://github.com/ethantsai/nlwhistlers>
 654 (Tsai, 2023).

655 References

- 656 Agapitov, O. V., Artemyev, A., Krasnoselskikh, V., Khotyaintsev, Y. V., Moure-
 657 nas, D., Breuillard, H., . . . Rolland, G. (2013, June). Statistics of whistler
 658 mode waves in the outer radiation belt: Cluster STAFF-SA measurements. *J.*
 659 *Geophys. Res.*, *118*, 3407-3420. doi: 10.1002/jgra.50312
- 660 Agapitov, O. V., Krasnoselskikh, V., Mozer, F. S., Artemyev, A. V., & Volokitin,
 661 A. S. (2015, May). Generation of nonlinear electric field bursts in the outer
 662 radiation belt through the parametric decay of whistler waves. *Geophys. Res.*
 663 *Lett.*, *42*, 3715-3722. doi: 10.1002/2015GL064145
- 664 Agapitov, O. V., Mourenas, D., Artemyev, A., Hospodarsky, G., & Bonnell, J. W.
 665 (2019, June). Time Scales for Electron Quasi-linear Diffusion by Lower-Band
 666 Chorus Waves: The Effects of ω_{pe}/Ω_{ce} Dependence on Geomagnetic Activity.
 667 *Geophys. Res. Lett.*, *46*(12), 6178-6187. doi: 10.1029/2019GL083446
- 668 Agapitov, O. V., Mourenas, D., Artemyev, A. V., & Mozer, F. S. (2016). Exclusion
 669 principle for very oblique and parallel lower band chorus waves. *Geophys. Res.*
 670 *Lett.*, *43*(21), 11,112–11,120. Retrieved from [http://dx.doi.org/10.1002/](http://dx.doi.org/10.1002/2016GL071250)
 671 [2016GL071250](http://dx.doi.org/10.1002/2016GL071250) doi: 10.1002/2016GL071250
- 672 Agapitov, O. V., Mourenas, D., Artemyev, A. V., Mozer, F. S., Hospodarsky, G.,
 673 Bonnell, J., & Krasnoselskikh, V. (2018, January). Synthetic Empirical
 674 Chorus Wave Model From Combined Van Allen Probes and Cluster Statis-
 675 tics. *Journal of Geophysical Research (Space Physics)*, *123*(1), 297-314. doi:
 676 10.1002/2017JA024843
- 677 Albert, J. M. (2001, May). Comparison of pitch angle diffusion by turbulent and
 678 monochromatic whistler waves. *J. Geophys. Res.*, *106*, 8477-8482. doi: 10

- 679 .1029/2000JA000304
 680 Albert, J. M. (2005, March). Evaluation of quasi-linear diffusion coefficients for
 681 whistler mode waves in a plasma with arbitrary density ratio. *J. Geophys.*
 682 *Res.*, *110*, 3218. doi: 10.1029/2004JA010844
 683 Albert, J. M. (2010, March). Diffusion by one wave and by many waves. *J. Geo-*
 684 *phys. Res.*, *115*, 0. doi: 10.1029/2009JA014732
 685 Albert, J. M. (2017, May). Quasi-linear diffusion coefficients for highly oblique
 686 whistler mode waves. *J. Geophys. Res.*, *122*, 5339-5354. doi: 10.1002/
 687 2017JA024124
 688 Albert, J. M., Artemyev, A. V., Li, W., Gan, L., & Ma, Q. (2021). Models of
 689 resonant wave-particle interactions. *Journal of Geophysical Research: Space*
 690 *Physics*, *126*(6), e2021JA029216. doi: 10.1029/2021JA029216
 691 Albert, J. M., Tao, X., & Bortnik, J. (2013). Aspects of Nonlinear Wave-Particle In-
 692 teractions. In D. Summers, I. U. Mann, D. N. Baker, & M. Schulz (Eds.), *Dy-*
 693 *namics of the earth's radiation belts and inner magnetosphere*. doi: 10.1029/
 694 2012GM001324
 695 Allison, H. J., & Shprits, Y. Y. (2020, September). Local heating of radiation belt
 696 electrons to ultra-relativistic energies. *Nature Communications*, *11*, 4533. doi:
 697 10.1038/s41467-020-18053-z
 698 Allison, H. J., Shprits, Y. Y., Zhelavskaya, I. S., Wang, D., & Smirnov, A. G. (2021,
 699 January). Gyroresonant wave-particle interactions with chorus waves during
 700 extreme depletions of plasma density in the Van Allen radiation belts. *Science*
 701 *Advances*, *7*(5), eabc0380. doi: 10.1126/sciadv.abc0380
 702 An, X., Artemyev, A., Angelopoulos, V., Zhang, X., Mourenas, D., & Bortnik, J.
 703 (2022, September). Nonresonant Scattering of Relativistic Electrons by Elec-
 704 tromagnetic Ion Cyclotron Waves in Earth's Radiation Belts. *Phys Rev. Lett.*,
 705 *129*(13), 135101. doi: 10.1103/PhysRevLett.129.135101
 706 An, Z., Wu, Y., & Tao, X. (2022). Electron dynamics in a chorus wave field
 707 generated from particle-in-cell simulations. *Geophys. Res. Lett.*, *49*(3),
 708 e2022GL097778. doi: 10.1029/2022GL097778
 709 Angelopoulos, V., Cruce, P., Drozdov, A., Grimes, E. W., Hatzigeorgiu, N., King,
 710 D. A., ... Schroeder, P. (2019, January). The Space Physics Environ-
 711 ment Data Analysis System (SPEDAS). *Space Sci. Rev.*, *215*, 9. doi:
 712 10.1007/s11214-018-0576-4
 713 Angelopoulos, V., Tsai, E., Bingley, L., Shaffer, C., Turner, D. L., Runov, A., ...
 714 Zhang, G. Y. (2020, July). The ELFING Mission. *Space Sci. Rev.*, *216*(5), 103.
 715 doi: 10.1007/s11214-020-00721-7
 716 Angelopoulos, V., Zhang, X. J., Artemyev, A. V., Mourenas, D., Tsai, E., Wilkins,
 717 C., ... Zarifian, A. (2023, August). Energetic Electron Precipitation Driven by
 718 Electromagnetic Ion Cyclotron Waves from ELFING's Low Altitude Perspective.
 719 *Space Sci. Rev.*, *219*(5), 37. doi: 10.1007/s11214-023-00984-w
 720 Artemyev, A. V., Agapitov, O., Mourenas, D., Krasnoselskikh, V., Shastun, V., &
 721 Mozer, F. (2016, April). Oblique Whistler-Mode Waves in the Earth's Inner
 722 Magnetosphere: Energy Distribution, Origins, and Role in Radiation Belt Dy-
 723 namics. *Space Sci. Rev.*, *200*(1-4), 261-355. doi: 10.1007/s11214-016-0252-5
 724 Artemyev, A. V., Angelopoulos, V., Zhang, X. J., Runov, A., Petrukovich, A., Naka-
 725 mura, R., ... Wilkins, C. (2022, October). Thinning of the Magnetotail Cur-
 726 rent Sheet Inferred From Low-Altitude Observations of Energetic Electrons.
 727 *Journal of Geophysical Research (Space Physics)*, *127*(10), e2022JA030705.
 728 doi: 10.1029/2022JA030705
 729 Artemyev, A. V., & Mourenas, D. (2020, March). On Whistler Mode Wave Relation
 730 to Electron Field-Aligned Plateau Populations. *Journal of Geophysical Re-*
 731 *search (Space Physics)*, *125*(3), e27735. doi: 10.1029/2019JA027735
 732 Artemyev, A. V., Mourenas, D., Agapitov, O. V., & Krasnoselskikh, V. V. (2013,
 733 April). Parametric validations of analytical lifetime estimates for radiation belt

- 734 electron diffusion by whistler waves. *Annales Geophysicae*, *31*, 599-624. doi:
735 10.5194/angeo-31-599-2013
- 736 Artemyev, A. V., Zhang, X. J., Angelopoulos, V., Mourenas, D., Vainchtein, D.,
737 Shen, Y., ... Runov, A. (2020, September). Ionosphere Feedback to Elec-
738 tron Scattering by Equatorial Whistler Mode Waves. *Journal of Geophysical*
739 *Research (Space Physics)*, *125*(9), e28373. doi: 10.1029/2020JA028373
- 740 Aryan, H., Agapitov, O. V., Artemyev, A., Mourenas, D., Balikhin, M. A., Boynton,
741 R., & Bortnik, J. (2020, August). Outer Radiation Belt Electron Lifetime
742 Model Based on Combined Van Allen Probes and Cluster VLF Measure-
743 ments. *Journal of Geophysical Research (Space Physics)*, *125*(8), e28018. doi:
744 10.1029/2020JA028018
- 745 Bell, T. F., Inan, U. S., Bortnik, J., & Scudder, J. D. (2002, August). The Landau
746 damping of magnetospherically reflected whistlers within the plasmasphere.
747 *Geophys. Res. Lett.*, *29*, 1733. doi: 10.1029/2002GL014752
- 748 Bezanson, J., Edelman, A., Karpinski, S., & Shah, V. B. (2017). Julia: A fresh ap-
749 proach to numerical computing. *SIAM review*, *59*(1), 65–98. Retrieved from
750 <https://doi.org/10.1137/141000671>
- 751 Blake, J. B., & O'Brien, T. P. (2016, April). Observations of small-scale latitudinal
752 structure in energetic electron precipitation. *Journal of Geophysical Research*
753 *(Space Physics)*, *121*(4), 3031-3035. doi: 10.1002/2015JA021815
- 754 Blum, L. W., Halford, A., Millan, R., Bonnell, J. W., Goldstein, J., Usanova, M.,
755 ... Li, X. (2015, July). Observations of coincident EMIC wave activity and
756 duskside energetic electron precipitation on 18-19 January 2013. *Geophys.*
757 *Res. Lett.*, *42*, 5727-5735. doi: 10.1002/2015GL065245
- 758 Blum, L. W., Li, X., & Denton, M. (2015, May). Rapid MeV electron precipitation
759 as observed by SAMPEX/HILT during high-speed stream-driven storms. *J.*
760 *Geophys. Res.*, *120*, 3783-3794. doi: 10.1002/2014JA020633
- 761 Bortnik, J., & Thorne, R. M. (2007, March). The dual role of ELF/VLF chorus
762 waves in the acceleration and precipitation of radiation belt electrons. *Journal*
763 *of Atmospheric and Solar-Terrestrial Physics*, *69*, 378-386. doi: 10.1016/j.jastp
764 .2006.05.030
- 765 Bortnik, J., Thorne, R. M., & Inan, U. S. (2008, November). Nonlinear interac-
766 tion of energetic electrons with large amplitude chorus. *Geophys. Res. Lett.*,
767 *35*, 21102. doi: 10.1029/2008GL035500
- 768 Bortnik, J., Thorne, R. M., Meredith, N. P., & Santolik, O. (2007, August). Ray
769 tracing of penetrating chorus and its implications for the radiation belts. *Geo-*
770 *phys. Res. Lett.*, *34*, L15109. doi: 10.1029/2007GL030040
- 771 Boynton, R. J., Mourenas, D., & Balikhin, M. A. (2016, September). Electron
772 flux dropouts at Geostationary Earth Orbit: Occurrences, magnitudes, and
773 main driving factors. *Journal of Geophysical Research (Space Physics)*, *121*,
774 8448-8461. doi: 10.1002/2016JA022916
- 775 Boynton, R. J., Mourenas, D., & Balikhin, M. A. (2017, November). Electron Flux
776 Dropouts at $L \sim 4.2$ From Global Positioning System Satellites: Occurrences,
777 Magnitudes, and Main Driving Factors. *Journal of Geophysical Research*
778 *(Space Physics)*, *122*, 11. doi: 10.1002/2017JA024523
- 779 Breneman, A. W., Crew, A., Sample, J., Klumpar, D., Johnson, A., Agapitov,
780 O., ... Kletzing, C. A. (2017, November). Observations Directly Link-
781 ing Relativistic Electron Microbursts to Whistler Mode Chorus: Van Allen
782 Probes and FIREBIRD II. *Geophys. Res. Lett.*, *44*(22), 11,265-11,272. doi:
783 10.1002/2017GL075001
- 784 Breuillard, H., Zaliznyak, Y., Krasnoselskikh, V., Agapitov, O., Artemyev, A., &
785 Rolland, G. (2012). Chorus wave-normal statistics in the Earth's radia-
786 tion belts from ray tracing technique. *Ann. Geophys.*, *30*, 1223-1233. doi:
787 10.5194/angeo-30-1223-2012
- 788 Büchner, J., & Zelenyi, L. M. (1989, September). Regular and chaotic charged

- 789 particle motion in magnetotaillike field reversals. I - Basic theory of trapped
790 motion. *J. Geophys. Res.*, *94*, 11821-11842. doi: 10.1029/JA094iA09p11821
- 791 Bunch, N. L., Spasojevic, M., Shprits, Y. Y., Gu, X., & Foust, F. (2013, April). The
792 spectral extent of chorus in the off-equatorial magnetosphere. *J. Geophys.*
793 *Res.*, *118*, 1700-1705. doi: 10.1029/2012JA018182
- 794 Capannolo, L., Li, W., Ma, Q., Chen, L., Shen, X. C., Spence, H. E., ... Redmon,
795 R. J. (2019, November). Direct Observation of Subrelativistic Electron Pre-
796 cipitation Potentially Driven by EMIC Waves. *Geophys. Res. Lett.*, *46*(22),
797 12,711-12,721. doi: 10.1029/2019GL084202
- 798 Capannolo, L., Li, W., Ma, Q., Qin, M., Shen, X. C., Angelopoulos, V., ...
799 Hanzelka, M. (2023). Electron precipitation observed by elfin using proton
800 precipitation as a proxy for electromagnetic ion cyclotron (emic) waves. *Geo-*
801 *physical Research Letters*. doi: <https://doi.org/10.1029/2023GL103519>
- 802 Chen, L., Thorne, R. M., Li, W., & Bortnik, J. (2013, March). Modeling the wave
803 normal distribution of chorus waves. *J. Geophys. Res.*, *118*, 1074-1088. doi:
804 10.1029/2012JA018343
- 805 Chen, L., Zhang, X.-J., Artemyev, A., Angelopoulos, V., Tsai, E., Wilkins, C., &
806 Horne, R. B. (2022, March). Ducted Chorus Waves Cause Sub-Relativistic and
807 Relativistic Electron Microbursts. *Geophys. Res. Lett.*, *49*(5), e97559. doi:
808 10.1029/2021GL097559
- 809 Chen, L., Zhang, X.-J., Artemyev, A., Zheng, L., Xia, Z., Breneman, A. W., &
810 Horne, R. B. (2021, October). Electron microbursts induced by nonducted
811 chorus waves. *Frontiers in Astronomy and Space Sciences*, *8*, 163. doi:
812 10.3389/fspas.2021.745927
- 813 Chen, R., Gao, X., Lu, Q., & Wang, S. (2019, November). Unraveling the Cor-
814 relation Between Chorus Wave and Electron Beam-Like Distribution in the
815 Earth's Magnetosphere. *Geophys. Res. Lett.*, *46*(21), 11,671-11,678. doi:
816 10.1029/2019GL085108
- 817 Demekhov, A. G., Trakhtengerts, V. Y., Rycroft, M. J., & Nunn, D. (2006, Decem-
818 ber). Electron acceleration in the magnetosphere by whistler-mode waves
819 of varying frequency. *Geomagnetism and Aeronomy*, *46*, 711-716. doi:
820 10.1134/S0016793206060053
- 821 Drozdov, A. Y., Shprits, Y. Y., Usanova, M. E., Aseev, N. A., Kellerman, A. C.,
822 & Zhu, H. (2017, August). EMIC wave parameterization in the long-
823 term VERB code simulation. *J. Geophys. Res.*, *122*, 8488-8501. doi:
824 10.1002/2017JA024389
- 825 Fu, X., Cowee, M. M., Friedel, R. H., Funsten, H. O., Gary, S. P., Hospodarsky,
826 G. B., ... Winske, D. (2014, October). Whistler anisotropy instabilities as the
827 source of banded chorus: Van Allen Probes observations and particle-in-cell
828 simulations. *Journal of Geophysical Research (Space Physics)*, *119*, 8288-8298.
829 doi: 10.1002/2014JA020364
- 830 Gabrielse, C., Angelopoulos, V., Runov, A., & Turner, D. L. (2014, April). Statisti-
831 cal characteristics of particle injections throughout the equatorial magnetotail.
832 *J. Geophys. Res.*, *119*, 2512-2535. doi: 10.1002/2013JA019638
- 833 Gan, L., Artemyev, A., Li, W., Zhang, X.-J., Ma, Q., Mourenas, D., ... Wilkins,
834 C. (2023). Bursty energetic electron precipitation by high-order reso-
835 nance with very-oblique whistler-mode waves. *Geophys. Res. Lett.* doi:
836 10.1029/2022GL101920
- 837 Gan, L., Li, W., Ma, Q., Artemyev, A. V., & Albert, J. M. (2022). Dependence of
838 nonlinear effects on whistler-mode wave bandwidth and amplitude: A perspec-
839 tive from diffusion coefficients. *J. Geophys. Res.*, *127*, e2021JA030063. doi:
840 10.1029/2021JA030063
- 841 Gendrin, R. (1961, August). Le guidage des whistlers par le champ magnetique.
842 *Planetary Space Science*, *5*, 274. doi: 10.1016/0032-0633(61)90096-4
- 843 Glauert, S. A., & Horne, R. B. (2005, April). Calculation of pitch angle and energy

- 844 diffusion coefficients with the PADIE code. *J. Geophys. Res.*, *110*, 4206. doi:
845 10.1029/2004JA010851
- 846 Grach, V. S., Artemyev, A. V., Demekhov, A. G., Zhang, X.-J., Bortnik, J., An-
847 gelopoulos, V., . . . Roberts, O. W. (2022, September). Relativistic Electron
848 Precipitation by EMIC Waves: Importance of Nonlinear Resonant Effects.
849 *Geophys. Res. Lett.*, *49*(17), e99994. doi: 10.1029/2022GL099994
- 850 Hanzelka, M., & Santolík, O. (2019, June). Effects of Ducting on Whistler Mode
851 Chorus or Exohiss in the Outer Radiation Belt. *Geophys. Res. Lett.*, *46*(11),
852 5735-5745. doi: 10.1029/2019GL083115
- 853 Hanzelka, M., & Santolík, O. (2022, December). Effects of Field-Aligned Cold
854 Plasma Density Filaments on the Fine Structure of Chorus. *Geophys. Res.*
855 *Lett.*, *49*(24), e2022GL101654. doi: 10.1029/2022GL101654
- 856 Horne, R. B., Glauert, S. A., Meredith, N. P., Boscher, D., Maget, V., Heynderickx,
857 D., & Pitchford, D. (2013, April). Space weather impacts on satellites and
858 forecasting the Earth's electron radiation belts with SPACECAST. *Space*
859 *Weather*, *11*, 169-186. doi: 10.1002/swe.20023
- 860 Hosseini, P., Agapitov, O., Harid, V., & Gołkowski, M. (2021, March). Evidence of
861 Small Scale Plasma Irregularity Effects on Whistler Mode Chorus Propagation.
862 *Geophys. Res. Lett.*, *48*(5), e92850. doi: 10.1029/2021GL092850
- 863 Hsieh, Y.-K., & Omura, Y. (2017, January). Nonlinear dynamics of electrons inter-
864 acting with oblique whistler mode chorus in the magnetosphere. *J. Geophys.*
865 *Res.*, *122*, 675-694. doi: 10.1002/2016JA023255
- 866 Imhof, W. L., Reagan, J. B., & Gaines, E. E. (1977, November). Fine-scale spa-
867 tial structure in the pitch angle distributions of energetic particles near
868 the midnight trapping boundary. *J. Geophys. Res.*, *82*, 5215-5221. doi:
869 10.1029/JA082i032p05215
- 870 Jun, C. W., Yue, C., Bortnik, J., Lyons, L. R., Nishimura, Y., & Kletzing, C. (2019,
871 Mar). EMIC Wave Properties Associated With and Without Injections in
872 The Inner Magnetosphere. *Journal of Geophysical Research (Space Physics)*,
873 *124*(3), 2029-2045. doi: 10.1029/2018JA026279
- 874 Kang, N., & Bortnik, J. (2022, March). Structure of Energy Precipitation Induced
875 by Superbolt-Lightning Generated Whistler Waves. *Geophys. Res. Lett.*,
876 *49*(5), e2022GL097770. doi: 10.1029/2022GL097770
- 877 Kang, N., Bortnik, J., Zhang, X., Claudepierre, S., & Shi, X. (2022, Decem-
878 ber). Relativistic Microburst Scale Size Induced by a Single Point-Source
879 Chorus Element. *Geophys. Res. Lett.*, *49*(23), e2022GL100841. doi:
880 10.1029/2022GL100841
- 881 Katoh, Y., Omura, Y., & Summers, D. (2008, November). Rapid energization of
882 radiation belt electrons by nonlinear wave trapping. *Annales Geophysicae*, *26*,
883 3451-3456. doi: 10.5194/angeo-26-3451-2008
- 884 Ke, Y., Chen, L., Gao, X., Lu, Q., Wang, X., Chen, R., . . . Wang, S. (2021, April).
885 Whistler Mode Waves Trapped by Density Irregularities in the Earth's Magne-
886 tosphere. *Geophys. Res. Lett.*, *48*(7), e92305. doi: 10.1029/2020GL092305
- 887 Ke, Y., Gao, X., Lu, Q., Wang, X., Chen, R., Chen, H., & Wang, S. (2022,
888 February). Deformation of Electron Distributions Due to Landau Trap-
889 ping by the Whistler-Mode Wave. *Geophys. Res. Lett.*, *49*(3), e96428. doi:
890 10.1029/2021GL096428
- 891 Ke, Y., Gao, X., Lu, Q., Wang, X., & Wang, S. (2017). Generation of rising-tone
892 chorus in a two-dimensional mirror field by using the general curvilinear pic
893 code. *J. Geophys. Res.*. Retrieved from [http://dx.doi.org/10.1002/](http://dx.doi.org/10.1002/2017JA024178)
894 [2017JA024178](http://dx.doi.org/10.1002/2017JA024178) doi: 10.1002/2017JA024178
- 895 Kennel, C. F., & Engelmann, F. (1966, November). Velocity Space Diffusion from
896 Weak Plasma Turbulence in a Magnetic Field. *Physics of Fluids*, *9*, 2377-2388.
897 doi: 10.1063/1.1761629
- 898 Kennel, C. F., & Petschek, H. E. (1966, January). Limit on Stably Trapped Particle

- 899 Fluxes. *J. Geophys. Res.*, *71*, 1-28.
- 900 Khazanov, G. V., Glocer, A., & Himwich, E. W. (2014, Jan). Magnetosphere-
901 ionosphere energy interchange in the electron diffuse aurora. *Journal of*
902 *Geophysical Research (Space Physics)*, *119*(1), 171-184. doi: 10.1002/
903 2013JA019325
- 904 Khazanov, G. V., Robinson, R. M., Zesta, E., Sibeck, D. G., Chu, M., & Grubbs,
905 G. A. (2018, July). Impact of Precipitating Electrons and Magnetosphere-
906 Ionosphere Coupling Processes on Ionospheric Conductance. *Space Weather*,
907 *16*(7), 829-837. doi: 10.1029/2018SW001837
- 908 Kim, H., Schiller, Q., Engebretson, M. J., Noh, S., Kuzichev, I., Lanzerotti, L. J.,
909 ... Fromm, T. (2021, February). Observations of Particle Loss due to Injec-
910 tion Associated Electromagnetic Ion Cyclotron Waves. *Journal of Geophysical*
911 *Research (Space Physics)*, *126*(2), e28503. doi: 10.1029/2020JA028503
- 912 Kitahara, M., & Katoh, Y. (2019, Jul). Anomalous Trapping of Low Pitch Angle
913 Electrons by Coherent Whistler Mode Waves. *J. Geophys. Res.*, *124*(7), 5568-
914 5583. doi: 10.1029/2019JA026493
- 915 Kong, Z., Gao, X., Chen, H., Lu, Q., Chen, R., Ke, Y., & Wang, S. (2021, Novem-
916 ber). The Correlation Between Whistler Mode Waves and Electron Beam-
917 Like Distribution: Test Particle Simulations and THEMIS Observations.
918 *Journal of Geophysical Research (Space Physics)*, *126*(11), e29834. doi:
919 10.1029/2021JA029834
- 920 Lam, M. M., Horne, R. B., Meredith, N. P., Glauert, S. A., Moffat-Griffin, T., &
921 Green, J. C. (2010). Origin of energetic electron precipitation; 30 keV into the
922 atmosphere. *Journal of Geophysical Research: Space Physics*, *115*(A4).
- 923 Li, W., & Hudson, M. K. (2019, Nov). Earth's Van Allen Radiation Belts: From
924 Discovery to the Van Allen Probes Era. *Journal of Geophysical Research*
925 *(Space Physics)*, *124*(11), 8319-8351. doi: 10.1029/2018JA025940
- 926 Li, W., Mourenas, D., Artemyev, A. V., Bortnik, J., Thorne, R. M., Kletzing, C. A.,
927 ... Spence, H. E. (2016, September). Unraveling the excitation mechanisms of
928 highly oblique lower band chorus waves. *Geophys. Res. Lett.*, *43*, 8867-8875.
929 doi: 10.1002/2016GL070386
- 930 Li, W., Ni, B., Thorne, R. M., Bortnik, J., Green, J. C., Kletzing, C. A., ... Hospo-
931 darsky, G. B. (2013, September). Constructing the global distribution of
932 chorus wave intensity using measurements of electrons by the POES satellites
933 and waves by the Van Allen Probes. *Geophys. Res. Lett.*, *40*, 4526-4532. doi:
934 10.1002/grl.50920
- 935 Li, W., Santolik, O., Bortnik, J., Thorne, R. M., Kletzing, C. A., Kurth, W. S., &
936 Hospodarsky, G. B. (2016, May). New chorus wave properties near the equator
937 from Van Allen Probes wave observations. *Geophys. Res. Lett.*, *43*, 4725-4735.
938 doi: 10.1002/2016GL068780
- 939 Li, W., Thorne, R. M., Bortnik, J., Nishimura, Y., Angelopoulos, V., Chen, L.,
940 ... Bonnell, J. W. (2010, December). Global distributions of suprathermal
941 electrons observed on THEMIS and potential mechanisms for access into the
942 plasmasphere. *J. Geophys. Res.*, *115*, 0. doi: 10.1029/2010JA015687
- 943 Li, W., Thorne, R. M., Ma, Q., Ni, B., Bortnik, J., Baker, D. N., ... Claudepierre,
944 S. G. (2014, June). Radiation belt electron acceleration by chorus waves
945 during the 17 March 2013 storm. *J. Geophys. Res.*, *119*, 4681-4693. doi:
946 10.1002/2014JA019945
- 947 Li, W., Thorne, R. M., Nishimura, Y., Bortnik, J., Angelopoulos, V., McFadden,
948 J. P., ... Auster, U. (2010, June). THEMIS analysis of observed equatorial
949 electron distributions responsible for the chorus excitation. *J. Geophys. Res.*,
950 *115*. doi: 10.1029/2009JA014845
- 951 Lorentzen, K. R., Blake, J. B., Inan, U. S., & Bortnik, J. (2001, April). Obser-
952 vations of relativistic electron microbursts in association with VLF chorus. *J.*
953 *Geophys. Res.*, *106*(A4), 6017-6028. doi: 10.1029/2000JA003018

- 954 Lyons, L. R., Thorne, R. M., & Kennel, C. F. (1972). Pitch-angle diffusion of radi-
 955 ation belt electrons within the plasmasphere. *J. Geophys. Res.*, *77*, 3455-3474.
 956 doi: 10.1029/JA077i019p03455
- 957 Ma, Q., Artemyev, A. V., Mourenas, D., Li, W., Thorne, R. M., Kletzing, C. A., ...
 958 Wygant, J. (2017, December). Very Oblique Whistler Mode Propagation in
 959 the Radiation Belts: Effects of Hot Plasma and Landau Damping. *Geophys.*
 960 *Res. Lett.*, *44*(24), 12,057-12,066. doi: 10.1002/2017GL075892
- 961 Ma, Q., Gu, W., Claudepierre, S. G., Li, W., Bortnik, J., Hua, M., & Shen, X. C.
 962 (2022, June). Electron Scattering by Very-Low-Frequency and Low-Frequency
 963 Waves From Ground Transmitters in the Earth's Inner Radiation Belt and Slot
 964 Region. *Journal of Geophysical Research (Space Physics)*, *127*(6), e30349. doi:
 965 10.1029/2022JA030349
- 966 Ma, Q., Li, W., Bortnik, J., Thorne, R. M., Chu, X., Ozeke, L. G., ... Claudepierre,
 967 S. G. (2018, March). Quantitative Evaluation of Radial Diffusion and Local
 968 Acceleration Processes During GEM Challenge Events. *Journal of Geophysical*
 969 *Research (Space Physics)*, *123*(3), 1938-1952. doi: 10.1002/2017JA025114
- 970 Ma, Q., Li, W., Thorne, R. M., Ni, B., Kletzing, C. A., Kurth, W. S., ... An-
 971 gelopoulos, V. (2015, February). Modeling inward diffusion and slow decay
 972 of energetic electrons in the Earth's outer radiation belt. *Geophys. Res. Lett.*,
 973 *42*, 987-995. doi: 10.1002/2014GL062977
- 974 Ma, Q., Ni, B., Tao, X., & Thorne, R. M. (2012, April). Evolution of the plasma
 975 sheet electron pitch angle distribution by whistler-mode chorus waves
 976 in non-dipole magnetic fields. *Annales Geophysicae*, *30*, 751-760. doi:
 977 10.5194/angeo-30-751-2012
- 978 Malaspina, D. M., Ukhorskiy, A., Chu, X., & Wygant, J. (2018, April). A Cen-
 979 sus of Plasma Waves and Structures Associated With an Injection Front
 980 in the Inner Magnetosphere. *J. Geophys. Res.*, *123*, 2566-2587. doi:
 981 10.1002/2017JA025005
- 982 Maxworth, A. S., & Golkowski, M. (2017). Magnetospheric whistler mode
 983 ray tracing in a warm background plasma with finite electron and ion
 984 temperature. *J. Geophys. Res.*, *122*(7), 7323-7335. Retrieved from
 985 <http://dx.doi.org/10.1002/2016JA023546> doi: 10.1002/2016JA023546
- 986 Meredith, N. P., Horne, R. B., & Anderson, R. R. (2001, July). Substorm de-
 987 pendence of chorus amplitudes: Implications for the acceleration of elec-
 988 trons to relativistic energies. *J. Geophys. Res.*, *106*, 13165-13178. doi:
 989 10.1029/2000JA900156
- 990 Meredith, N. P., Horne, R. B., Shen, X.-C., Li, W., & Bortnik, J. (2020). Global
 991 model of whistler mode chorus in the near-equatorial region ($|\lambda_m| < 18^\circ$).
 992 *Geophys. Res. Lett.*, *47*, e2020GL087311. doi: 10.1029/2020GL087311
- 993 Meredith, N. P., Horne, R. B., Sicard-Piet, A., Boscher, D., Yearby, K. H., Li, W., &
 994 Thorne, R. M. (2012, October). Global model of lower band and upper band
 995 chorus from multiple satellite observations. *J. Geophys. Res.*, *117*, 10225. doi:
 996 10.1029/2012JA017978
- 997 Meredith, N. P., Horne, R. B., Thorne, R. M., & Anderson, R. R. (2003, August).
 998 Favored regions for chorus-driven electron acceleration to relativistic energies
 999 in the Earth's outer radiation belt. *Geophys. Res. Lett.*, *30*(16), 160000-1. doi:
 1000 10.1029/2003GL017698
- 1001 Millan, R. M., & Baker, D. N. (2012, November). Acceleration of Particles to High
 1002 Energies in Earth's Radiation Belts. *Space Sci. Rev.*, *173*, 103-131. doi: 10
 1003 .1007/s11214-012-9941-x
- 1004 Millan, R. M., & Thorne, R. M. (2007, March). Review of radiation belt relativistic
 1005 electron losses. *Journal of Atmospheric and Solar-Terrestrial Physics*, *69*, 362-
 1006 377. doi: 10.1016/j.jastp.2006.06.019
- 1007 Min, K., Liu, K., & Li, W. (2014, July). Signatures of electron Landau resonant
 1008 interactions with chorus waves from THEMIS observations. *J. Geophys. Res.*,

- 1009 119, 5551-5560. doi: 10.1002/2014JA019903
- 1010 Mourenas, D., Artemyev, A. V., Agapitov, O. V., & Krasnoselskikh, V. (2014,
1011 April). Consequences of geomagnetic activity on energization and loss of radi-
1012 ation belt electrons by oblique chorus waves. *J. Geophys. Res.*, *119*, 2775-2796.
1013 doi: 10.1002/2013JA019674
- 1014 Mourenas, D., Artemyev, A. V., Agapitov, O. V., Krasnoselskikh, V., & Li, W.
1015 (2014, December). Approximate analytical solutions for the trapped electron
1016 distribution due to quasi-linear diffusion by whistler mode waves. *J. Geophys.*
1017 *Res.*, *119*, 9962-9977. doi: 10.1002/2014JA020443
- 1018 Mourenas, D., Artemyev, A. V., Agapitov, O. V., Krasnoselskikh, V., & Mozer, F. S.
1019 (2015). Very oblique whistler generation by low-energy electron streams. *J.*
1020 *Geophys. Res.*, *120*, 3665-3683. doi: 10.1002/2015JA021135
- 1021 Mourenas, D., Artemyev, A. V., Ripoll, J.-F., Agapitov, O. V., & Krasnoselskikh,
1022 V. V. (2012). Timescales for electron quasi-linear diffusion by parallel and
1023 oblique lower-band Chorus waves. *J. Geophys. Res.*, *117*, A06234. doi:
1024 10.1029/2012JA017717
- 1025 Mourenas, D., Artemyev, A. V., Zhang, X. J., & Angelopoulos, V. (2022, Novem-
1026 ber). Extreme Energy Spectra of Relativistic Electron Flux in the Outer
1027 Radiation Belt. *Journal of Geophysical Research (Space Physics)*, *127*(11),
1028 e2022JA031038. doi: 10.1029/2022JA031038
- 1029 Mourenas, D., Artemyev, A. V., Zhang, X. J., & Angelopoulos, V. (2023, Au-
1030 gust). Upper Limit on Outer Radiation Belt Electron Flux Based on Dynam-
1031 ical Equilibrium. *Journal of Geophysical Research (Space Physics)*, *128*(8),
1032 e2023JA031676. doi: 10.1029/2023JA031676
- 1033 Mourenas, D., Artemyev, A. V., Zhang, X. J., Angelopoulos, V., Tsai, E., &
1034 Wilkins, C. (2021, November). Electron Lifetimes and Diffusion Rates
1035 Inferred From ELFIN Measurements at Low Altitude: First Results.
1036 *Journal of Geophysical Research (Space Physics)*, *126*(11), e29757. doi:
1037 10.1029/2021JA029757
- 1038 Mourenas, D., & Ripoll, J.-F. (2012). Analytical estimates of quasi-linear diffusion
1039 coefficients and electron lifetimes in the inner radiation belt. *J. Geophys. Res.*,
1040 *117*, A01204. doi: 10.1029/2011JA016985
- 1041 Mourenas, D., Zhang, X. J., Nunn, D., Artemyev, A. V., Angelopoulos, V., Tsai, E.,
1042 & Wilkins, C. (2022, May). Short Chorus Wave Packets: Generation Within
1043 Chorus Elements, Statistics, and Consequences on Energetic Electron Precipi-
1044 tation. *Journal of Geophysical Research (Space Physics)*, *127*(5), e30310. doi:
1045 10.1029/2022JA030310
- 1046 Mozer, F. S., Agapitov, O., Artemyev, A., Drake, J. F., Krasnoselskikh, V., Lejosne,
1047 S., & Vasko, I. (2015). Time domain structures: What and where they are,
1048 what they do, and how they are made. *Geophys. Res. Lett.*, *42*, 3627-3638.
1049 doi: 10.1002/2015GL063946
- 1050 Ni, B., Li, W., Thorne, R. M., Bortnik, J., Green, J. C., Kletzing, C. A., . . . Soria-
1051 Santacruz Pich, M. (2014, July). A novel technique to construct the global
1052 distribution of whistler mode chorus wave intensity using low-altitude POES
1053 electron data. *J. Geophys. Res.*, *119*, 5685-5699. doi: 10.1002/2014JA019935
- 1054 Ni, B., Thorne, R. M., Meredith, N. P., Shprits, Y. Y., & Horne, R. B. (2011, Octo-
1055 ber). Diffuse auroral scattering by whistler mode chorus waves: Dependence on
1056 wave normal angle distribution. *J. Geophys. Res.*, *116*, 10207. doi: 10.1029/
1057 2011JA016517
- 1058 Ni, B., Thorne, R. M., Shprits, Y. Y., & Bortnik, J. (2008, June). Resonant
1059 scattering of plasma sheet electrons by whistler-mode chorus: Contribu-
1060 tion to diffuse auroral precipitation. *Geophys. Res. Lett.*, *35*, 11106. doi:
1061 10.1029/2008GL034032
- 1062 O'Brien, T. P., Looper, M. D., & Blake, J. B. (2004, February). Quantification of
1063 relativistic electron microburst losses during the GEM storms. *Geophys. Res.*

- 1064 *Lett.*, 31(4), L04802. doi: 10.1029/2003GL018621
- 1065 O'Brien, T. P., & Moldwin, M. B. (2003, February). Empirical plasmopause
1066 models from magnetic indices. *Geophys. Res. Lett.*, 30, 1152. doi:
1067 10.1029/2002GL016007
- 1068 Olfier, L., Mann, I. R., Boyd, A. J., Ozeke, L. G., & Choi, D. (2018, May). On
1069 the Role of Last Closed Drift Shell Dynamics in Driving Fast Losses and Van
1070 Allen Radiation Belt Extinction. *J. Geophys. Res.*, 123, 3692-3703. doi:
1071 10.1029/2018JA025190
- 1072 Omura, Y., Furuya, N., & Summers, D. (2007, June). Relativistic turning ac-
1073 celeration of resonant electrons by coherent whistler mode waves in a dipole
1074 magnetic field. *J. Geophys. Res.*, 112, 6236. doi: 10.1029/2006JA012243
- 1075 Omura, Y., Miyashita, Y., Yoshikawa, M., Summers, D., Hikishima, M., Ebihara, Y.,
1076 & Kubota, Y. (2015, November). Formation process of relativistic electron flux
1077 through interaction with chorus emissions in the Earth's inner magnetosphere.
1078 *J. Geophys. Res.*, 120, 9545-9562. doi: 10.1002/2015JA021563
- 1079 Orlova, K. G., & Shprits, Y. Y. (2011, September). On the bounce-averaging of scat-
1080 tering rates and the calculation of bounce period. *Physics of Plasmas*, 18(9),
1081 092904. doi: 10.1063/1.3638137
- 1082 Rackauckas, C., & Nie, Q. (2017). Differentialequations.jl—a performant and feature-
1083 rich ecosystem for solving differential equations in julia. *Journal of Open Re-
1084 search Software*, 5(1).
- 1085 Runov, A., Angelopoulos, V., Gabrielse, C., Liu, J., Turner, D. L., & Zhou, X.-Z.
1086 (2015, June). Average thermodynamic and spectral properties of plasma in
1087 and around dipolarizing flux bundles. *J. Geophys. Res.*, 120, 4369-4383. doi:
1088 10.1002/2015JA021166
- 1089 Sauer, K., Baumgaerte, K., & Sydora, R. D. (2020). Gap formation around $\omega_e/2$
1090 and generation of low-band whistler waves by landau-resonant electrons in
1091 the magnetosphere: Predictions from dispersion theory. *Earth and Planetary
1092 Physics*, 4, 138. Retrieved from [http://eppcgs.xml-journal.net//article/
1093 id/3c6a82bf-66b3-436e-94ce-bc744f2e3c29](http://eppcgs.xml-journal.net//article/id/3c6a82bf-66b3-436e-94ce-bc744f2e3c29) doi: 10.26464/epp2020020
- 1094 Sergeev, V. A., Sazhina, E. M., Tsyganenko, N. A., Lundblad, J. A., & Soraas, F.
1095 (1983, October). Pitch-angle scattering of energetic protons in the magne-
1096 totail current sheet as the dominant source of their isotropic precipitation
1097 into the nightside ionosphere. *Planetary Space Science*, 31, 1147-1155. doi:
1098 10.1016/0032-0633(83)90103-4
- 1099 Sheeley, B. W., Moldwin, M. B., Rassoul, H. K., & Anderson, R. R. (2001, Novem-
1100 ber). An empirical plasmasphere and trough density model: CRRES observa-
1101 tions. *J. Geophys. Res.*, 106, 25631-25642. doi: 10.1029/2000JA000286
- 1102 Shen, X.-C., Li, W., Capannolo, L., Ma, Q., Qin, M., Artemyev, A. V., ... Huang,
1103 S. (2023, April). Modulation of Energetic Electron Precipitation Driven
1104 by Three Types of Whistler Mode Waves. *Geophys. Res. Lett.*, 50(8),
1105 e2022GL101682. doi: 10.1029/2022GL101682
- 1106 Shen, Y., Chen, L., Zhang, X.-J., Artemyev, A., Angelopoulos, V., Cully, C. M., ...
1107 Horne, R. B. (2021, December). Conjugate Observation of Magnetospheric
1108 Chorus Propagating to the Ionosphere by Ducting. *Geophys. Res. Lett.*,
1109 48(23), e95933. doi: 10.1029/2021GL095933
- 1110 Shklyar, D. R. (2021, February). A Theory of Interaction Between Relativistic Elec-
1111 trons and Magnetospherically Reflected Whistlers. *Journal of Geophysical Re-
1112 search (Space Physics)*, 126(2), e28799. doi: 10.1029/2020JA028799
- 1113 Shklyar, D. R., & Matsumoto, H. (2009, April). Oblique Whistler-Mode Waves
1114 in the Inhomogeneous Magnetospheric Plasma: Resonant Interactions with
1115 Energetic Charged Particles. *Surveys in Geophysics*, 30, 55-104. doi:
1116 10.1007/s10712-009-9061-7
- 1117 Shprits, Y. Y., & Ni, B. (2009, November). Dependence of the quasi-linear scatter-
1118 ing rates on the wave normal distribution of chorus waves. *J. Geophys. Res.*,

- 1119 114, 11205. doi: 10.1029/2009JA014223
- 1120 Shprits, Y. Y., Subbotin, D. A., Meredith, N. P., & Elkington, S. R. (2008, Novem-
1121 ber). Review of modeling of losses and sources of relativistic electrons in the
1122 outer radiation belt II: Local acceleration and loss. *Journal of Atmospheric
1123 and Solar-Terrestrial Physics*, *70*, 1694-1713. doi: 10.1016/j.jastp.2008.06.014
- 1124 Shprits, Y. Y., Thorne, R. M., Friedel, R., Reeves, G. D., Fennell, J., Baker, D. N.,
1125 & Kanekal, S. G. (2006, November). Outward radial diffusion driven by losses
1126 at magnetopause. *J. Geophys. Res.*, *111*, 11214. doi: 10.1029/2006JA011657
- 1127 Shumko, M., Turner, D. L., O'Brien, T. P., Claudepierre, S. G., Sample, J., Hartley,
1128 D. P., ... Mitchell, D. G. (2018, August). Evidence of Microbursts Observed
1129 Near the Equatorial Plane in the Outer Van Allen Radiation Belt. *Geophys.
1130 Res. Lett.*, *45*(16), 8044-8053. doi: 10.1029/2018GL078451
- 1131 Stix, T. H. (1962). *The Theory of Plasma Waves*.
- 1132 Summers, D., Ma, C., Meredith, N. P., Horne, R. B., Thorne, R. M., & Anderson,
1133 R. R. (2004, January). Modeling outer-zone relativistic electron response to
1134 whistler-mode chorus activity during substorms. *Journal of Atmospheric and
1135 Solar-Terrestrial Physics*, *66*, 133-146. doi: 10.1016/j.jastp.2003.09.013
- 1136 Summers, D., & Ni, B. (2008, July). Effects of latitudinal distributions of particle
1137 density and wave power on cyclotron resonant diffusion rates of radiation belt
1138 electrons. *Earth, Planets, and Space*, *60*, 763-771.
- 1139 Summers, D., Ni, B., & Meredith, N. P. (2007, April). Timescales for radiation belt
1140 electron acceleration and loss due to resonant wave-particle interactions: 1.
1141 Theory. *J. Geophys. Res.*, *112*, 4206. doi: 10.1029/2006JA011801
- 1142 Tao, X., Bortnik, J., Albert, J. M., & Thorne, R. M. (2012, October). Comparison
1143 of bounce-averaged quasi-linear diffusion coefficients for parallel propagating
1144 whistler mode waves with test particle simulations. *J. Geophys. Res.*, *117*,
1145 10205. doi: 10.1029/2012JA017931
- 1146 Tao, X., Thorne, R. M., Li, W., Ni, B., Meredith, N. P., & Horne, R. B. (2011,
1147 April). Evolution of electron pitch angle distributions following injection
1148 from the plasma sheet. *J. Geophys. Res.*, *116*, A04229. doi: 10.1029/
1149 2010JA016245
- 1150 Thorne, R. M. (1980, March). The importance of energetic particle precipitation
1151 on the chemical composition of the middle atmosphere. *Pure and Applied Geo-
1152 physics*, *118*(1), 128-151. doi: 10.1007/BF01586448
- 1153 Thorne, R. M. (2010, November). Radiation belt dynamics: The importance of
1154 wave-particle interactions. *Geophys. Res. Lett.*, *37*(2), 22107. doi: 10.1029/
1155 2010GL044990
- 1156 Thorne, R. M., Li, W., Ni, B., Ma, Q., Bortnik, J., Chen, L., ... Kanekal, S. G.
1157 (2013, December). Rapid local acceleration of relativistic radiation-
1158 belt electrons by magnetospheric chorus. *Nature*, *504*, 411-414. doi:
1159 10.1038/nature12889
- 1160 Thorne, R. M., O'Brien, T. P., Shprits, Y. Y., Summers, D., & Horne, R. B. (2005,
1161 September). Timescale for MeV electron microburst loss during geomagnetic
1162 storms. *J. Geophys. Res.*, *110*, 9202. doi: 10.1029/2004JA010882
- 1163 Tsai, E. (2023, June). *ethantsai/nlwhistlers:jgr2023*. Zenodo. Retrieved from
1164 <https://doi.org/10.5281/zenodo.8083874> (Software) doi: 10.5281/zenodo
1165 .8083874
- 1166 Tsai, E., Artemyev, A., Angelopoulos, V., & Zhang, X.-J. (2023, August). In-
1167 vestigating Whistler-Mode Wave Intensity Along Field Lines Using Electron
1168 Precipitation Measurements. *Journal of Geophysical Research (Space Physics)*,
1169 *128*(8), e2023JA031578. doi: 10.1029/2023JA031578
- 1170 Tsai, E., Artemyev, A., Zhang, X.-J., & Angelopoulos, V. (2022, May). Relativistic
1171 Electron Precipitation Driven by Nonlinear Resonance With Whistler-Mode
1172 Waves. *Journal of Geophysical Research (Space Physics)*, *127*(5), e30338. doi:
1173 10.1029/2022JA030338

- 1174 Tsyganenko, N. A. (1989, January). A magnetospheric magnetic field model with
 1175 a warped tail current sheet. *Planetary Space Science*, *37*, 5-20. doi: 10.1016/
 1176 0032-0633(89)90066-4
- 1177 Turner, D. L., Angelopoulos, V., Li, W., Bortnik, J., Ni, B., Ma, Q., ... Rodriguez,
 1178 J. V. (2014, March). Competing source and loss mechanisms due to wave-
 1179 particle interactions in Earth's outer radiation belt during the 30 September to
 1180 3 October 2012 geomagnetic storm. *J. Geophys. Res.*, *119*, 1960-1979. doi:
 1181 10.1002/2014JA019770
- 1182 Turunen, E., Kero, A., Verronen, P. T., Miyoshi, Y., Oyama, S.-I., & Saito, S.
 1183 (2016). Mesospheric ozone destruction by high-energy electron precipitation as-
 1184 sociated with pulsating aurora. *Journal of Geophysical Research: Atmospheres*,
 1185 *121*(19), 11–852.
- 1186 Vainchtein, D., Zhang, X. J., Artemyev, A. V., Mourenas, D., Angelopoulos, V.,
 1187 & Thorne, R. M. (2018, October). Evolution of Electron Distribution
 1188 Driven by Nonlinear Resonances With Intense Field-Aligned Chorus Waves.
 1189 *Journal of Geophysical Research (Space Physics)*, *123*(10), 8149-8169. doi:
 1190 10.1029/2018JA025654
- 1191 Vasko, I. Y., Agapitov, O. V., Mozer, F. S., Artemyev, A. V., Drake, J. F., &
 1192 Kuzichev, I. V. (2017, January). Electron holes in the outer radiation belt:
 1193 Characteristics and their role in electron energization. *J. Geophys. Res.*, *122*,
 1194 120-135. doi: 10.1002/2016JA023083
- 1195 Vasko, I. Y., Agapitov, O. V., Mozer, F. S., Bonnell, J. W., Artemyev, A. V., Kras-
 1196 noselskikh, V. V., ... Hospodarsky, G. (2017, May). Electron-acoustic solitons
 1197 and double layers in the inner magnetosphere. *Geophys. Res. Lett.*, *44*, 4575-
 1198 4583. doi: 10.1002/2017GL074026
- 1199 Verkhoglyadova, O. P., Tsurutani, B. T., & Lakhina, G. S. (2010, September). Prop-
 1200 erties of obliquely propagating chorus. *Journal of Geophysical Research (Space*
 1201 *Physics)*, *115*(1), A00F19. doi: 10.1029/2009JA014809
- 1202 Walsh, B. M., Hull, A. J., Agapitov, O., Mozer, F. S., & Li, H. (2020). A census of
 1203 magnetospheric electrons from several ev to 30 kev. *Journal of Geophysical Re-*
 1204 *search: Space Physics*, *125*(5), e2019JA027577. Retrieved from [https://](https://agupubs.onlinelibrary.wiley.com/doi/abs/10.1029/2019JA027577)
 1205 agupubs.onlinelibrary.wiley.com/doi/abs/10.1029/2019JA027577
 1206 (e2019JA027577 10.1029/2019JA027577) doi: 10.1029/2019JA027577
- 1207 Wang, D., & Shprits, Y. Y. (2019, July). On How High-Latitude Chorus Waves Tip
 1208 the Balance Between Acceleration and Loss of Relativistic Electrons. *Geophys.*
 1209 *Res. Lett.*, *46*(14), 7945-7954. doi: 10.1029/2019GL082681
- 1210 Watt, C. E. J., Degeling, A. W., & Rankin, R. (2013, May). Constructing the fre-
 1211 quency and wave normal distribution of whistler-mode wave power. *J. Geo-*
 1212 *phys. Res.*, *118*, 1984-1991. doi: 10.1002/jgra.50231
- 1213 Wilkins, C., Angelopoulos, V., Runov, A., Artemyev, A., Zhang, X. J., Liu, J.,
 1214 & Tsai, E. (2023, October). Statistical Characteristics of the Electron
 1215 Isotropy Boundary. *Journal of Geophysical Research (Space Physics)*, *128*(10),
 1216 e2023JA031774. doi: 10.1029/2023JA031774
- 1217 Xiang, Z., Tu, W., Ni, B., Henderson, M. G., & Cao, X. (2018, August). A Statis-
 1218 tical Survey of Radiation Belt Dropouts Observed by Van Allen Probes. *Geo-*
 1219 *phys. Res. Lett.*, *45*, 8035-8043. doi: 10.1029/2018GL078907
- 1220 Xu, W., Marshall, R. A., Tyssøy, H. N., & Fang, X. (2020). A generalized method
 1221 for calculating atmospheric ionization by energetic electron precipitation. *Jour-*
 1222 *nal of Geophysical Research: Space Physics*, *125*(11), e2020JA028482.
- 1223 Yahnin, A. G., Yahnina, T. A., Raita, T., & Manninen, J. (2017, September).
 1224 Ground pulsation magnetometer observations conjugated with relativistic elec-
 1225 tron precipitation. *Journal of Geophysical Research (Space Physics)*, *122*(9),
 1226 9169-9182. doi: 10.1002/2017JA024249
- 1227 Yahnin, A. G., Yahnina, T. A., Semenova, N. V., Gvozdevsky, B. B., & Pashin,
 1228 A. B. (2016, September). Relativistic electron precipitation as seen by NOAA

- 1229 POES. *Journal of Geophysical Research (Space Physics)*, *121*(9), 8286-8299.
1230 doi: 10.1002/2016JA022765
- 1231 Zhang, X., Angelopoulos, V., Artemyev, A. V., & Liu, J. (2018, September).
1232 Whistler and Electron Firehose Instability Control of Electron Distributions in
1233 and Around Dipolarizing Flux Bundles. *Geophys. Res. Lett.*, *45*, 9380-9389.
1234 doi: 10.1029/2018GL079613
- 1235 Zhang, X.-J., Angelopoulos, V., Artemyev, A., Mourenas, D., Agapitov, O., Tsai,
1236 E., & Wilkins, C. (2023, January). Temporal Scales of Electron Precipitation
1237 Driven by Whistler-Mode Waves. *Journal of Geophysical Research (Space*
1238 *Physics)*, *128*(1), e2022JA031087. doi: 10.1029/2022JA031087
- 1239 Zhang, X.-J., Angelopoulos, V., Mourenas, D., Artemyev, A., Tsai, E., & Wilkins,
1240 C. (2022, May). Characteristics of Electron Microburst Precipitation Based
1241 on High-Resolution ELFIN Measurements. *Journal of Geophysical Research*
1242 *(Space Physics)*, *127*(5), e30509. doi: 10.1029/2022JA030509
- 1243 Zhang, X. J., Thorne, R., Artemyev, A., Mourenas, D., Angelopoulos, V., Bortnik,
1244 J., ... Hospodarsky, G. B. (2018, July). Properties of Intense Field-Aligned
1245 Lower-Band Chorus Waves: Implications for Nonlinear Wave-Particle Inter-
1246 actions. *Journal of Geophysical Research (Space Physics)*, *123*(7), 5379-5393.
1247 doi: 10.1029/2018JA025390

Key factors determining nightside energetic electron losses driven by whistler-mode waves

Ethan Tsai¹, Anton Artemyev¹, Qianli Ma^{2,3}, Didier Mourenas^{4,5}, Oleksiy Agapitov⁶, Xiao-Jia Zhang^{7,1}, Vassilis Angelopoulos¹

¹Earth, Planetary, and Space Sciences, University of California, Los Angeles, Los Angeles, CA 90095, USA

²Department of Atmospheric and Oceanic Sciences, University of California, Los Angeles, Los Angeles, USA

³Boston University, Boston, MA, United States

⁴CEA, DAM, DIF, Arpajon, France

⁵Laboratoire Matière en Conditions Extrêmes, Paris-Saclay University, CEA, Bruyères-le-Châtel, France

⁶Space Sciences Laboratory, University of California, Berkeley, CA, USA

⁷Department of Physics, The University of Texas at Dallas, Richardson, TX, USA

Key Points:

- Comparing ELFIN data with test particle and quasi-linear simulations, we investigate whistler-driven electron precipitation on the nightside
- A reduction in background plasma density is key to enabling whistler-mode waves to efficiently scatter electrons up to 1 MeV
- Decreasing wave frequency as a function of latitude and wave obliquity, are both integral to capturing realistic nightside electron losses

Corresponding author: Ethan Tsai, ethantsai@ucla.edu

Abstract

Energetic electron losses by pitch-angle scattering and precipitation to the atmosphere from the radiation belts are controlled, to a great extent, by resonant wave particle interactions with whistler-mode waves. The efficacy of such precipitation is primarily controlled by wave intensity, although its relative importance, compared to other wave and plasma parameters, remains unclear. Precipitation spectra from the low-altitude, polar-orbiting ELFİN mission have previously been demonstrated to be consistent with energetic precipitation modeling derived from empirical models of field-aligned wave power across a wide-swath of local-time sectors. However, such modeling could not explain the intense, relativistic electron precipitation observed on the nightside. Therefore, this study aims to additionally consider the contributions of three modifications – wave obliquity, frequency spectrum, and local plasma density – to explain this discrepancy on the nightside. By incorporating these effects into both test particle simulations and quasi-linear diffusion modeling, we find that realistic implementations of each individual modification result in only slight changes to the electron precipitation spectrum. However, these modifications, when combined, enable more accurate modeling of ELFİN-observed spectra. In particular, a significant reduction in plasma density enables lower frequency waves, oblique, or even quasi-field aligned waves to resonate with near ~ 1 MeV electrons closer to the equator. We demonstrate that the levels of modification required to accurately reproduce the nightside spectra of whistler-mode wave-driven relativistic electron precipitation match empirical expectations, and should therefore be included in future radiation belt modeling.

Plain Language Summary

Whistler-mode waves are a type of electromagnetic wave that mediate electron dynamics in Earth’s radiation belts and are simultaneously important for energizing electrons and driving loss mechanisms. Most radiation belt models today do not adequately capture the effects of these waves on relativistic electrons, which are important to study because these energetic electrons are often called “Killer Electrons” for their ability to degrade spacecraft electronics. Additionally, when lost into Earth’s atmosphere, these electrons can also change atmospheric chemistry and ionospheric properties, making them an important input parameters for atmospheric, ionospheric, and magnetospheric modeling. This study uses two different modeling methods to determine which properties of whistler-mode waves are most important for accurately capturing these wave-particle interactions on the nightside, where plasma interactions are more dynamic. The results agree well with statistical results from the Electron Losses and Fields INvestigation (ELFİN) mission, allowing us to fully explain the mechanisms behind whistler-mode wave-driven electron losses on the nightside.

1 Introduction

Earth’s inner magnetosphere is filled with energetic electron fluxes injected from the plasma sheet, that are then further accelerated via resonant interactions with electromagnetic whistler-mode (chorus) waves (Millan & Baker, 2012; Shprits et al., 2008). These wave-particle interactions are, in great part, also responsible for energetic electron pitch-angle scattering into the loss cone and subsequent electron loss through precipitation into Earth’s atmosphere (Millan & Thorne, 2007; Shprits et al., 2008). This contribution to both acceleration and pitch-angle scattering of energetic electrons makes the whistler-mode wave a crucial element of outer radiation belt dynamics (Bortnik & Thorne, 2007; Thorne, 2010; Li & Hudson, 2019). Not only do energetic radiation belt electrons serve as an important space weather proxy (Horne et al., 2013), relativistic electron can also penetrate deep into the thermosphere/mesosphere (Xu et al., 2020) contributing to ozone depletion (Thorne, 1980; Lam et al., 2010; Turunen et al., 2016). Un-

71 understanding the mechanisms behind the global distribution of energetic electron losses
72 is therefore important for studying radiation belt dynamics and atmospheric chemistry.

73 Energetic ($\gtrsim 100$ keV) electron losses due to whistler-mode waves is one such topic
74 that has yet to be fully investigated. It is known that these waves can scatter electrons
75 up to 1 MeV (O’Brien et al., 2004; Thorne et al., 2005; Blake & O’Brien, 2016; Shumko
76 et al., 2018; Breneman et al., 2017), which is problematic because current radiation belt
77 models typically only incorporate diffusive losses of sub-relativistic electrons (up to \sim
78 500 keV). Additionally, previous research (Tsai et al., 2023) has revealed a day-night dif-
79 ference in energetic electrons scattered by whistler-mode waves, with more intense elec-
80 tron precipitation on the dayside than on the nightside. This is attributed to two system-
81 level properties – (1) nightside regions generally have a lower plasma density and (2) night-
82 side wave activity is generally more confined to the equatorial plane (Meredith et al., 2001,
83 2003; Agapitov et al., 2013) – which both cause strong resonant wave particle interac-
84 tions to preferentially occur on the dayside, resulting in more extreme energetic electron
85 losses (e.g., Thorne et al., 2005; Mourenas, Artemyev, Agapitov, & Krasnoselskikh, 2014;
86 Wang & Shprits, 2019; Aryan et al., 2020). This is supported by Tsai et al. (2023), which
87 used modeled electron precipitation spectra derived from statistically-averaged wave in-
88 tensity distributions from Agapitov et al. (2018) to directly compare with statistical ob-
89 servations of electron precipitating fluxes from ELFIND (Angelopoulos et al., 2020). Al-
90 though these model-data comparisons showed good agreement between electron precipi-
91 tation and wave power in the dusk and daysides, ELFIND-measured nightside relativistic
92 ($\gtrsim 500$ keV) precipitating flux rates were substantially larger than anticipated (i.e.
93 modeled) and nearly comparable to that on the dayside. Understanding mechanisms that
94 can cause such intense energetic precipitation is a prerequisite for accurately modeling
95 electron loss in the radiation belts, therefore motivating the need to explore what key
96 factors actually determine nightside electron losses.

97 There are a few prime candidates that determine the efficiency of wave-particle res-
98 onant interactions (and, particularly, the energy dependence of whistler-mode wave driven
99 electron scattering):

- 100 1. Wave intensity distribution along magnetic field lines (see discussion in Thorne
101 et al., 2005; Wang & Shprits, 2019).
- 102 2. Obliquity of wave propagation relative to the background magnetic field (see dis-
103 cussion in Lorentzen et al., 2001; Mourenas, Artemyev, Agapitov, & Krasnosel-
104 skikh, 2014; Artemyev et al., 2016).
- 105 3. Wave frequency spectrum and its variation along magnetic field lines (see discus-
106 sion in Agapitov et al., 2018)
- 107 4. Equatorial plasma density magnitude (see discussion in Thorne et al., 2013; Agapi-
108 tov et al., 2019; Allison & Shprits, 2020) and its variation along magnetic field lines
109 (see discussion in Summers & Ni, 2008; Artemyev et al., 2013).

110 Having already examined the importance of wave amplitude in Tsai et al. (2023), we now
111 study the remaining three mechanisms which could potentially modulate nightside elec-
112 tron precipitating spectra. First, intense nightside whistler-mode waves are typically as-
113 sociated with strong plasma sheet injections (Tao et al., 2011; Fu et al., 2014; X. Zhang
114 et al., 2018) which are often accompanied by the enhanced convection electric field which
115 transports cold plasma Earthward, thereby decreasing equatorial plasma density (Vasko,
116 Agapitov, Mozer, Bonnell, et al., 2017; Agapitov et al., 2019). A lower plasma density
117 results in a lower plasma frequency; a lower plasma frequency to gyrofrequency ratio,
118 f_{pe}/f_{ce} yields a higher cyclotron resonance energy $E_R \propto (f_{ce}/f_{pe})^2$ to f_{ce}/f_{pe} (from
119 low to high energy) of electrons for given wave frequencies, wave normal angles, and elec-
120 tron pitch-angles (Stix, 1962; Summers et al., 2007; Li, Thorne, Nishimura, et al., 2010;
121 Allison et al., 2021). This nightside localized density reduction can thus potentially in-
122 crease the scattering rate of relativistic electrons.

123 Second, statistical observations have shown a clear trend of average wave frequency
 124 decreasing with latitude along field lines (i.e. increasing distance from the equatorial plane)
 125 (Agapitov et al., 2018). This is likely caused by preferential Landau damping of higher-
 126 frequency waves resonating with suprathermal electrons (L. Chen et al., 2013; Watt et
 127 al., 2013; Maxworth & Golkowski, 2017). A lower normalized wave frequency f/f_{ce} means
 128 a higher cyclotron resonance energy $E_R \propto (f_{ce}/f)(1-f/f_{ce})^3$ to $(f_{ce}/f)^{1/2}(1-f/f_{ce})^{3/2}$
 129 from low to high energy (Li, Thorne, Nishimura, et al., 2010; Mourenas et al., 2012). Thus,
 130 this reduction in the mean wave frequency in the nightside off-equatorial region may also
 131 increase the scattering rate of relativistic electrons.

132 Third, plasma injections are often associated with enhanced electrostatic turbu-
 133 lence (Mozer et al., 2015; Agapitov et al., 2015; Vasko, Agapitov, Mozer, Artemyev, et
 134 al., 2017; Malaspina et al., 2018) that forms a plateau in the field-aligned velocity dis-
 135 tribution and significantly reduces Landau damping of oblique whistler-mode waves (see
 136 discussion in Mourenas et al., 2015; Ma et al., 2017; Artemyev & Mourenas, 2020). In
 137 this regime, oblique (with wave normal angles below the Gendrin angle $\theta_G \approx \text{acos}(2f/f_{ce})$)
 138 and very oblique (with wave normal angle up to the resonant cone angle $\theta_r \approx \text{acos}(f/f_{ce})$)
 139 waves may survive Landau damping (see Min et al., 2014; R. Chen et al., 2019; Sauer
 140 et al., 2020; Ke et al., 2022). These waves then become oblique off the equatorial plane
 141 (Bortnik et al., 2007; L. Chen et al., 2013), or, in more unusual cases, are generated within
 142 the equatorial source region (Artemyev et al., 2016; Li, Mourenas, et al., 2016; Agapi-
 143 tov et al., 2016). Wave obliquity not only increases the resonant interaction energy with
 144 electrons as $E_R \propto 1/k_{\parallel}^2 \propto 1/\cos^2\theta$ (e.g., Verkhoglyadova et al., 2010; Mourenas et
 145 al., 2015), but also allows for interactions with electrons at higher-order cyclotron res-
 146 onances ($n \gg 1$, e.g., Shklyar & Matsumoto, 2009; Mourenas et al., 2012; Artemyev
 147 et al., 2013; Albert, 2017) which can drastically increase the resonance energy $E_R \propto n^2$
 148 (e.g., Lorentzen et al., 2001; Gan et al., 2023). Thus, nightside whistler-mode wave obli-
 149 quity could also potentially increase the scattering rate of relativistic electrons.

150 Here, we examine each of these three mechanisms to see whether they can explain
 151 the enhanced precipitation of relativistic electrons in the nightside MLT sector using a
 152 combination of statistics from ELFIN observations (Angelopoulos et al., 2020), test par-
 153 ticle simulations (Tsai et al., 2022, 2023), and quasi-linear diffusion code (Ma et al., 2012,
 154 2015). This paper is organized as follows: Section 2 details ELFIN observations/statistics
 155 and presents observational evidence of intense nightside precipitation of relativistic elec-
 156 trons; Section 3 describes the basics of the test particle simulation and quasi-linear dif-
 157 fusion codes; Section 4 compares ELFIN data to results from a variety of runs explor-
 158 ing the three main modifications – reduced plasma density, wave obliquity, wave frequency
 159 variation along magnetic field lines; finally, Section 5 summarizes and discusses the ob-
 160 tained results.

161 2 Data Sets

162 The ELFIN CubeSats (ELFIN A and B) are identically equipped with an Ener-
 163 getic Particle Detector for Electrons (EPDE), capable of measuring energy and pitch-
 164 angle distributions of energetic electrons with $\Delta E/E = 40\%$ across 16 logarithmically
 165 spaced energy channels between 50 keV and 5 MeV (Angelopoulos et al., 2020). Spin-
 166 ning at just over 21 revolutions per minute (spin period ≈ 2.8 sec), ELFIN’s 16 sectors
 167 per spin yields a spin phase resolution of $\Delta\alpha = 22.5^\circ$. The main data product used in
 168 this study is the precipitating-to-trapped flux ratio, $j_{prec}/j_{trap}(E)$, where $j_{trap}(E)$ is the
 169 locally trapped (outside of the local bounce loss-cone) electron flux and $j_{prec}(E)$ is the
 170 flux integrated over the local loss-cone with a correction to remove the backscattered fluxes
 171 from the opposite hemisphere (see details in Mourenas et al., 2021; Angelopoulos et al.,
 172 2023). Figure 1 shows two typical examples of ELFIN outer radiation belt crossings on
 173 the nightside with $j_{trap}(E)$ (a,d) and j_{prec}/j_{trap} (b,e) distributions.

174 This study utilized 30 months (January 2020 - June 2022) of ELFIN's $j_{trap}(E)$ and
 175 $j_{prec}(E)$ measurements during strong and bursty energetic electron precipitation events
 176 (for details regarding statistical coverage, see Figure 5 in Tsai et al., 2023). In order to
 177 obtain a statistical representation of whistler-mode-driven electron precipitation, data
 178 was selected based on data quality (minimum 4 counts/second for any given energy or
 179 pitch angle bin) and precipitation intensity ($j_{prec}(E)/j_{trap}(E) > 0.5$ at ELFIN's low-
 180 est energy bin of 63 keV). In addition, there were provisions to identify and remove elec-
 181 tron precipitation events driven by field-line curvature scattering, EMIC-driven precip-
 182 itation, and microbursts. Curvature scattering (Imhof et al., 1977; Sergeev et al., 1983;
 183 Büchner & Zelenyi, 1989) of plasma sheet and radiation belt electrons can be identified
 184 by its sharp energy/latitude dispersion (isotropy boundary) that results in high precipitating-
 185 to-trapped flux ratio at relativistic energies closer to the planet (see the IB precipitat-
 186 ing pattern in Fig. 1b and statistical results in Wilkins et al. (2023)). Such data, in ad-
 187 dition to the isotropic precipitation with $j_{prec}/j_{trap} \sim 1$ of < 300 keV electrons pole-
 188 ward from the isotropy boundary (Artemyev et al., 2022), are removed from our statis-
 189 tics. Next, electromagnetic ion cyclotron (EMIC) waves, which are caused by nightside
 190 ion injections (Jun et al., 2019; Kim et al., 2021) and efficiently scatter and precipitate
 191 relativistic electrons (e.g., Blum, Halford, et al., 2015; Blum, Li, & Denton, 2015; Yah-
 192 nin et al., 2016, 2017; Capannolo et al., 2019, 2023), are excluded. These EMIC-driven
 193 observations are identified by precipitating-to-trapped ratios that reach their peak at \geq
 194 500 keV energy (see examples in X. An et al., 2022; Grach et al., 2022; Capannolo et al.,
 195 2023; Angelopoulos et al., 2023). Additionally, whistler-mode hiss waves provide a wide
 196 energy range of scattering, from weak scattering further from the plasmasphere to pre-
 197 cipitation of relativistic electrons within the plasmasphere (see discussion of ELFIN ob-
 198 servations of such precipitation in Mourenas et al., 2021; Angelopoulos et al., 2023; X.-
 199 C. Shen et al., 2023); these hiss precipitation events are also eliminated. Figure 1e shows
 200 this particular pattern, which is recognizable by a low j_{prec}/j_{trap} ratio peaking at ≥ 500
 201 keV energy at low L -shells. Finally, we exclude all precipitation patterns showing microburst-
 202 like flux variation within one spin (such events are characterized by precipitating-to-trapped
 203 flux ratio exceeding one for relativistic electron energies, see X.-J. Zhang et al., 2022, for
 204 further examples).

205 All these effects are programmatically eliminated from statistics leaving us with
 206 only one type of precipitating energy distribution: a precipitating-to-trapped ratio mono-
 207 tonically decreasing with energy, observed primarily within L -shells $\in [4, 8]$, correspond-
 208 ing to the outer radiation belt outside the plasmasphere (e.g., Mourenas et al., 2021).
 209 This type of precipitation can only be caused by whistler-mode waves (see more details
 210 and examples in Tsai et al., 2022; X.-J. Zhang et al., 2022, 2023), and is demonstrated
 211 in Figure 1(b,e).

212 We combine all ELFIN observations from the nightside MLT sector (27950 spins
 213 across 4458 radiation belt crossings) and plot the averaged precipitating-to-trapped flux
 214 spectra for three geomagnetic activity levels and two L -shell domains (4.5–5.5 and 5.5–
 215 7.5) for $AE \in [100, 300]$ nT in Fig. 2d. Fig. 2(a-c) show that the precipitating-to-trapped
 216 electron flux ratio j_{prec}/j_{trap} above 100 keV increases significantly as AE increases. The
 217 precipitating-to-trapped flux ratio reaches $j_{prec}/j_{trap} \sim 0.1$ up to 200–400 keV when
 218 $AE > 300$ nT. This result is consistent with past observations of stronger energetic elec-
 219 tron injections from the plasma sheet during periods of higher AE (Tao et al., 2011; Runov
 220 et al., 2015; Gabrielse et al., 2014), leading to even more intense whistler-mode waves
 221 (Meredith et al., 2001; X. J. Zhang et al., 2018) which can efficiently precipitate 50 –
 222 500 keV electrons (Summers et al., 2004; Thorne et al., 2005; Aryan et al., 2020; Agapi-
 223 tov et al., 2018). The ratio j_{prec}/j_{trap} is also higher at $L = 5.5–7.5$ than at $L = 4.5–$
 224 5.5 in Fig. 2, in agreement with the higher chorus wave power at higher $L > 5.0–5.5$
 225 in the night sector in spacecraft statistics (Agapitov et al., 2018; Meredith et al., 2020).
 226 The smooth decrease of j_{prec}/j_{trap} as electron energy increases in Fig. 2d is consistent
 227 with the expectation that at higher latitudes, wave power decreases while minimum cy-

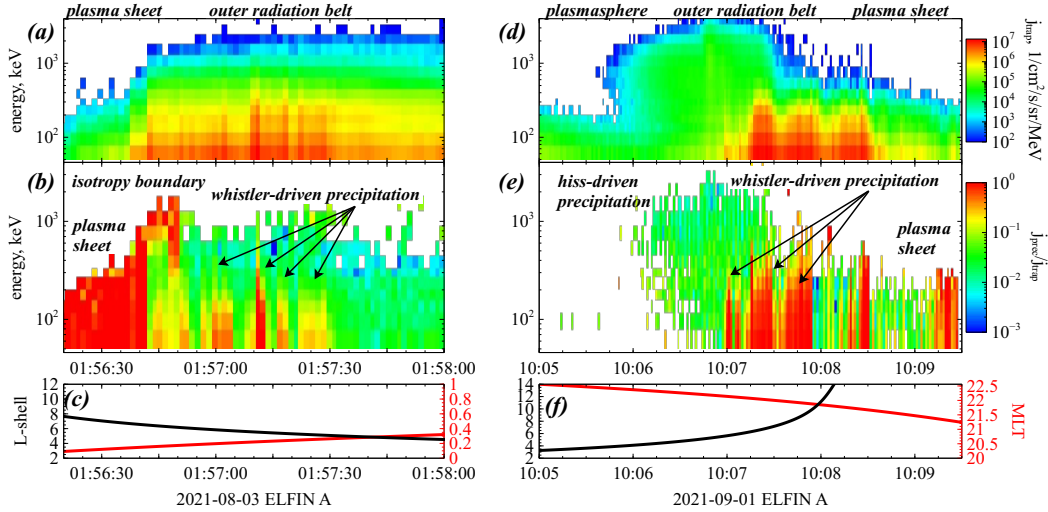


Figure 1. Two examples of ELFIN observations with strong precipitation of energetic electrons in the nightside MLT sector showing locally trapped electron fluxes (a,d), precipitating-to-trapped flux ratio (b,e), and ELFIN’s MLT, L -shell coordinates from (Tsyganenko, 1989) model (c,f).

228 electron resonance energy increases, therefore precipitating higher energy electrons at lower
 229 absolute flux levels (Agapitov et al., 2018; Meredith et al., 2020).

230 3 Simulation

231 Calculating the precipitating-to-trapped flux ratios is useful because it eliminates
 232 the trapped flux variability (which can vary by orders of magnitude). The slope of the
 233 ratio’s energy spectra now represents only the relative effects of resonant interactions with
 234 whistler-mode waves. To then compare with ELFIN statistics, we obtain modeled precipitating-
 235 to-trapped flux ratios using two different types of simulations: (1) a configurable large-
 236 ensemble test particle simulation for electron resonant interactions, as used in previous
 237 work (Tsai et al., 2022, 2023) and (2) a quasi-linear diffusion code which has been used
 238 in previous radiation belt simulations (Ma et al., 2012, 2015). The test particle simu-
 239 lations include potential non-linear resonant effects and consider only purely monochro-
 240 matic waves, whereas the quasi-linear diffusion code models electron scattering by an en-
 241 semble of oblique waves with higher order resonant interactions across a distribution of
 242 frequencies. Thus, by comparing results obtained by these two approaches, we can fully
 243 capture the importance of different resonant effects for electron scattering and losses.

244 3.1 Test particle simulation

245 Our test particle simulation (Tsai et al., 2022, 2023) is designed to compute the
 246 expected energy distribution of the electron precipitation flux ratio given realistic wave
 247 parameters. In order to obtain enough statistics – especially at higher energies where
 248 it is less likely for electrons to be scattered into the loss cone – we use a large number
 249 of particles for all test particle simulations in this study with $N = 5 \times 10^6$. For this
 250 to run in a reasonable amount of time, we parallelize the code and implement it in Ju-
 251 lia 1.9.3 (Bezanson et al., 2017) using the differential equations package (Rackauckas &
 252 Nie, 2017). The Hamiltonian formulation for wave-particle resonant interactions (Albert
 253 et al., 2013; Vainchtein et al., 2018) incorporates nonlinear effects such as phase bunch-

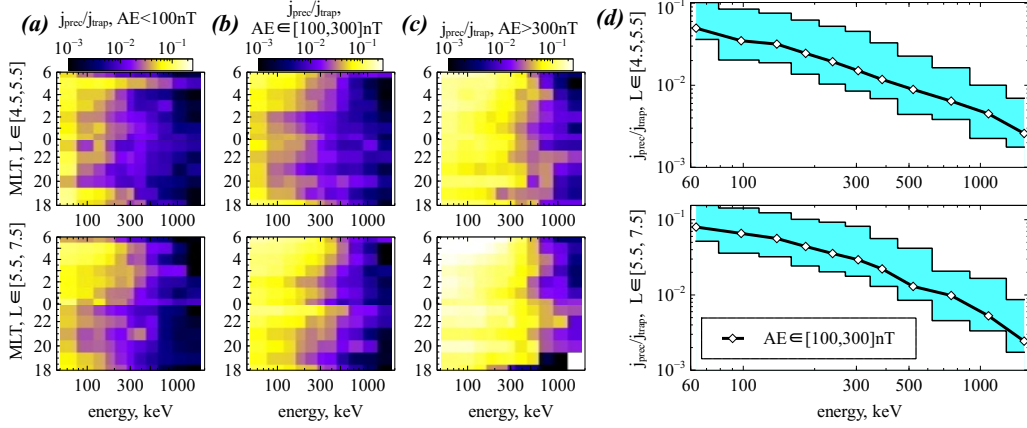


Figure 2. Plots (a-c) show the statistical distributions of precipitating-to-trapped electron spectra in (MLT, energy) space for several levels of geomagnetic activity. Plots (d) show energy profiles of precipitating-to-trapped fluxes for three geomagnetic activity levels in the nightside MLT $\in [18, 4]$. The shaded blue range regions represent the upper ($AE > 300$ nT) and lower ($AE < 100$ nT) bounds of geomagnetic activity levels while the central black curve depicts $AE \in [100, 300]$ nT.

254 ing, phase trapping, and anomalous trapping (Demekhov et al., 2006; Bortnik et al., 2008;
 255 Katoh et al., 2008; Omura et al., 2007; Kitahara & Katoh, 2019; Albert et al., 2021). The
 256 simulation uses monochromatic waves, which is generally valid for describing diffusive
 257 scattering in a background dipolar magnetic field due to its strong magnetic field gra-
 258 dient (Albert, 2001, 2010; Shklyar, 2021). Critically, the wave field is modified by the
 259 function $B_w(\lambda, L, MLT, Kp)$ which describes the wave amplitude variation along mag-
 260 netic field lines using an empirical chorus wave model built using 14 years of Cluster and
 261 Van Allen Probe statistics. The wave model is dependent on latitude, geographic loca-
 262 tion, and geomagnetic activity (see model and coefficients in Agapitov et al., 2018), which
 263 is necessary for realistic modeling of energetic electron losses. Further details of the test
 264 particle simulation implementation can be found in Tsai et al. (2022, 2023).

265 In this study, we have further augmented the test particle simulation to explore the
 266 latitudinal dependence of wave frequency and obliquity so that wave frequency $\omega(\lambda, \theta)$
 267 is a function of both latitude and wave normal angle. Changing into dimensionless vari-
 268 ables allows us to provide a mean normalized wave frequency $\omega_m(\lambda) = \omega(\lambda)/\Omega_{ce,eq}$ and
 269 mean wave normal angle $\theta(\lambda)$ both as functions of magnetic latitude λ (as described in
 270 Section 3.3). With dimensionless variables, the normalized plasma frequency is defined
 271 as $\Omega_{pe} = \omega_{pe,eq}/\Omega_{ce,eq}$.

272 3.2 Quasi-linear diffusion code

273 To instill further confidence in test particle simulation results, we calculate the quasi-
 274 linear diffusion coefficients using the Full Diffusion Code (Ni et al., 2008, 2011; Shprits
 275 & Ni, 2009; Ma et al., 2018) and model the precipitating electron flux using the Fokker-
 276 Planck diffusion code (Ma et al., 2012, 2015). This quasi-linear diffusion code physically
 277 differs from the test particle simulations primarily in the fact that it prescribes Gaus-
 278 sian distributions for the wave frequency (Glauert & Horne, 2005):

$$\hat{B}^2(\omega) \sim \exp\left[-\frac{(\omega - \omega_m(\lambda))^2}{\delta\omega^2}\right]$$

279 and the wave normal angle:

$$g(\theta) \sim \exp \left[-\frac{(\tan \theta - \tan \theta_m(\lambda))^2}{(\tan \delta\theta)^2} \right]$$

280 where mean values ω_m and θ_m with bandwidths $\delta\omega$ and $\delta\theta$ represent wave frequency and
 281 normal angle, respectively. These distributions are provided relative to mean values, $\omega_m(\lambda)$
 282 and $\theta_m(\lambda)$, which are given as functions of magnetic latitude λ and discussed in the next
 283 section (see details in Artemyev et al., 2013; Agapitov et al., 2018; Aryan et al., 2020).

284 We use the bounce-averaged Fokker-Planck equation to model the electron precip-
 285 itation rate (Lyons et al., 1972; Glauert & Horne, 2005):

$$\frac{\partial f}{\partial t} = \frac{1}{\tau_b(\alpha_{eq}) \sin 2\alpha_{eq}} \frac{\partial}{\partial \alpha_{eq}} \left(\tau_b(\alpha_{eq}) \sin 2\alpha_{eq} \left(\langle D_{\alpha\alpha} \rangle \frac{\partial f}{\partial \alpha_{eq}} \right) \right) - \frac{f}{\tau_{loss}} \quad (1)$$

286 where α_{eq} is the equatorial pitch angle, $\tau_b \approx 1.38 - 0.32 (\sin \alpha_{eq} + \sin^2 \alpha_{eq})$ (see Orlova
 287 & Shprits, 2011), $\langle D_{\alpha\alpha} \rangle$ is the bounce-averaged diffusion rate, and $\tau_{loss}(t)$ is the bounce
 288 loss time (and is set to be a quarter of the bounce period inside the local loss-cone and
 289 infinity outside the loss cone). We use the quasi-linear diffusion code to numerically solve
 290 Eq. (1), with diffusion rates derived from $\hat{B}^2(\omega)$ and $g(\theta)$ distributions (see Ni et al.,
 291 2008, 2011; Ma et al., 2015, 2018). Zero-gradient boundary conditions in pitch angle are
 292 set to simulate the loss cone filling of electrons due to wave scattering (Ma et al., 2022).

293 3.3 Frequency and Obliquity Models

294 In both simulations, we use the following two models to compare the effects of whistler
 295 wave frequency (normalized to the equatorial gyrofrequency) $\omega_m = \omega/\Omega_{ce,eq}$:

296 **Model 1:** normalized wave frequency held constant at $\omega_m = 0.35$, the typical frequency
 297 of whistler mode chorus waves near the equator (Agapitov et al., 2018).

298 **Model 2:** function $\omega(\lambda)$ linearly decreasing from $0.41\Omega_{ce,eq}$ at the equator until reach-
 299 ing a constant $0.16\Omega_{ce,eq}$ for $\lambda \geq 20^\circ$. This model is based on statistics of off-
 300 equatorial parallel and oblique lower-band chorus waves from the Van Allen Probes
 301 (Agapitov et al., 2018).

302 We use the following four models to describe the mean wave normal angle (WNA)
 303 θ_m . A scaling factor $\Theta(\lambda) = \lambda/(15^\circ + \lambda)$ is adopted to modify the WNA increase from
 304 0 at the equator to $\Theta(45^\circ) = 0.75$ at 45° latitude in WNA1 and WNA2.

305 **FAW:** a field-aligned wave model (with $\theta = 0^\circ$ in test particle simulations and $\theta_m =$
 306 0° , $\delta\theta = 30^\circ$ or $\delta\theta = 5^\circ$ in the quasi-linear diffusion code) that describes the
 307 most intense population of waves (Li, Santolik, et al., 2016; Agapitov et al., 2013)
 308 as they remain field-aligned off equator due to wave ducting by small-scale den-
 309 sity structures (Hanzelka & Santolik, 2019; Y. Shen et al., 2021; Ke et al., 2021;
 310 Hosseini et al., 2021).

311 **WNA1:** a moderately oblique WNA model with $\theta_1(\lambda) = \theta_G(\lambda) \cdot \Theta(\lambda)$, where $\theta_G =$
 312 $\arccos(2\omega/\Omega_{ce})$ is the Gendrin angle (Gendrin, 1961). This model describes field-
 313 aligned waves that are generated at the equator, but become mildly oblique as they
 314 propagate through the inhomogeneous plasma (e.g. Breuillard et al., 2012; L. Chen
 315 et al., 2013; Ke et al., 2017).

316 **WNA2:** a very oblique WNA model with $\theta_2(\lambda) = \theta_r(\lambda) \cdot \Theta(\lambda)$, where $\theta_r = \arccos(\omega/\Omega_{ce})$
 317 is the resonance cone angle. This describes field-aligned waves that are generated
 318 at the equator, but become very oblique as they propagate through the inhom-
 319 ogeneous plasma in the case of suppressed Landau damping (see discussion in Arte-
 320 myev & Mourenas, 2020).

321 **WNA3:** an extremely oblique WNA model with $\theta_3(\lambda) = \theta_r(\lambda) - 2^\circ$. This model de-
 322 scribes very oblique waves that are generated in the equatorial source region in
 323 the presence of field-aligned electron streams suppressing Landau damping (Mourenas
 324 et al., 2015; Li, Mourenas, et al., 2016; R. Chen et al., 2019; Kong et al., 2021).

325 The quasi-linear simulations also require a bandwidth parameter which sets the width
 326 of the wave frequency and normal angle Gaussian distributions, defined in Section 3.2.
 327 Frequency bandwidth $\delta\omega$ is set to 0.125, and the lower and upper cutoff frequencies are
 328 set to be $\omega_m - 2\delta\omega$ and 0.5, respectively. Wave normal angle bandwidth is set to either
 329 $\delta\theta = 5^\circ$ or $\delta\theta = 30^\circ$ for FAW, and $\delta\theta = 10^\circ$ for the other models; if $\theta_r(\lambda) - \theta_m(\lambda) <$
 330 20° , we set $\delta\theta = (\theta_r(\lambda) - \theta_m(\lambda))/2$. The lower (θ_{LC}) and upper (θ_{UC}) cutoff wave nor-
 331 mal angles are set as $\tan \theta_{LC} = \max(0, \tan \theta_m - 2 \tan \delta\theta)$ and $\tan \theta_{UC} = \min(\tan 89.9^\circ, \tan \theta_m +$
 332 $2 \tan \delta\theta)$, respectively.

333 Finally, the magnetic wave power distribution $B_w^2(\lambda)$ is taken from an empirical
 334 statistical model (Agapitov et al., 2018) at 23 MLT and $L = 6$ for $Kp = 3$. Note that
 335 we use $Kp = 3$ as a reasonable estimate of average geomagnetic activity level for ELFIN
 336 observations of electron precipitation driven by resonance with whistler-mode waves (see
 337 Tsai et al., 2023, for further discussion). For quiet conditions $Kp \leq 2$, the wave inten-
 338 sity provides insufficient levels of precipitating electron fluxes, which is generally corrob-
 339 orated by the extremely low levels (i.e. near background) of precipitating fluxes ELFIN
 340 observes during quiet periods. During disturbed storm times ($Kp > 4$), the precipitat-
 341 ing and locally trapped fluxes are occasionally too large and approach saturation of ELFIN's
 342 EPDE instrument (see details in X.-J. Zhang et al., 2022). Both types of ELFIN obser-
 343 vations (either background-level precipitation or nearly-saturated measurements) are ex-
 344 cluded from the statistical analysis.

345 4 Data-model comparison

346 In this section, the precipitating-to-trapped electron flux ratio j_{prec}/j_{trap} , calcu-
 347 lated through test particle simulations (TPS) or Quasi-Linear Diffusion Code (QLDC),
 348 are compared with j_{prec}/j_{trap} as measured by ELFIN. This allows us to assess the dif-
 349 ferent roles potentially played by plasma density, wave obliquity, and wave frequency based
 350 on precipitating flux ratio variation with energy.

351 For proper comparison, the simulated j_{prec}/j_{trap} flux ratio is normalized to the ob-
 352 served j_{prec}/j_{trap} flux ratio at ELFIN's second energy bin (~ 97 keV), thereby remov-
 353 ing wave amplitude variability such that the spectral slope can be compared for across
 354 various scenarios. This is valid because the $\sim 30 - 100$ keV precipitating-to-trapped
 355 electron flux ratio correlates well with the equatorial wave amplitude (Li et al., 2013; Ni
 356 et al., 2014). In addition, spurious variations in j_{prec}/j_{trap} modeled using our test par-
 357 ticle simulations tend to become larger below 97 keV, despite the large number of par-
 358 ticle runs per energy bin. These oscillations are absent from results of the quasi-linear
 359 diffusion code, which correlate well with test particle simulation results above 97 keV
 360 after normalization.

361 4.1 Role of plasma density

362 Figure 3 shows a comparison between the precipitating-to-trapped electron flux ratio
 363 j_{prec}/j_{trap} measured by ELFIN at $L > 5$ and 18-4 MLT (black) with j_{prec}/j_{trap} ob-
 364 tained from TPS (solid red) and QLDC (dashed red) with parallel (FAW model) lower-
 365 band chorus waves (adopting $\theta = 0^\circ$ in test particle simulations, $\delta\theta = 30^\circ$ in the quasi-
 366 linear diffusion code), using wave frequency Model 1 of constant frequency ($\omega_m = 0.35$)
 367 chorus waves and a typical plasma frequency to gyrofrequency ratio $\Omega_{pe} = 6.5$ at $L =$
 368 6.5 and 23 MLT (Sheeley et al., 2001). In this plot (and remaining Figures 3-7), the gray
 369 shaded regions of ELFIN data denote the boundaries of quiet (AE < 100 nT) and ac-

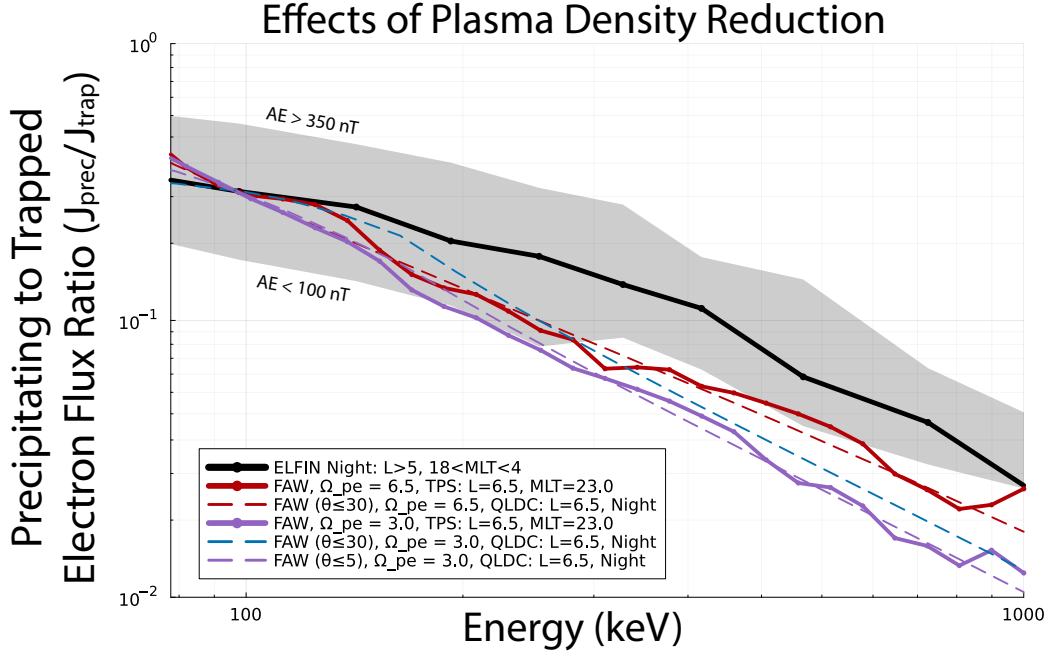


Figure 3. ELFIN-measured precipitating-to-trapped electron flux ratio at $L > 5$ on the night-side (18 – 4 MLT) as a function of energy (black curve). The corresponding j_{prec}/j_{trap} flux ratio obtained from test particle simulations is shown for parallel (FAW model, $\theta = 0^\circ$) lower-band chorus waves, using frequency Model 1 ($\omega_m = constant$) and a typical $\Omega_{pe} = 6.5$ at $L = 6.5$ and 23 MLT (solid red). Results from the quasi-linear diffusion code using the same parameters is shown in dashed red. Similarly, the cases of reduced density $\Omega_{pe} = 3$ modeled with test particle simulation (solid purple), quasi-linear diffusion code using narrow-band field aligned waves ($\delta\theta = 5^\circ$, dashed purple), and more quasi-linear field aligned waves ($\delta\theta = 30^\circ$, dashed blue), are shown. All simulation results are normalized to observations at 97 keV.

370 tive ($AE > 350$ nT) times. The normalized ratios j_{prec}/j_{trap} obtained from TPS and
 371 QLDC are quite similar (compare solid with dashed lines of the same color), validating
 372 the reliability of the quasi-linear approach (Kennel & Engelmann, 1966; Lyons et al., 1972;
 373 Albert, 2005; Glauert & Horne, 2005; Mourenas et al., 2012; Mourenas, Artemyev, Agapi-
 374 tov, & Krasnoselskikh, 2014), especially in the case of field aligned waves, as demonstrated
 375 in previous studies (Tao et al., 2012; Mourenas, Artemyev, et al., 2022; Gan et al., 2022;
 376 Z. An et al., 2022). However, despite their normalization to the measured j_{prec}/j_{trap} at
 377 97 keV, these similar ratios of j_{prec}/j_{trap} (red curves) obtained from test particle sim-
 378 ulations and from the quasi-linear diffusion code become $\sim 1.5 - 2$ times smaller than
 379 the measured j_{prec}/j_{trap} at 200–1000 keV (black), corresponding to a deficiency of pitch-
 380 angle diffusion occurring at higher energies. For reference, this baseline case (red) rep-
 381 represents the same discrepancy on the nightside as first described in Tsai et al. (2023).

382 A reduced plasma density should lower the latitude of first-order cyclotron reso-
 383 nance with chorus waves for electrons near the loss-cone (Mourenas et al., 2012). Since
 384 chorus wave power B_w^2 is higher at lower latitudes (Agapitov et al., 2018), a reduced den-
 385 sity is therefore expected to yield higher electron pitch-angle diffusion rate $D_{\alpha\alpha} \propto B_w^2$
 386 near the loss-cone leading to higher precipitation rates and fluxes at all energies. How-
 387 ever, adopting a reduced plasma density ($\Omega_{pe} = 3$) in test particle simulations (pur-
 388 ple line in Fig. 3) and normalizing the flux ratio at 97 keV leads to an even larger dis-
 389 crepancy across the 300 – 1000 keV range with a $\sim 2 - 3$ times smaller j_{prec}/j_{trap} ra-
 390 tio than ELFIN statistics show. We therefore interpret this density effect as more im-
 391 portant at lower energies (~ 100 keV) compared to higher energies (> 300 keV) due
 392 to $B_w^2(\lambda)$ increasing, in our model and in observations, more steeply towards lower lat-
 393 itudes at $\lambda \lesssim 25^\circ$ (where resonance with ~ 100 keV electrons occurs) than at $\lambda > 25^\circ$
 394 (where resonance with ~ 1 MeV electrons occurs) during disturbed periods at 21-3 MLT
 395 (Agapitov et al., 2018). Therefore, the wave power $B_w^2(\lambda)$ seen by electrons near the loss-
 396 cone increases only marginally at higher energies for both $\theta = 0^\circ$ in test-particle sim-
 397 ulations and $\theta < 5^\circ$ or $\theta < 30^\circ$ in QLDC simulations (solid/dashed purple and dashed
 398 blue lines). This then reduces the normalized pitch-angle diffusion rate $D_{\alpha\alpha}$ near the loss-
 399 cone and the normalized j_{prec}/j_{trap} flux ratio, which varies roughly like $\approx \sqrt{D_{\alpha\alpha}}$ (Kennel
 400 & Petschek, 1966; Li et al., 2013; Mourenas, Zhang, et al., 2022; Mourenas et al., 2023).

401 Adopting a more realistic spread of WNAs for quasi-field aligned waves ($\delta\theta = 30^\circ$,
 402 blue dashed line) in the quasi-linear diffusion code leads to the effects of additional, higher-
 403 order cyclotron resonances to become more significant (Artemyev et al., 2016), which is
 404 clearly shown as the difference between the blue and purple dashed lines in Figure 3. Due
 405 to moderate obliqueness, this effect is most prominent in the lower energies – resonat-
 406 ing with waves around the equator – extending now to about 180 keV. However, it is not
 407 enough to reproduce ELFIN observations up to 1 MeV, because the relative scattering
 408 efficiency decreases with the purple curve at higher energies, causing the blue curve to
 409 underestimate ELFIN statistics beyond > 250 keV. Despite the fact that, in observa-
 410 tions, the plasma frequency to gyrofrequency ratio Ω_{pe} does decrease at 18-4 MLT dur-
 411 ing disturbed periods (O’Brien & Moldwin, 2003), often down to $\Omega_{pe} \approx 3 - 4$ at $L \sim$
 412 6 when $AE > 150$ nT (Agapitov et al., 2019), results in Figure 3 show that plasma den-
 413 sity reduction alone cannot account for a relative increase of electron scattering at higher
 414 energies.

415 4.2 Role of wave frequency

416 As noted earlier, statistical observations of lower-band chorus waves show that their
 417 normalized frequency is not constant as a function of latitude (as assumed in frequency
 418 Model 1), but rather, decreasing due to preferential Landau damping affecting higher
 419 frequencies at higher latitudes (Agapitov et al., 2018; Bunch et al., 2013; L. Chen et al.,
 420 2013), as reflected by frequency Model 2. Figure 4a shows that the j_{prec}/j_{trap} ratios ob-
 421 tained for wave normal angle model FAW from test particle simulations (solid curves)

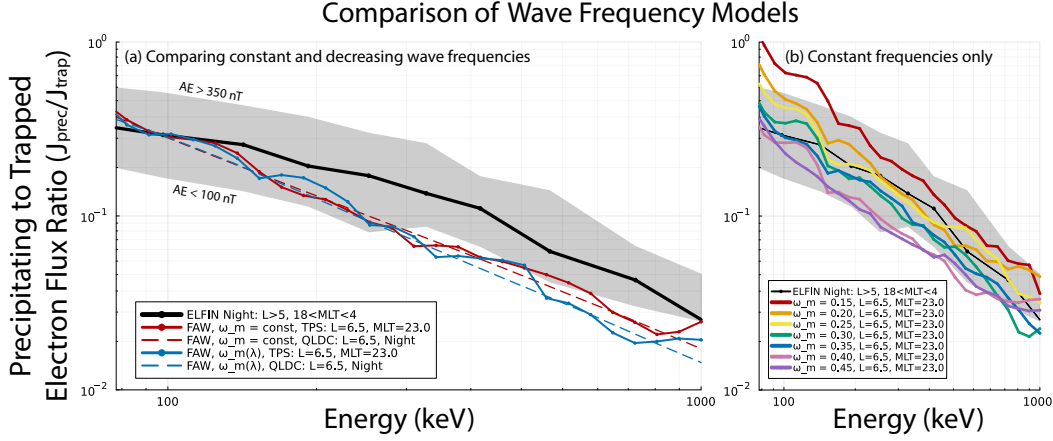


Figure 4. To compare the effects of two frequency models, precipitating-to-trapped electron flux ratio j_{prec}/j_{trap} plotted for ELFIN statistics on the nightside (black) is shown in comparison with j_{prec}/j_{trap} ratios obtained from test particle simulations (TPS, solid lines) and quasi-linear diffusion code (QLDC, dashed lines). In (a), Frequency Model 2 (frequency decreasing toward higher latitudes, blue) produces slightly higher precipitation rates at 100 keV relative to 1 MeV as compared to a constant $\omega_m = 0.35$ (red). Plot (b) shows results from a variety of normalized wave frequency values that do not vary as a function of magnetic latitude, demonstrating that absolute frequency has little effect on the slope of the precipitation energy spectra.

and from the quasi-linear diffusion code (dashed curves) are both slightly decreased at $E = 200 - 1000$ keV when wave frequency Model 2 is used (blue curves), rather than when using Model 1. This is because a reduction of wave frequency alone, when adopting a fixed plasma density $\Omega_{pe} = 6.5$ at $L = 6.5$, has essentially the same effect as decreasing plasma density in Section 4.1 – albeit weaker in magnitude – by allowing first-order cyclotron resonance for electrons near the loss-cone to occur at lower latitudes (Mourenas et al., 2012). In turn, this preferentially increases precipitation rates at low energies $E \lesssim 100$ keV, the typical resonance energies at low-latitude plasma conditions.

Figure 4b shows that decreasing the wave frequency by a fixed amount significantly increases electron precipitation rates by lowering the latitude of resonance with chorus waves. But at the same time, it leads to only a slight increase of the slope of the energy spectrum once normalized to ELFIN statistics, because the amplitude of resonant waves is slightly more increased for 100 keV electrons than for 1 MeV electrons. For a large plasma density, $\Omega_{pe} = 6.5$, this effect on the normalized j_{prec}/j_{trap} remains weak, and both wave frequency Model 1 and 2 end up giving very similar results. Therefore, the effects of frequency variation with latitude alone cannot account for the spectral shape of the precipitation ratio in ELFIN’s nightside observations.

4.3 Role of wave obliquity

Figure 5a compares ELFIN-observed precipitating-to-trapped flux ratio on the nightside (black) with that of simulations in order to explore the effects of a variety of wave-normal angle distributions paired with constant wave frequency (Model 1) and baseline plasma density (Sheeley et al., 2001). Results from test particle simulations (solid curves) and from the quasi-linear diffusion code (dashed curves) are displayed for four different models of wave normal angle: FAW (red), WNA1 (green), WNA2 (blue), and WNA3 (purple), corresponding to a progressively larger amount of wave power in oblique waves closer to the resonance cone angle (see Section 3.3). Despite the large number of particles ($N =$

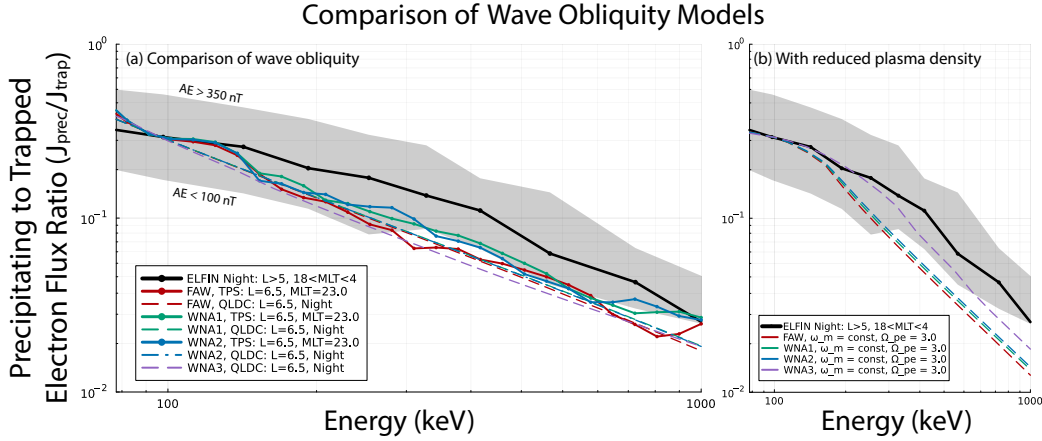


Figure 5. ELFIN-observed j_{prec}/j_{trap} flux ratio at $L > 5$ on the nightside (18 – 4 MLT) as a function of electron energy (black). The corresponding ratios j_{prec}/j_{trap} obtained from test particle simulations (TPS, solid curves) and from the quasi-linear diffusion code (QLDC, dashed curves) are displayed for lower-band chorus waves in (a), using frequency Model 1 of constant frequency, and parameterized by four wave normal angle models: FAW (red), WNA1 (green), WNA2 (blue), and WNA3 (purple), with a normalization to observations at 97 keV, adopting a typical $\Omega_{pe} = 6.5$ at $L = 6.5$ and 23 MLT. (b) shows QLDC results for the same four wave normal angle models but for a reduced plasma density of $\Omega_{pe} = 3.0$.

448 5×10^6), unnatural oscillations in the test particle simulations make it difficult to quan-
 449 tify the exact contribution differences among the FAW, WNA1, and WNA2 models. Es-
 450 pecially because the test particle simulation only includes first-order oblique wave inter-
 451 actions, it is reasonable to conclude that including wave obliquity in the TPS does not
 452 significantly alter precipitation efficiency. However, results from the quasi-linear diffu-
 453 sion code generally agree with test particle simulation results, indicating the reliability
 454 of the quasi-linear approach (described, e.g., by Kennel & Engelmann, 1966; Lyons et
 455 al., 1972; Albert, 2005; Glauert & Horne, 2005; Mourenas et al., 2012; Mourenas, Arte-
 456 myev, Agapitov, & Krasnoselskikh, 2014). Our quasi-linear simulations show that wave
 457 obliquity is ineffective at increasing high energy electron precipitation compared to low
 458 energy electron precipitation (in the case of $\Omega_{pe} = 6.5$). Note that WNA1 and WNA2
 459 models correspond to wave-normal angle distributions that extend up to three-quarters
 460 of the Gendrin angle and resonance cone angle, respectively, at $\lambda > 45^\circ$, while the WNA3
 461 model corresponds to highly oblique waves, at about 2° from the resonance cone angle.
 462 Yet the results are nearly identical (dashed blue, dashed green, and dashed purple curves).

463 Oblique chorus waves can resonate with electrons via high-order cyclotron resonances
 464 ($n \geq 1$ or $n \leq -2$, e.g., Shklyar & Matsumoto, 2009; Mourenas et al., 2012; Artemyev
 465 et al., 2013, 2016; Albert, 2017), which can significantly increase diffusion rates at high
 466 energy (Lorentzen et al., 2001; Gan et al., 2023). However, diffusion rates near the loss
 467 cone due to higher-order cyclotron resonances rapidly decrease in magnitude as $|n|$ in-
 468 creases, especially from $|n| = 1$ to $|n| = 2$ (Shprits & Ni, 2009), although this reduc-
 469 tion is weaker for highly oblique waves (Artemyev et al., 2016). To increase the ratio of
 470 1 MeV to 100 keV pitch-angle diffusion rates near the loss cone, therefore, the waves must
 471 be sufficiently oblique and/or plasma density and wave frequency should be sufficiently
 472 low to enable only first-order resonance at ~ 100 keV, but higher-order resonances at
 473 1 MeV (Artemyev et al., 2016; Mourenas & Ripoll, 2012; Shprits & Ni, 2009; Gan et al.,
 474 2023). Figure 5b indeed shows that when plasma density is reduced to $\Omega_{pe} = 3$ (or equiv-

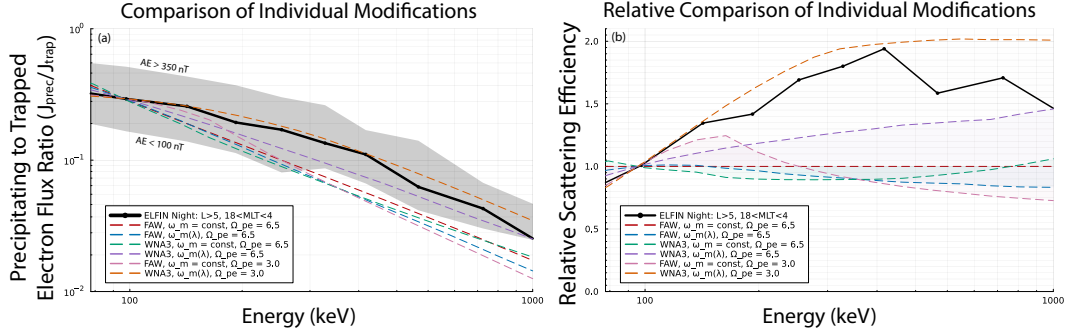


Figure 6. ELFIN-observed nightside ($18 - 4$ MLT) j_{prec}/j_{trap} electron flux ratio shown as a function of energy (black). (a) shows j_{prec}/j_{trap} flux ratios obtained from quasi-linear diffusion code (QLDC) for parallel (FAW) lower-band chorus waves (red), very oblique waves using wave normal angle model WNA3 (green), waves with a realistic wave frequency distribution (blue), WNA3 with a realistic wave frequency distribution (purple), FAW with reduced density (pink), and everything combined (orange). (b) shows the same flux ratios all normalized to the base case with no modifications (red) demonstrating which energy range each modification is most effective at on a linear scale. This shows that each effect examined alone cannot reproduce results from ELFIN individually.

475 alently, when wave frequency decreases with latitude, see Section 4.4), electron precip-
 476 itation is greatly increased at 1 MeV relative to 100 keV as wave obliquity increases, espe-
 477 cially in the case of highly oblique waves (WNA3). These results therefore suggest that
 478 wave obliquity, alone, has a near-negligible effect on the high-energy to low-energy elec-
 479 tron loss ratio; however, when combined with a density reduction, it can significantly en-
 480 hance energetic electron losses.

481 4.4 Combined results

482 Figure 6a shows comparisons between the precipitating-to-trapped electron flux ra-
 483 tio j_{prec}/j_{trap} measured by ELFIN at $L > 5$ on the nightside (black), overlaid with j_{prec}/j_{trap}
 484 obtained from the quasi-linear diffusion code for the three modifications in question –
 485 reduced plasma density $\Omega_{pe} = 3$, Frequency Model 2, and WNA3 – alone or in com-
 486 bination. As surmised in previous sections, each individual modification fails to agree
 487 with the observed spectrum. With wave frequency Model 2 (blue) and WNA3 (green)
 488 underestimating across entire energy range (i.e., increasing precipitation at 100 keV) and
 489 reduced density (pink) providing a relative efficiency bump of j_{prec}/j_{trap} only at $E <$
 490 200 keV. Interestingly, however, ELFIN’s statistical observations are only slightly un-
 491 derestimated when combining WNA3 and Frequency Model 2 (purple), and best matched
 492 when all three modifications are combined (orange). Figure 6b shows the relative dif-
 493 ference produced by each modification compared to the baseline red curve. We see that
 494 these effects synergistically enhance j_{prec}/j_{trap} flux ratios at higher energies. For exam-
 495 ple, Model 2 (blue) becomes relatively less effective at higher energy, while WNA3 (green)
 496 immediately loses effectiveness, but catches back up closer to 1 MeV. However, when com-
 497 bined (purple), the relative precipitation is drastically enhanced in the entire 200–1000
 498 keV range, leading to far better agreement with observations. Further combining WNA3
 499 and Frequency Model 2 with a reduced plasma density (orange) significantly enhances
 500 precipitation past levels observed by ELFIN (black). This is likely due to two phenom-
 501 ena: first, the combined effects of a reduced plasma density and a decreasing wave fre-
 502 quency decrease the latitude at which cyclotron resonance with quasi-parallel waves oc-

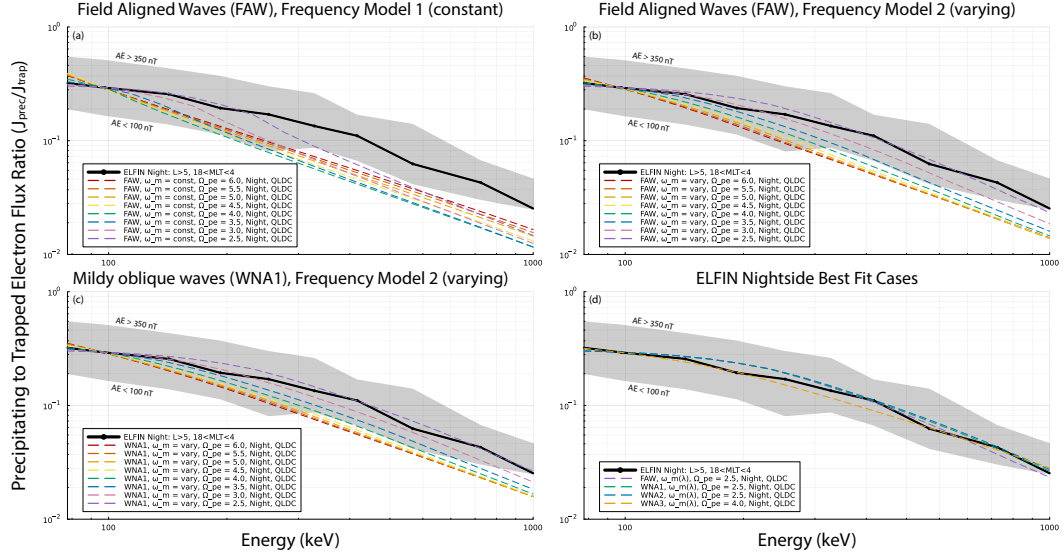


Figure 7. The comparison between observed electron precipitation ratios and simulation results using different wave frequency models, Ω_{pe} ratios, and wave normal angle models. In each plot, the black line denotes statistical averages of j_{prec}/j_{trap} flux ratios for nightside ELFEN observations with $L > 5$. Plots (a-c) show QLDC results with various modifications parameterized by Ω_{pe} : (a) shows field aligned waves with Frequency Model 1; (b) shows field aligned waves with Frequency Model 2; and (c) shows WNA1 combined with Frequency Model 2. (d) shows that all three effects – $\omega_{pe} \in [2.5, 4]$, combined with Frequency Model 2 and some level of wave obliquity – are necessary for recreating ELFEN nightside statistics.

503 occurs far more significantly than each effect alone (Mourenas et al., 2012), leading to a
 504 larger increase of resonant wave power for higher energy electrons that best match ELFEN’s
 505 observed precipitation spectra; second, the supplementary higher-order cyclotron reso-
 506 nances contributing at ~ 1 MeV, but not at ~ 150 keV, are of lower order ($|n| = 2$)
 507 than for higher density or frequency, allowing for a more dramatic increase of the 1 MeV
 508 to 150 keV pitch-angle diffusion rate ratio (Artemyev et al., 2016; Mourenas & Ripoll,
 509 2012; Shprits & Ni, 2009; Gan et al., 2023).

510 Figure 7 summarizes the findings from each wave parameter combination through-
 511 out a range of reduced equatorial plasma densities for a better understanding of the inter-
 512 play between the three effects considered. Figure 7a shows that only below a certain
 513 threshold of $\Omega_{pe} \lesssim 4$ does the interaction of higher-order resonances start to increase
 514 precipitation at higher energies. Using the total electron density with $\Omega_{pe} = 2.5$, this
 515 effect becomes very pronounced above 100 keV and up to 300 keV, whereas above that
 516 energy this effect alone is still incapable of matching observations, as discussed in Sec-
 517 tion 4.1. The effect of plasma density combined with wave frequency becomes significantly
 518 more pronounced throughout the whole energy range when $\Omega_{pe} \lesssim 4$, as shown in Fig-
 519 ure 7b, and matches very well with ELFEN’s nightside observations when a more extreme
 520 $\Omega_{pe} = 2.5$ is used. Adding mild wave obliquity (Figure 7c) results in the best match
 521 with ELFEN statistics, demonstrating that all three effects combined are necessary.

522 Figure 7d shows the best fit scenarios for forward-modeling ELFEN-observed precipitating-
 523 to-trapped flux ratios, which all require the varying frequency model in addition to re-
 524 duced plasma density to various degrees. Here, we show that it is possible to obtain de-
 525 cent agreement without the need for wave obliquity by significantly reducing Ω_{pe} to 2.5

(purple). By adding moderately oblique waves (green and blue), more ~ 1 MeV electrons are precipitated, doing a marginally better job of matching observations. Using extremely oblique waves (WNA3) – which describes a population of very oblique waves generated around the equator when the Landau damping is largely reduced by field-aligned electron streams (Mourenas et al., 2015; Li, Mourenas, et al., 2016) – requires increasing plasma density $\Omega_{pe} = 4$ in order to avoid significant overestimation. Therefore, ELFIN observations of nightside electron precipitation spectra (from 50–1000 keV) can be described either under the assumption of a significant plasma density reduction or a more moderate plasma density reduction coupled with a strongly oblique wave population. This required plasma density ($\omega_{pe} \in [2.5, 4]$) is fully consistent with the average measured ω_{pe} levels at 18-4 MLT and $L = 5-6.5$ in Van Allen Probes statistics during disturbed periods with $AE \in [150, 600]$ nT (Agapitov et al., 2019). These conditions indicate the importance of plasma injections and/or enhanced convection periods and how they cause enhanced nightside electron losses. Such Earthward plasma transport (convection and injections), especially during increased geomagnetic activity, justifies our choice of the cold plasma density reduction (Agapitov et al., 2019). These injections are also associated with electron field-aligned streams caused by the electrostatic turbulence around injection regions or the ionosphere outflow of secondary electrons in response to the enhanced precipitation of plasma sheet electron fluxes (see Khazanov et al., 2014, 2018; Artemyev & Mourenas, 2020; Artemyev et al., 2020, and references therein).

5 Discussion and Conclusions

Today’s radiation belt simulations primarily rely on EMIC-driven electron precipitation to explain relativistic electron losses (see, e.g., Ma et al., 2015; Drozdov et al., 2017, and references therein), in addition to dropouts related to magnetopause shadowing loss (e.g., see Shprits et al., 2006; Turner et al., 2014; Boynton et al., 2016, 2017; Olfier et al., 2018; Xiang et al., 2018). Analysis presented here shows that the inclusion of realistic whistler-mode wave properties can meaningfully enhance relativistic electron scattering rates, thereby reducing the relative importance of EMIC waves on the nightside, at least for electrons below 1 MeV. While it has been known for a long time that whistler-mode waves can accelerate electrons to relativistic energies (Thorne et al., 2013; Li et al., 2014; Mourenas, Artemyev, Agapitov, Krasnoselskikh, & Li, 2014; Omura et al., 2015; Hsieh & Omura, 2017; Allison & Shprits, 2020), contribution of this wave mode to relativistic electron losses may be underestimated in modern-day simulations due to the lack of observations that can reliably quantify it. This has recently changed with the availability of ELFIN’s unique precipitation observations, which now allow us to quantify how well modeling – based on statistical averages of wave properties and plasma density – reflects the observed precipitation energy spectra of energetic electrons.

We previously showed that using only field-aligned, monochromatic whistler-mode waves with realistic wave amplitudes as a function of magnetic latitude was sufficient to approximate relativistic electron losses at the dawn, noon, and dusk sectors (Tsai et al., 2023). However, the modeled precipitating-to-trapped flux ratio significantly underestimated ELFIN-obtained statistics of precipitation energy spectra in the nightside MLT sector. Pertinent to ELFIN statistics, we specifically excluded all data exhibiting signatures of field-line curvature scattering, EMIC waves, and any signatures of noise or poor statistics. The resulting ELFIN statistics are 3 years of unambiguous whistler-mode wave-driven energetic electron precipitating-to-trapped flux ratios across a range of MLT, L -shells, and geomagnetic activity. At first, we used test particle simulations to examine various wave and plasma characteristics that may potentially cause this discrepancy. However, test particle simulations showed that, while some effects led to better agreement, the discrepancy was still large. However, by additionally utilizing a state-of-the-art quasi-linear diffusion code, we were able to quantify each key wave parameter – alone and in combination – relative to ELFIN observations, thereby determining the importance of

578 including empirically-obtained equatorial plasma frequency, wave-normal angle distri-
 579 butions, and wave frequency distributions. We found that, in addition to the prerequi-
 580 site, empirically-provided $B_w(\lambda)$ (Tsai et al., 2023), inclusion of all three modifications
 581 – realistic Ω_{pe} , $\omega_m(\lambda)$, and $\theta(\lambda)$ – were sufficient to recover the more intense nightside
 582 energetic precipitation observed by ELFIN. A reduced plasma density, indicative of geo-
 583 magnetically active times, results in relative enhancement of precipitation in the sub-
 584 relativistic regime (< 300 keV), while wave obliquity significantly enhances relativistic
 585 electron scattering > 500 keV. It seems that a decreasing wave frequency as a function
 586 of latitude helps balance the two out, leading to a smooth recovery of the 200–600 keV
 587 range, without severely overestimating either ends of the precipitation flux ratio spec-
 588 trum.

589 The equatorial confinement of whistler-mode waves is attributed to the increase
 590 of wave obliquity – or more precisely, the increase of statistical averages of wave normal
 591 angles – as expected from wave propagation away from their equatorial source (L. Chen
 592 et al., 2013; Breuillard et al., 2012; Agapitov et al., 2013) due to the associated severe
 593 damping by Landau resonance with suprathermal electrons (e.g., Bell et al., 2002; Bort-
 594 nik et al., 2007). This effect is substantially less important on the dayside as compared
 595 to the nightside, as evidenced by the significantly larger amplitudes of waves at higher
 596 latitudes on the dayside (Meredith et al., 2012). Reduced Landau damping is caused by
 597 a milder ambient dayside magnetic field gradient (due to magnetospheric compression)
 598 and a lower density of suprathermal electrons (Li, Thorne, Bortnik, et al., 2010; Walsh
 599 et al., 2020). As a result, waves on the dayside propagate in higher densities, are less oblique,
 600 and have a less pronounced decrease in wave frequencies, in direct opposition to what
 601 is observed on the nightside. This explains why an empirical model of $B_w(\lambda)$ and field
 602 aligned waves is sufficient for recovering dayside energetic electron precipitation (Tsai
 603 et al., 2023), while further indicating the importance of including realistic wave and back-
 604 ground plasma characteristics for such precipitation modeling on the nightside.

605 To conclude, these results highlight the importance of combining whistler-mode wave
 606 characteristics and background plasma for accurately modeling relativistic electron losses
 607 from the outer radiation belt. Specifically, we note that:

- 608 • The latitudinal distribution of wave amplitude alone cannot account for the in-
 609 tense nightside precipitation of ~ 0.1 – 1 MeV electrons scattered at mid-to-high
 610 latitudes relative to precipitation of ~ 100 keV electrons scattered near the equa-
 611 tor.
- 612 • Very oblique waves are important for scattering more energetic electrons – becom-
 613 ing more effective in the ~ 1 MeV range – but only in the presence of reduced
 614 plasma density or decreasing wave frequency.
- 615 • The decrease of wave frequency with latitude, caused by high-frequency wave damp-
 616 ing, is not very important on its own. However, together with a reduced plasma
 617 density (with or without oblique waves), it can lead to more precipitation of high
 618 energy electrons relative to ~ 100 keV electrons.
- 619 • Equatorial plasma density decrease during geomagnetically active conditions (char-
 620 acterized by enhanced whistler-mode wave intensity) improves the relative efficiency
 621 of resonant electron scattering toward the loss-cone at 100 keV compared to 1 MeV,
 622 but alone, it is in poor agreement with ELFIN statistics. However, when combined
 623 with increasing WNA and decreasing wave frequency as a function of latitude, this
 624 plasma density reduction becomes a catalyst, significantly boosting electron pre-
 625 cipitation rates across the energy range up to 1 MeV.

626 So, in order to best explain the increased precipitation observed by ELFIN on the night-
 627 side, modeled whistler-mode waves must have a realistic latitudinally-dependent wave
 628 frequency model (Model 2) coupled with a reduced plasma density ($\Omega_{pe} \in [2.5, 4]$) and
 629 an associated range of wave obliquity from quasi-field aligned ($\theta < 30^\circ$) to extremely

630 oblique (WNA3) waves. Any further investigation of these effects likely requires either
 631 detailed and comprehensive simulations using modern ray-tracing techniques (e.g., L. Chen
 632 et al., 2021, 2022; Hosseini et al., 2021; Hanzelka & Santolík, 2022; Kang et al., 2022;
 633 Kang & Bortnik, 2022) or a new generation of satellite missions equipped to make si-
 634 multaneous measurements of whistler-mode waves and precipitating/trapped electron
 635 populations.

636 Acknowledgments

637 We are grateful to NASA’s CubeSat Launch Initiative and Launch Services Program for
 638 ELFIN’s successful launch in the desired orbits. We acknowledge early support of ELFIN
 639 project by the AFOSR, under its University Nanosat Program, UNP-8 project, contract
 640 FA9453-12-D-0285, and by the California Space Grant program. Importantly, we acknowl-
 641 edge the critical contributions by numerous UCLA students who made the ELFIN mis-
 642 sion a success. A.V.A and X.-J.Z. acknowledge support from the NASA grants 80NSSC23K0089,
 643 80NSSC22K0522, 80NSSC23K0108, 80NSSC19K0844, 80NSSC23K0100 and NSF grant
 644 2329897. V. A. acknowledge support from NSF grants AGS-1242918, AGS-2019950, and
 645 AGS-2329897. Q.M. acknowledges the NASA grant 80NSSC20K0196 and NSF grant AGS-
 646 2225445. The work O.V.A. was supported by NASA grants 80NNSC19K0848, 80NSSC20K0697,
 647 80NSSC22K0433, 80NSSC22K0522, NASA’s Living with a Star (LWS) program (con-
 648 tract 80NSSC20K0218), and by NSF grant number 1914670.

649 Open Research

650 ELFIN data is available at <https://data.elfin.ucla.edu/> and online summary plots
 651 at <https://plots.elfin.ucla.edu/summary.php>.
 652 Data access and processing was done using SPEDAS V4.1, see Angelopoulos et al. (2019).
 653 Test-particle simulation code is found at <https://github.com/ethantsai/nlwhistlers>
 654 (Tsai, 2023).

655 References

- 656 Agapitov, O. V., Artemyev, A., Krasnoselskikh, V., Khotyaintsev, Y. V., Moure-
 657 nas, D., Breuillard, H., ... Rolland, G. (2013, June). Statistics of whistler
 658 mode waves in the outer radiation belt: Cluster STAFF-SA measurements. *J.*
 659 *Geophys. Res.*, *118*, 3407-3420. doi: 10.1002/jgra.50312
- 660 Agapitov, O. V., Krasnoselskikh, V., Mozer, F. S., Artemyev, A. V., & Volokitin,
 661 A. S. (2015, May). Generation of nonlinear electric field bursts in the outer
 662 radiation belt through the parametric decay of whistler waves. *Geophys. Res.*
 663 *Lett.*, *42*, 3715-3722. doi: 10.1002/2015GL064145
- 664 Agapitov, O. V., Mourenas, D., Artemyev, A., Hospodarsky, G., & Bonnell, J. W.
 665 (2019, June). Time Scales for Electron Quasi-linear Diffusion by Lower-Band
 666 Chorus Waves: The Effects of ω_{pe}/Ω_{ce} Dependence on Geomagnetic Activity.
 667 *Geophys. Res. Lett.*, *46*(12), 6178-6187. doi: 10.1029/2019GL083446
- 668 Agapitov, O. V., Mourenas, D., Artemyev, A. V., & Mozer, F. S. (2016). Exclusion
 669 principle for very oblique and parallel lower band chorus waves. *Geophys. Res.*
 670 *Lett.*, *43*(21), 11,112–11,120. Retrieved from [http://dx.doi.org/10.1002/](http://dx.doi.org/10.1002/2016GL071250)
 671 [2016GL071250](http://dx.doi.org/10.1002/2016GL071250) doi: 10.1002/2016GL071250
- 672 Agapitov, O. V., Mourenas, D., Artemyev, A. V., Mozer, F. S., Hospodarsky, G.,
 673 Bonnell, J., & Krasnoselskikh, V. (2018, January). Synthetic Empirical
 674 Chorus Wave Model From Combined Van Allen Probes and Cluster Statis-
 675 tics. *Journal of Geophysical Research (Space Physics)*, *123*(1), 297-314. doi:
 676 10.1002/2017JA024843
- 677 Albert, J. M. (2001, May). Comparison of pitch angle diffusion by turbulent and
 678 monochromatic whistler waves. *J. Geophys. Res.*, *106*, 8477-8482. doi: 10

- 679 .1029/2000JA000304
 680 Albert, J. M. (2005, March). Evaluation of quasi-linear diffusion coefficients for
 681 whistler mode waves in a plasma with arbitrary density ratio. *J. Geophys.*
 682 *Res.*, *110*, 3218. doi: 10.1029/2004JA010844
 683 Albert, J. M. (2010, March). Diffusion by one wave and by many waves. *J. Geo-*
 684 *phys. Res.*, *115*, 0. doi: 10.1029/2009JA014732
 685 Albert, J. M. (2017, May). Quasi-linear diffusion coefficients for highly oblique
 686 whistler mode waves. *J. Geophys. Res.*, *122*, 5339-5354. doi: 10.1002/
 687 2017JA024124
 688 Albert, J. M., Artemyev, A. V., Li, W., Gan, L., & Ma, Q. (2021). Models of
 689 resonant wave-particle interactions. *Journal of Geophysical Research: Space*
 690 *Physics*, *126*(6), e2021JA029216. doi: 10.1029/2021JA029216
 691 Albert, J. M., Tao, X., & Bortnik, J. (2013). Aspects of Nonlinear Wave-Particle In-
 692 teractions. In D. Summers, I. U. Mann, D. N. Baker, & M. Schulz (Eds.), *Dy-*
 693 *namics of the earth's radiation belts and inner magnetosphere*. doi: 10.1029/
 694 2012GM001324
 695 Allison, H. J., & Shprits, Y. Y. (2020, September). Local heating of radiation belt
 696 electrons to ultra-relativistic energies. *Nature Communications*, *11*, 4533. doi:
 697 10.1038/s41467-020-18053-z
 698 Allison, H. J., Shprits, Y. Y., Zhelavskaya, I. S., Wang, D., & Smirnov, A. G. (2021,
 699 January). Gyroresonant wave-particle interactions with chorus waves during
 700 extreme depletions of plasma density in the Van Allen radiation belts. *Science*
 701 *Advances*, *7*(5), eabc0380. doi: 10.1126/sciadv.abc0380
 702 An, X., Artemyev, A., Angelopoulos, V., Zhang, X., Mourenas, D., & Bortnik, J.
 703 (2022, September). Nonresonant Scattering of Relativistic Electrons by Elec-
 704 tromagnetic Ion Cyclotron Waves in Earth's Radiation Belts. *Phys Rev. Lett.*,
 705 *129*(13), 135101. doi: 10.1103/PhysRevLett.129.135101
 706 An, Z., Wu, Y., & Tao, X. (2022). Electron dynamics in a chorus wave field
 707 generated from particle-in-cell simulations. *Geophys. Res. Lett.*, *49*(3),
 708 e2022GL097778. doi: 10.1029/2022GL097778
 709 Angelopoulos, V., Cruce, P., Drozdov, A., Grimes, E. W., Hatzigeorgiu, N., King,
 710 D. A., ... Schroeder, P. (2019, January). The Space Physics Environ-
 711 ment Data Analysis System (SPEDAS). *Space Sci. Rev.*, *215*, 9. doi:
 712 10.1007/s11214-018-0576-4
 713 Angelopoulos, V., Tsai, E., Bingley, L., Shaffer, C., Turner, D. L., Runov, A., ...
 714 Zhang, G. Y. (2020, July). The ELFING Mission. *Space Sci. Rev.*, *216*(5), 103.
 715 doi: 10.1007/s11214-020-00721-7
 716 Angelopoulos, V., Zhang, X. J., Artemyev, A. V., Mourenas, D., Tsai, E., Wilkins,
 717 C., ... Zarifian, A. (2023, August). Energetic Electron Precipitation Driven by
 718 Electromagnetic Ion Cyclotron Waves from ELFING's Low Altitude Perspective.
 719 *Space Sci. Rev.*, *219*(5), 37. doi: 10.1007/s11214-023-00984-w
 720 Artemyev, A. V., Agapitov, O., Mourenas, D., Krasnoselskikh, V., Shastun, V., &
 721 Mozer, F. (2016, April). Oblique Whistler-Mode Waves in the Earth's Inner
 722 Magnetosphere: Energy Distribution, Origins, and Role in Radiation Belt Dy-
 723 namics. *Space Sci. Rev.*, *200*(1-4), 261-355. doi: 10.1007/s11214-016-0252-5
 724 Artemyev, A. V., Angelopoulos, V., Zhang, X. J., Runov, A., Petrukovich, A., Naka-
 725 mura, R., ... Wilkins, C. (2022, October). Thinning of the Magnetotail Cur-
 726 rent Sheet Inferred From Low-Altitude Observations of Energetic Electrons.
 727 *Journal of Geophysical Research (Space Physics)*, *127*(10), e2022JA030705.
 728 doi: 10.1029/2022JA030705
 729 Artemyev, A. V., & Mourenas, D. (2020, March). On Whistler Mode Wave Relation
 730 to Electron Field-Aligned Plateau Populations. *Journal of Geophysical Re-*
 731 *search (Space Physics)*, *125*(3), e27735. doi: 10.1029/2019JA027735
 732 Artemyev, A. V., Mourenas, D., Agapitov, O. V., & Krasnoselskikh, V. V. (2013,
 733 April). Parametric validations of analytical lifetime estimates for radiation belt

- 734 electron diffusion by whistler waves. *Annales Geophysicae*, *31*, 599-624. doi:
735 10.5194/angeo-31-599-2013
- 736 Artemyev, A. V., Zhang, X. J., Angelopoulos, V., Mourenas, D., Vainchtein, D.,
737 Shen, Y., ... Runov, A. (2020, September). Ionosphere Feedback to Elec-
738 tron Scattering by Equatorial Whistler Mode Waves. *Journal of Geophysical*
739 *Research (Space Physics)*, *125*(9), e28373. doi: 10.1029/2020JA028373
- 740 Aryan, H., Agapitov, O. V., Artemyev, A., Mourenas, D., Balikhin, M. A., Boynton,
741 R., & Bortnik, J. (2020, August). Outer Radiation Belt Electron Lifetime
742 Model Based on Combined Van Allen Probes and Cluster VLF Measure-
743 ments. *Journal of Geophysical Research (Space Physics)*, *125*(8), e28018. doi:
744 10.1029/2020JA028018
- 745 Bell, T. F., Inan, U. S., Bortnik, J., & Scudder, J. D. (2002, August). The Landau
746 damping of magnetospherically reflected whistlers within the plasmasphere.
747 *Geophys. Res. Lett.*, *29*, 1733. doi: 10.1029/2002GL014752
- 748 Bezanson, J., Edelman, A., Karpinski, S., & Shah, V. B. (2017). Julia: A fresh ap-
749 proach to numerical computing. *SIAM review*, *59*(1), 65–98. Retrieved from
750 <https://doi.org/10.1137/141000671>
- 751 Blake, J. B., & O'Brien, T. P. (2016, April). Observations of small-scale latitudinal
752 structure in energetic electron precipitation. *Journal of Geophysical Research*
753 *(Space Physics)*, *121*(4), 3031-3035. doi: 10.1002/2015JA021815
- 754 Blum, L. W., Halford, A., Millan, R., Bonnell, J. W., Goldstein, J., Usanova, M.,
755 ... Li, X. (2015, July). Observations of coincident EMIC wave activity and
756 duskside energetic electron precipitation on 18-19 January 2013. *Geophys.*
757 *Res. Lett.*, *42*, 5727-5735. doi: 10.1002/2015GL065245
- 758 Blum, L. W., Li, X., & Denton, M. (2015, May). Rapid MeV electron precipitation
759 as observed by SAMPEX/HILT during high-speed stream-driven storms. *J.*
760 *Geophys. Res.*, *120*, 3783-3794. doi: 10.1002/2014JA020633
- 761 Bortnik, J., & Thorne, R. M. (2007, March). The dual role of ELF/VLF chorus
762 waves in the acceleration and precipitation of radiation belt electrons. *Journal*
763 *of Atmospheric and Solar-Terrestrial Physics*, *69*, 378-386. doi: 10.1016/j.jastp
764 .2006.05.030
- 765 Bortnik, J., Thorne, R. M., & Inan, U. S. (2008, November). Nonlinear interac-
766 tion of energetic electrons with large amplitude chorus. *Geophys. Res. Lett.*,
767 *35*, 21102. doi: 10.1029/2008GL035500
- 768 Bortnik, J., Thorne, R. M., Meredith, N. P., & Santolik, O. (2007, August). Ray
769 tracing of penetrating chorus and its implications for the radiation belts. *Geo-*
770 *phys. Res. Lett.*, *34*, L15109. doi: 10.1029/2007GL030040
- 771 Boynton, R. J., Mourenas, D., & Balikhin, M. A. (2016, September). Electron
772 flux dropouts at Geostationary Earth Orbit: Occurrences, magnitudes, and
773 main driving factors. *Journal of Geophysical Research (Space Physics)*, *121*,
774 8448-8461. doi: 10.1002/2016JA022916
- 775 Boynton, R. J., Mourenas, D., & Balikhin, M. A. (2017, November). Electron Flux
776 Dropouts at $L \sim 4.2$ From Global Positioning System Satellites: Occurrences,
777 Magnitudes, and Main Driving Factors. *Journal of Geophysical Research*
778 *(Space Physics)*, *122*, 11. doi: 10.1002/2017JA024523
- 779 Breneman, A. W., Crew, A., Sample, J., Klumpar, D., Johnson, A., Agapitov,
780 O., ... Kletzing, C. A. (2017, November). Observations Directly Link-
781 ing Relativistic Electron Microbursts to Whistler Mode Chorus: Van Allen
782 Probes and FIREBIRD II. *Geophys. Res. Lett.*, *44*(22), 11,265-11,272. doi:
783 10.1002/2017GL075001
- 784 Breuillard, H., Zaliznyak, Y., Krasnoselskikh, V., Agapitov, O., Artemyev, A., &
785 Rolland, G. (2012). Chorus wave-normal statistics in the Earth's radia-
786 tion belts from ray tracing technique. *Ann. Geophys.*, *30*, 1223-1233. doi:
787 10.5194/angeo-30-1223-2012
- 788 Büchner, J., & Zelenyi, L. M. (1989, September). Regular and chaotic charged

- 789 particle motion in magnetotaillike field reversals. I - Basic theory of trapped
790 motion. *J. Geophys. Res.*, *94*, 11821-11842. doi: 10.1029/JA094iA09p11821
- 791 Bunch, N. L., Spasojevic, M., Shprits, Y. Y., Gu, X., & Foust, F. (2013, April). The
792 spectral extent of chorus in the off-equatorial magnetosphere. *J. Geophys.*
793 *Res.*, *118*, 1700-1705. doi: 10.1029/2012JA018182
- 794 Capannolo, L., Li, W., Ma, Q., Chen, L., Shen, X. C., Spence, H. E., ... Redmon,
795 R. J. (2019, November). Direct Observation of Subrelativistic Electron Pre-
796 cipitation Potentially Driven by EMIC Waves. *Geophys. Res. Lett.*, *46*(22),
797 12,711-12,721. doi: 10.1029/2019GL084202
- 798 Capannolo, L., Li, W., Ma, Q., Qin, M., Shen, X. C., Angelopoulos, V., ...
799 Hanzelka, M. (2023). Electron precipitation observed by elfin using proton
800 precipitation as a proxy for electromagnetic ion cyclotron (emic) waves. *Geo-*
801 *physical Research Letters*. doi: <https://doi.org/10.1029/2023GL103519>
- 802 Chen, L., Thorne, R. M., Li, W., & Bortnik, J. (2013, March). Modeling the wave
803 normal distribution of chorus waves. *J. Geophys. Res.*, *118*, 1074-1088. doi:
804 10.1029/2012JA018343
- 805 Chen, L., Zhang, X.-J., Artemyev, A., Angelopoulos, V., Tsai, E., Wilkins, C., &
806 Horne, R. B. (2022, March). Ducted Chorus Waves Cause Sub-Relativistic and
807 Relativistic Electron Microbursts. *Geophys. Res. Lett.*, *49*(5), e97559. doi:
808 10.1029/2021GL097559
- 809 Chen, L., Zhang, X.-J., Artemyev, A., Zheng, L., Xia, Z., Breneman, A. W., &
810 Horne, R. B. (2021, October). Electron microbursts induced by nonducted
811 chorus waves. *Frontiers in Astronomy and Space Sciences*, *8*, 163. doi:
812 10.3389/fspas.2021.745927
- 813 Chen, R., Gao, X., Lu, Q., & Wang, S. (2019, November). Unraveling the Cor-
814 relation Between Chorus Wave and Electron Beam-Like Distribution in the
815 Earth's Magnetosphere. *Geophys. Res. Lett.*, *46*(21), 11,671-11,678. doi:
816 10.1029/2019GL085108
- 817 Demekhov, A. G., Trakhtengerts, V. Y., Rycroft, M. J., & Nunn, D. (2006, Decem-
818 ber). Electron acceleration in the magnetosphere by whistler-mode waves
819 of varying frequency. *Geomagnetism and Aeronomy*, *46*, 711-716. doi:
820 10.1134/S0016793206060053
- 821 Drozdov, A. Y., Shprits, Y. Y., Usanova, M. E., Aseev, N. A., Kellerman, A. C.,
822 & Zhu, H. (2017, August). EMIC wave parameterization in the long-
823 term VERB code simulation. *J. Geophys. Res.*, *122*, 8488-8501. doi:
824 10.1002/2017JA024389
- 825 Fu, X., Cowee, M. M., Friedel, R. H., Funsten, H. O., Gary, S. P., Hospodarsky,
826 G. B., ... Winske, D. (2014, October). Whistler anisotropy instabilities as the
827 source of banded chorus: Van Allen Probes observations and particle-in-cell
828 simulations. *Journal of Geophysical Research (Space Physics)*, *119*, 8288-8298.
829 doi: 10.1002/2014JA020364
- 830 Gabrielse, C., Angelopoulos, V., Runov, A., & Turner, D. L. (2014, April). Statisti-
831 cal characteristics of particle injections throughout the equatorial magnetotail.
832 *J. Geophys. Res.*, *119*, 2512-2535. doi: 10.1002/2013JA019638
- 833 Gan, L., Artemyev, A., Li, W., Zhang, X.-J., Ma, Q., Mourenas, D., ... Wilkins,
834 C. (2023). Bursty energetic electron precipitation by high-order reso-
835 nance with very-oblique whistler-mode waves. *Geophys. Res. Lett.* doi:
836 10.1029/2022GL101920
- 837 Gan, L., Li, W., Ma, Q., Artemyev, A. V., & Albert, J. M. (2022). Dependence of
838 nonlinear effects on whistler-mode wave bandwidth and amplitude: A perspec-
839 tive from diffusion coefficients. *J. Geophys. Res.*, *127*, e2021JA030063. doi:
840 10.1029/2021JA030063
- 841 Gendrin, R. (1961, August). Le guidage des whistlers par le champ magnetique.
842 *Planetary Space Science*, *5*, 274. doi: 10.1016/0032-0633(61)90096-4
- 843 Glauert, S. A., & Horne, R. B. (2005, April). Calculation of pitch angle and energy

- 844 diffusion coefficients with the PADIE code. *J. Geophys. Res.*, *110*, 4206. doi:
845 10.1029/2004JA010851
- 846 Grach, V. S., Artemyev, A. V., Demekhov, A. G., Zhang, X.-J., Bortnik, J., An-
847 gelopoulos, V., . . . Roberts, O. W. (2022, September). Relativistic Electron
848 Precipitation by EMIC Waves: Importance of Nonlinear Resonant Effects.
849 *Geophys. Res. Lett.*, *49*(17), e99994. doi: 10.1029/2022GL099994
- 850 Hanzelka, M., & Santolík, O. (2019, June). Effects of Ducting on Whistler Mode
851 Chorus or Exohiss in the Outer Radiation Belt. *Geophys. Res. Lett.*, *46*(11),
852 5735-5745. doi: 10.1029/2019GL083115
- 853 Hanzelka, M., & Santolík, O. (2022, December). Effects of Field-Aligned Cold
854 Plasma Density Filaments on the Fine Structure of Chorus. *Geophys. Res.*
855 *Lett.*, *49*(24), e2022GL101654. doi: 10.1029/2022GL101654
- 856 Horne, R. B., Glauert, S. A., Meredith, N. P., Boscher, D., Maget, V., Heynderickx,
857 D., & Pitchford, D. (2013, April). Space weather impacts on satellites and
858 forecasting the Earth's electron radiation belts with SPACECAST. *Space*
859 *Weather*, *11*, 169-186. doi: 10.1002/swe.20023
- 860 Hosseini, P., Agapitov, O., Harid, V., & Gołkowski, M. (2021, March). Evidence of
861 Small Scale Plasma Irregularity Effects on Whistler Mode Chorus Propagation.
862 *Geophys. Res. Lett.*, *48*(5), e92850. doi: 10.1029/2021GL092850
- 863 Hsieh, Y.-K., & Omura, Y. (2017, January). Nonlinear dynamics of electrons inter-
864 acting with oblique whistler mode chorus in the magnetosphere. *J. Geophys.*
865 *Res.*, *122*, 675-694. doi: 10.1002/2016JA023255
- 866 Imhof, W. L., Reagan, J. B., & Gaines, E. E. (1977, November). Fine-scale spa-
867 tial structure in the pitch angle distributions of energetic particles near
868 the midnight trapping boundary. *J. Geophys. Res.*, *82*, 5215-5221. doi:
869 10.1029/JA082i032p05215
- 870 Jun, C. W., Yue, C., Bortnik, J., Lyons, L. R., Nishimura, Y., & Kletzing, C. (2019,
871 Mar). EMIC Wave Properties Associated With and Without Injections in
872 The Inner Magnetosphere. *Journal of Geophysical Research (Space Physics)*,
873 *124*(3), 2029-2045. doi: 10.1029/2018JA026279
- 874 Kang, N., & Bortnik, J. (2022, March). Structure of Energy Precipitation Induced
875 by Superbolt-Lightning Generated Whistler Waves. *Geophys. Res. Lett.*,
876 *49*(5), e2022GL097770. doi: 10.1029/2022GL097770
- 877 Kang, N., Bortnik, J., Zhang, X., Claudepierre, S., & Shi, X. (2022, Decem-
878 ber). Relativistic Microburst Scale Size Induced by a Single Point-Source
879 Chorus Element. *Geophys. Res. Lett.*, *49*(23), e2022GL100841. doi:
880 10.1029/2022GL100841
- 881 Katoh, Y., Omura, Y., & Summers, D. (2008, November). Rapid energization of
882 radiation belt electrons by nonlinear wave trapping. *Annales Geophysicae*, *26*,
883 3451-3456. doi: 10.5194/angeo-26-3451-2008
- 884 Ke, Y., Chen, L., Gao, X., Lu, Q., Wang, X., Chen, R., . . . Wang, S. (2021, April).
885 Whistler Mode Waves Trapped by Density Irregularities in the Earth's Magne-
886 tosphere. *Geophys. Res. Lett.*, *48*(7), e92305. doi: 10.1029/2020GL092305
- 887 Ke, Y., Gao, X., Lu, Q., Wang, X., Chen, R., Chen, H., & Wang, S. (2022,
888 February). Deformation of Electron Distributions Due to Landau Trap-
889 ping by the Whistler-Mode Wave. *Geophys. Res. Lett.*, *49*(3), e96428. doi:
890 10.1029/2021GL096428
- 891 Ke, Y., Gao, X., Lu, Q., Wang, X., & Wang, S. (2017). Generation of rising-tone
892 chorus in a two-dimensional mirror field by using the general curvilinear pic
893 code. *J. Geophys. Res.*. Retrieved from [http://dx.doi.org/10.1002/](http://dx.doi.org/10.1002/2017JA024178)
894 [2017JA024178](http://dx.doi.org/10.1002/2017JA024178) doi: 10.1002/2017JA024178
- 895 Kennel, C. F., & Engelmann, F. (1966, November). Velocity Space Diffusion from
896 Weak Plasma Turbulence in a Magnetic Field. *Physics of Fluids*, *9*, 2377-2388.
897 doi: 10.1063/1.1761629
- 898 Kennel, C. F., & Petschek, H. E. (1966, January). Limit on Stably Trapped Particle

- 899 Fluxes. *J. Geophys. Res.*, *71*, 1-28.
- 900 Khazanov, G. V., Glocer, A., & Himwich, E. W. (2014, Jan). Magnetosphere-
 901 ionosphere energy interchange in the electron diffuse aurora. *Journal of*
 902 *Geophysical Research (Space Physics)*, *119*(1), 171-184. doi: 10.1002/
 903 2013JA019325
- 904 Khazanov, G. V., Robinson, R. M., Zesta, E., Sibeck, D. G., Chu, M., & Grubbs,
 905 G. A. (2018, July). Impact of Precipitating Electrons and Magnetosphere-
 906 Ionosphere Coupling Processes on Ionospheric Conductance. *Space Weather*,
 907 *16*(7), 829-837. doi: 10.1029/2018SW001837
- 908 Kim, H., Schiller, Q., Engebretson, M. J., Noh, S., Kuzichev, I., Lanzerotti, L. J.,
 909 ... Fromm, T. (2021, February). Observations of Particle Loss due to Injec-
 910 tion Associated Electromagnetic Ion Cyclotron Waves. *Journal of Geophysical*
 911 *Research (Space Physics)*, *126*(2), e28503. doi: 10.1029/2020JA028503
- 912 Kitahara, M., & Katoh, Y. (2019, Jul). Anomalous Trapping of Low Pitch Angle
 913 Electrons by Coherent Whistler Mode Waves. *J. Geophys. Res.*, *124*(7), 5568-
 914 5583. doi: 10.1029/2019JA026493
- 915 Kong, Z., Gao, X., Chen, H., Lu, Q., Chen, R., Ke, Y., & Wang, S. (2021, Novem-
 916 ber). The Correlation Between Whistler Mode Waves and Electron Beam-
 917 Like Distribution: Test Particle Simulations and THEMIS Observations.
 918 *Journal of Geophysical Research (Space Physics)*, *126*(11), e29834. doi:
 919 10.1029/2021JA029834
- 920 Lam, M. M., Horne, R. B., Meredith, N. P., Glauert, S. A., Moffat-Griffin, T., &
 921 Green, J. C. (2010). Origin of energetic electron precipitation; 30 keV into the
 922 atmosphere. *Journal of Geophysical Research: Space Physics*, *115*(A4).
- 923 Li, W., & Hudson, M. K. (2019, Nov). Earth's Van Allen Radiation Belts: From
 924 Discovery to the Van Allen Probes Era. *Journal of Geophysical Research*
 925 *(Space Physics)*, *124*(11), 8319-8351. doi: 10.1029/2018JA025940
- 926 Li, W., Mourenas, D., Artemyev, A. V., Bortnik, J., Thorne, R. M., Kletzing, C. A.,
 927 ... Spence, H. E. (2016, September). Unraveling the excitation mechanisms of
 928 highly oblique lower band chorus waves. *Geophys. Res. Lett.*, *43*, 8867-8875.
 929 doi: 10.1002/2016GL070386
- 930 Li, W., Ni, B., Thorne, R. M., Bortnik, J., Green, J. C., Kletzing, C. A., ... Hoso-
 931 podarsky, G. B. (2013, September). Constructing the global distribution of
 932 chorus wave intensity using measurements of electrons by the POES satellites
 933 and waves by the Van Allen Probes. *Geophys. Res. Lett.*, *40*, 4526-4532. doi:
 934 10.1002/grl.50920
- 935 Li, W., Santolik, O., Bortnik, J., Thorne, R. M., Kletzing, C. A., Kurth, W. S., &
 936 Hospodarsky, G. B. (2016, May). New chorus wave properties near the equator
 937 from Van Allen Probes wave observations. *Geophys. Res. Lett.*, *43*, 4725-4735.
 938 doi: 10.1002/2016GL068780
- 939 Li, W., Thorne, R. M., Bortnik, J., Nishimura, Y., Angelopoulos, V., Chen, L.,
 940 ... Bonnell, J. W. (2010, December). Global distributions of suprathermal
 941 electrons observed on THEMIS and potential mechanisms for access into the
 942 plasmasphere. *J. Geophys. Res.*, *115*, 0. doi: 10.1029/2010JA015687
- 943 Li, W., Thorne, R. M., Ma, Q., Ni, B., Bortnik, J., Baker, D. N., ... Claudepierre,
 944 S. G. (2014, June). Radiation belt electron acceleration by chorus waves
 945 during the 17 March 2013 storm. *J. Geophys. Res.*, *119*, 4681-4693. doi:
 946 10.1002/2014JA019945
- 947 Li, W., Thorne, R. M., Nishimura, Y., Bortnik, J., Angelopoulos, V., McFadden,
 948 J. P., ... Auster, U. (2010, June). THEMIS analysis of observed equatorial
 949 electron distributions responsible for the chorus excitation. *J. Geophys. Res.*,
 950 *115*. doi: 10.1029/2009JA014845
- 951 Lorentzen, K. R., Blake, J. B., Inan, U. S., & Bortnik, J. (2001, April). Obser-
 952 vations of relativistic electron microbursts in association with VLF chorus. *J.*
 953 *Geophys. Res.*, *106*(A4), 6017-6028. doi: 10.1029/2000JA003018

- 954 Lyons, L. R., Thorne, R. M., & Kennel, C. F. (1972). Pitch-angle diffusion of radi-
 955 ation belt electrons within the plasmasphere. *J. Geophys. Res.*, *77*, 3455-3474.
 956 doi: 10.1029/JA077i019p03455
- 957 Ma, Q., Artemyev, A. V., Mourenas, D., Li, W., Thorne, R. M., Kletzing, C. A., ...
 958 Wygant, J. (2017, December). Very Oblique Whistler Mode Propagation in
 959 the Radiation Belts: Effects of Hot Plasma and Landau Damping. *Geophys.*
 960 *Res. Lett.*, *44*(24), 12,057-12,066. doi: 10.1002/2017GL075892
- 961 Ma, Q., Gu, W., Claudepierre, S. G., Li, W., Bortnik, J., Hua, M., & Shen, X. C.
 962 (2022, June). Electron Scattering by Very-Low-Frequency and Low-Frequency
 963 Waves From Ground Transmitters in the Earth's Inner Radiation Belt and Slot
 964 Region. *Journal of Geophysical Research (Space Physics)*, *127*(6), e30349. doi:
 965 10.1029/2022JA030349
- 966 Ma, Q., Li, W., Bortnik, J., Thorne, R. M., Chu, X., Ozeke, L. G., ... Claudepierre,
 967 S. G. (2018, March). Quantitative Evaluation of Radial Diffusion and Local
 968 Acceleration Processes During GEM Challenge Events. *Journal of Geophysical*
 969 *Research (Space Physics)*, *123*(3), 1938-1952. doi: 10.1002/2017JA025114
- 970 Ma, Q., Li, W., Thorne, R. M., Ni, B., Kletzing, C. A., Kurth, W. S., ... An-
 971 gelopoulos, V. (2015, February). Modeling inward diffusion and slow decay
 972 of energetic electrons in the Earth's outer radiation belt. *Geophys. Res. Lett.*,
 973 *42*, 987-995. doi: 10.1002/2014GL062977
- 974 Ma, Q., Ni, B., Tao, X., & Thorne, R. M. (2012, April). Evolution of the plasma
 975 sheet electron pitch angle distribution by whistler-mode chorus waves
 976 in non-dipole magnetic fields. *Annales Geophysicae*, *30*, 751-760. doi:
 977 10.5194/angeo-30-751-2012
- 978 Malaspina, D. M., Ukhorskiy, A., Chu, X., & Wygant, J. (2018, April). A Cen-
 979 sus of Plasma Waves and Structures Associated With an Injection Front
 980 in the Inner Magnetosphere. *J. Geophys. Res.*, *123*, 2566-2587. doi:
 981 10.1002/2017JA025005
- 982 Maxworth, A. S., & Golkowski, M. (2017). Magnetospheric whistler mode
 983 ray tracing in a warm background plasma with finite electron and ion
 984 temperature. *J. Geophys. Res.*, *122*(7), 7323-7335. Retrieved from
 985 <http://dx.doi.org/10.1002/2016JA023546> doi: 10.1002/2016JA023546
- 986 Meredith, N. P., Horne, R. B., & Anderson, R. R. (2001, July). Substorm de-
 987 pendence of chorus amplitudes: Implications for the acceleration of elec-
 988 trons to relativistic energies. *J. Geophys. Res.*, *106*, 13165-13178. doi:
 989 10.1029/2000JA900156
- 990 Meredith, N. P., Horne, R. B., Shen, X.-C., Li, W., & Bortnik, J. (2020). Global
 991 model of whistler mode chorus in the near-equatorial region ($|\lambda_m| < 18^\circ$).
 992 *Geophys. Res. Lett.*, *47*, e2020GL087311. doi: 10.1029/2020GL087311
- 993 Meredith, N. P., Horne, R. B., Sicard-Piet, A., Boscher, D., Yearby, K. H., Li, W., &
 994 Thorne, R. M. (2012, October). Global model of lower band and upper band
 995 chorus from multiple satellite observations. *J. Geophys. Res.*, *117*, 10225. doi:
 996 10.1029/2012JA017978
- 997 Meredith, N. P., Horne, R. B., Thorne, R. M., & Anderson, R. R. (2003, August).
 998 Favored regions for chorus-driven electron acceleration to relativistic energies
 999 in the Earth's outer radiation belt. *Geophys. Res. Lett.*, *30*(16), 160000-1. doi:
 1000 10.1029/2003GL017698
- 1001 Millan, R. M., & Baker, D. N. (2012, November). Acceleration of Particles to High
 1002 Energies in Earth's Radiation Belts. *Space Sci. Rev.*, *173*, 103-131. doi: 10
 1003 .1007/s11214-012-9941-x
- 1004 Millan, R. M., & Thorne, R. M. (2007, March). Review of radiation belt relativistic
 1005 electron losses. *Journal of Atmospheric and Solar-Terrestrial Physics*, *69*, 362-
 1006 377. doi: 10.1016/j.jastp.2006.06.019
- 1007 Min, K., Liu, K., & Li, W. (2014, July). Signatures of electron Landau resonant
 1008 interactions with chorus waves from THEMIS observations. *J. Geophys. Res.*,

- 1009 119, 5551-5560. doi: 10.1002/2014JA019903
- 1010 Mourenas, D., Artemyev, A. V., Agapitov, O. V., & Krasnoselskikh, V. (2014,
1011 April). Consequences of geomagnetic activity on energization and loss of radi-
1012 ation belt electrons by oblique chorus waves. *J. Geophys. Res.*, *119*, 2775-2796.
1013 doi: 10.1002/2013JA019674
- 1014 Mourenas, D., Artemyev, A. V., Agapitov, O. V., Krasnoselskikh, V., & Li, W.
1015 (2014, December). Approximate analytical solutions for the trapped electron
1016 distribution due to quasi-linear diffusion by whistler mode waves. *J. Geophys.*
1017 *Res.*, *119*, 9962-9977. doi: 10.1002/2014JA020443
- 1018 Mourenas, D., Artemyev, A. V., Agapitov, O. V., Krasnoselskikh, V., & Mozer, F. S.
1019 (2015). Very oblique whistler generation by low-energy electron streams. *J.*
1020 *Geophys. Res.*, *120*, 3665-3683. doi: 10.1002/2015JA021135
- 1021 Mourenas, D., Artemyev, A. V., Ripoll, J.-F., Agapitov, O. V., & Krasnoselskikh,
1022 V. V. (2012). Timescales for electron quasi-linear diffusion by parallel and
1023 oblique lower-band Chorus waves. *J. Geophys. Res.*, *117*, A06234. doi:
1024 10.1029/2012JA017717
- 1025 Mourenas, D., Artemyev, A. V., Zhang, X. J., & Angelopoulos, V. (2022, Novem-
1026 ber). Extreme Energy Spectra of Relativistic Electron Flux in the Outer
1027 Radiation Belt. *Journal of Geophysical Research (Space Physics)*, *127*(11),
1028 e2022JA031038. doi: 10.1029/2022JA031038
- 1029 Mourenas, D., Artemyev, A. V., Zhang, X. J., & Angelopoulos, V. (2023, Au-
1030 gust). Upper Limit on Outer Radiation Belt Electron Flux Based on Dynam-
1031 ical Equilibrium. *Journal of Geophysical Research (Space Physics)*, *128*(8),
1032 e2023JA031676. doi: 10.1029/2023JA031676
- 1033 Mourenas, D., Artemyev, A. V., Zhang, X. J., Angelopoulos, V., Tsai, E., &
1034 Wilkins, C. (2021, November). Electron Lifetimes and Diffusion Rates
1035 Inferred From ELFIN Measurements at Low Altitude: First Results.
1036 *Journal of Geophysical Research (Space Physics)*, *126*(11), e29757. doi:
1037 10.1029/2021JA029757
- 1038 Mourenas, D., & Ripoll, J.-F. (2012). Analytical estimates of quasi-linear diffusion
1039 coefficients and electron lifetimes in the inner radiation belt. *J. Geophys. Res.*,
1040 *117*, A01204. doi: 10.1029/2011JA016985
- 1041 Mourenas, D., Zhang, X. J., Nunn, D., Artemyev, A. V., Angelopoulos, V., Tsai, E.,
1042 & Wilkins, C. (2022, May). Short Chorus Wave Packets: Generation Within
1043 Chorus Elements, Statistics, and Consequences on Energetic Electron Precipi-
1044 tation. *Journal of Geophysical Research (Space Physics)*, *127*(5), e30310. doi:
1045 10.1029/2022JA030310
- 1046 Mozer, F. S., Agapitov, O., Artemyev, A., Drake, J. F., Krasnoselskikh, V., Lejosne,
1047 S., & Vasko, I. (2015). Time domain structures: What and where they are,
1048 what they do, and how they are made. *Geophys. Res. Lett.*, *42*, 3627-3638.
1049 doi: 10.1002/2015GL063946
- 1050 Ni, B., Li, W., Thorne, R. M., Bortnik, J., Green, J. C., Kletzing, C. A., . . . Soria-
1051 Santacruz Pich, M. (2014, July). A novel technique to construct the global
1052 distribution of whistler mode chorus wave intensity using low-altitude POES
1053 electron data. *J. Geophys. Res.*, *119*, 5685-5699. doi: 10.1002/2014JA019935
- 1054 Ni, B., Thorne, R. M., Meredith, N. P., Shprits, Y. Y., & Horne, R. B. (2011, Octo-
1055 ber). Diffuse auroral scattering by whistler mode chorus waves: Dependence on
1056 wave normal angle distribution. *J. Geophys. Res.*, *116*, 10207. doi: 10.1029/
1057 2011JA016517
- 1058 Ni, B., Thorne, R. M., Shprits, Y. Y., & Bortnik, J. (2008, June). Resonant
1059 scattering of plasma sheet electrons by whistler-mode chorus: Contribu-
1060 tion to diffuse auroral precipitation. *Geophys. Res. Lett.*, *35*, 11106. doi:
1061 10.1029/2008GL034032
- 1062 O'Brien, T. P., Looper, M. D., & Blake, J. B. (2004, February). Quantification of
1063 relativistic electron microburst losses during the GEM storms. *Geophys. Res.*

- 1064 *Lett.*, 31(4), L04802. doi: 10.1029/2003GL018621
- 1065 O'Brien, T. P., & Moldwin, M. B. (2003, February). Empirical plasmopause
1066 models from magnetic indices. *Geophys. Res. Lett.*, 30, 1152. doi:
1067 10.1029/2002GL016007
- 1068 Olifer, L., Mann, I. R., Boyd, A. J., Ozeke, L. G., & Choi, D. (2018, May). On
1069 the Role of Last Closed Drift Shell Dynamics in Driving Fast Losses and Van
1070 Allen Radiation Belt Extinction. *J. Geophys. Res.*, 123, 3692-3703. doi:
1071 10.1029/2018JA025190
- 1072 Omura, Y., Furuya, N., & Summers, D. (2007, June). Relativistic turning ac-
1073 celeration of resonant electrons by coherent whistler mode waves in a dipole
1074 magnetic field. *J. Geophys. Res.*, 112, 6236. doi: 10.1029/2006JA012243
- 1075 Omura, Y., Miyashita, Y., Yoshikawa, M., Summers, D., Hikishima, M., Ebihara, Y.,
1076 & Kubota, Y. (2015, November). Formation process of relativistic electron flux
1077 through interaction with chorus emissions in the Earth's inner magnetosphere.
1078 *J. Geophys. Res.*, 120, 9545-9562. doi: 10.1002/2015JA021563
- 1079 Orlova, K. G., & Shprits, Y. Y. (2011, September). On the bounce-averaging of scat-
1080 tering rates and the calculation of bounce period. *Physics of Plasmas*, 18(9),
1081 092904. doi: 10.1063/1.3638137
- 1082 Rackauckas, C., & Nie, Q. (2017). Differentialequations.jl—a performant and feature-
1083 rich ecosystem for solving differential equations in julia. *Journal of Open Re-
1084 search Software*, 5(1).
- 1085 Runov, A., Angelopoulos, V., Gabrielse, C., Liu, J., Turner, D. L., & Zhou, X.-Z.
1086 (2015, June). Average thermodynamic and spectral properties of plasma in
1087 and around dipolarizing flux bundles. *J. Geophys. Res.*, 120, 4369-4383. doi:
1088 10.1002/2015JA021166
- 1089 Sauer, K., Baumgaerte, K., & Sydora, R. D. (2020). Gap formation around $\omega_e/2$
1090 and generation of low-band whistler waves by landau-resonant electrons in
1091 the magnetosphere: Predictions from dispersion theory. *Earth and Planetary
1092 Physics*, 4, 138. Retrieved from [http://eppcgs.xml-journal.net//article/
1093 id/3c6a82bf-66b3-436e-94ce-bc744f2e3c29](http://eppcgs.xml-journal.net//article/id/3c6a82bf-66b3-436e-94ce-bc744f2e3c29) doi: 10.26464/epp2020020
- 1094 Sergeev, V. A., Sazhina, E. M., Tsyganenko, N. A., Lundblad, J. A., & Soraas, F.
1095 (1983, October). Pitch-angle scattering of energetic protons in the magne-
1096 totail current sheet as the dominant source of their isotropic precipitation
1097 into the nightside ionosphere. *Planetary Space Science*, 31, 1147-1155. doi:
1098 10.1016/0032-0633(83)90103-4
- 1099 Sheeley, B. W., Moldwin, M. B., Rassoul, H. K., & Anderson, R. R. (2001, Novem-
1100 ber). An empirical plasmasphere and trough density model: CRRES observa-
1101 tions. *J. Geophys. Res.*, 106, 25631-25642. doi: 10.1029/2000JA000286
- 1102 Shen, X.-C., Li, W., Capannolo, L., Ma, Q., Qin, M., Artemyev, A. V., ... Huang,
1103 S. (2023, April). Modulation of Energetic Electron Precipitation Driven
1104 by Three Types of Whistler Mode Waves. *Geophys. Res. Lett.*, 50(8),
1105 e2022GL101682. doi: 10.1029/2022GL101682
- 1106 Shen, Y., Chen, L., Zhang, X.-J., Artemyev, A., Angelopoulos, V., Cully, C. M., ...
1107 Horne, R. B. (2021, December). Conjugate Observation of Magnetospheric
1108 Chorus Propagating to the Ionosphere by Ducting. *Geophys. Res. Lett.*,
1109 48(23), e95933. doi: 10.1029/2021GL095933
- 1110 Shklyar, D. R. (2021, February). A Theory of Interaction Between Relativistic Elec-
1111 trons and Magnetospherically Reflected Whistlers. *Journal of Geophysical Re-
1112 search (Space Physics)*, 126(2), e28799. doi: 10.1029/2020JA028799
- 1113 Shklyar, D. R., & Matsumoto, H. (2009, April). Oblique Whistler-Mode Waves
1114 in the Inhomogeneous Magnetospheric Plasma: Resonant Interactions with
1115 Energetic Charged Particles. *Surveys in Geophysics*, 30, 55-104. doi:
1116 10.1007/s10712-009-9061-7
- 1117 Shprits, Y. Y., & Ni, B. (2009, November). Dependence of the quasi-linear scatter-
1118 ing rates on the wave normal distribution of chorus waves. *J. Geophys. Res.*,

- 1119 114, 11205. doi: 10.1029/2009JA014223
- 1120 Shprits, Y. Y., Subbotin, D. A., Meredith, N. P., & Elkington, S. R. (2008, Novem-
1121 ber). Review of modeling of losses and sources of relativistic electrons in the
1122 outer radiation belt II: Local acceleration and loss. *Journal of Atmospheric
1123 and Solar-Terrestrial Physics*, *70*, 1694-1713. doi: 10.1016/j.jastp.2008.06.014
- 1124 Shprits, Y. Y., Thorne, R. M., Friedel, R., Reeves, G. D., Fennell, J., Baker, D. N.,
1125 & Kanekal, S. G. (2006, November). Outward radial diffusion driven by losses
1126 at magnetopause. *J. Geophys. Res.*, *111*, 11214. doi: 10.1029/2006JA011657
- 1127 Shumko, M., Turner, D. L., O'Brien, T. P., Claudepierre, S. G., Sample, J., Hartley,
1128 D. P., ... Mitchell, D. G. (2018, August). Evidence of Microbursts Observed
1129 Near the Equatorial Plane in the Outer Van Allen Radiation Belt. *Geophys.
1130 Res. Lett.*, *45*(16), 8044-8053. doi: 10.1029/2018GL078451
- 1131 Stix, T. H. (1962). *The Theory of Plasma Waves*.
- 1132 Summers, D., Ma, C., Meredith, N. P., Horne, R. B., Thorne, R. M., & Anderson,
1133 R. R. (2004, January). Modeling outer-zone relativistic electron response to
1134 whistler-mode chorus activity during substorms. *Journal of Atmospheric and
1135 Solar-Terrestrial Physics*, *66*, 133-146. doi: 10.1016/j.jastp.2003.09.013
- 1136 Summers, D., & Ni, B. (2008, July). Effects of latitudinal distributions of particle
1137 density and wave power on cyclotron resonant diffusion rates of radiation belt
1138 electrons. *Earth, Planets, and Space*, *60*, 763-771.
- 1139 Summers, D., Ni, B., & Meredith, N. P. (2007, April). Timescales for radiation belt
1140 electron acceleration and loss due to resonant wave-particle interactions: 1.
1141 Theory. *J. Geophys. Res.*, *112*, 4206. doi: 10.1029/2006JA011801
- 1142 Tao, X., Bortnik, J., Albert, J. M., & Thorne, R. M. (2012, October). Comparison
1143 of bounce-averaged quasi-linear diffusion coefficients for parallel propagating
1144 whistler mode waves with test particle simulations. *J. Geophys. Res.*, *117*,
1145 10205. doi: 10.1029/2012JA017931
- 1146 Tao, X., Thorne, R. M., Li, W., Ni, B., Meredith, N. P., & Horne, R. B. (2011,
1147 April). Evolution of electron pitch angle distributions following injection
1148 from the plasma sheet. *J. Geophys. Res.*, *116*, A04229. doi: 10.1029/
1149 2010JA016245
- 1150 Thorne, R. M. (1980, March). The importance of energetic particle precipitation
1151 on the chemical composition of the middle atmosphere. *Pure and Applied Geo-
1152 physics*, *118*(1), 128-151. doi: 10.1007/BF01586448
- 1153 Thorne, R. M. (2010, November). Radiation belt dynamics: The importance of
1154 wave-particle interactions. *Geophys. Res. Lett.*, *37*(2), 22107. doi: 10.1029/
1155 2010GL044990
- 1156 Thorne, R. M., Li, W., Ni, B., Ma, Q., Bortnik, J., Chen, L., ... Kanekal, S. G.
1157 (2013, December). Rapid local acceleration of relativistic radiation-
1158 belt electrons by magnetospheric chorus. *Nature*, *504*, 411-414. doi:
1159 10.1038/nature12889
- 1160 Thorne, R. M., O'Brien, T. P., Shprits, Y. Y., Summers, D., & Horne, R. B. (2005,
1161 September). Timescale for MeV electron microburst loss during geomagnetic
1162 storms. *J. Geophys. Res.*, *110*, 9202. doi: 10.1029/2004JA010882
- 1163 Tsai, E. (2023, June). *ethantsai/nlwhistlers:jgr2023*. Zenodo. Retrieved from
1164 <https://doi.org/10.5281/zenodo.8083874> (Software) doi: 10.5281/zenodo
1165 .8083874
- 1166 Tsai, E., Artemyev, A., Angelopoulos, V., & Zhang, X.-J. (2023, August). In-
1167 vestigating Whistler-Mode Wave Intensity Along Field Lines Using Electron
1168 Precipitation Measurements. *Journal of Geophysical Research (Space Physics)*,
1169 *128*(8), e2023JA031578. doi: 10.1029/2023JA031578
- 1170 Tsai, E., Artemyev, A., Zhang, X.-J., & Angelopoulos, V. (2022, May). Relativistic
1171 Electron Precipitation Driven by Nonlinear Resonance With Whistler-Mode
1172 Waves. *Journal of Geophysical Research (Space Physics)*, *127*(5), e30338. doi:
1173 10.1029/2022JA030338

- 1174 Tsyganenko, N. A. (1989, January). A magnetospheric magnetic field model with
 1175 a warped tail current sheet. *Planetary Space Science*, *37*, 5-20. doi: 10.1016/
 1176 0032-0633(89)90066-4
- 1177 Turner, D. L., Angelopoulos, V., Li, W., Bortnik, J., Ni, B., Ma, Q., ... Rodriguez,
 1178 J. V. (2014, March). Competing source and loss mechanisms due to wave-
 1179 particle interactions in Earth's outer radiation belt during the 30 September to
 1180 3 October 2012 geomagnetic storm. *J. Geophys. Res.*, *119*, 1960-1979. doi:
 1181 10.1002/2014JA019770
- 1182 Turunen, E., Kero, A., Verronen, P. T., Miyoshi, Y., Oyama, S.-I., & Saito, S.
 1183 (2016). Mesospheric ozone destruction by high-energy electron precipitation as-
 1184 sociated with pulsating aurora. *Journal of Geophysical Research: Atmospheres*,
 1185 *121*(19), 11–852.
- 1186 Vainchtein, D., Zhang, X. J., Artemyev, A. V., Mourenas, D., Angelopoulos, V.,
 1187 & Thorne, R. M. (2018, October). Evolution of Electron Distribution
 1188 Driven by Nonlinear Resonances With Intense Field-Aligned Chorus Waves.
 1189 *Journal of Geophysical Research (Space Physics)*, *123*(10), 8149-8169. doi:
 1190 10.1029/2018JA025654
- 1191 Vasko, I. Y., Agapitov, O. V., Mozer, F. S., Artemyev, A. V., Drake, J. F., &
 1192 Kuzichev, I. V. (2017, January). Electron holes in the outer radiation belt:
 1193 Characteristics and their role in electron energization. *J. Geophys. Res.*, *122*,
 1194 120-135. doi: 10.1002/2016JA023083
- 1195 Vasko, I. Y., Agapitov, O. V., Mozer, F. S., Bonnell, J. W., Artemyev, A. V., Kras-
 1196 noselskikh, V. V., ... Hospodarsky, G. (2017, May). Electron-acoustic solitons
 1197 and double layers in the inner magnetosphere. *Geophys. Res. Lett.*, *44*, 4575-
 1198 4583. doi: 10.1002/2017GL074026
- 1199 Verkhoglyadova, O. P., Tsurutani, B. T., & Lakhina, G. S. (2010, September). Prop-
 1200 erties of obliquely propagating chorus. *Journal of Geophysical Research (Space*
 1201 *Physics)*, *115*(1), A00F19. doi: 10.1029/2009JA014809
- 1202 Walsh, B. M., Hull, A. J., Agapitov, O., Mozer, F. S., & Li, H. (2020). A census of
 1203 magnetospheric electrons from several ev to 30 kev. *Journal of Geophysical Re-*
 1204 *search: Space Physics*, *125*(5), e2019JA027577. Retrieved from [https://](https://agupubs.onlinelibrary.wiley.com/doi/abs/10.1029/2019JA027577)
 1205 agupubs.onlinelibrary.wiley.com/doi/abs/10.1029/2019JA027577
 1206 (e2019JA027577 10.1029/2019JA027577) doi: 10.1029/2019JA027577
- 1207 Wang, D., & Shprits, Y. Y. (2019, July). On How High-Latitude Chorus Waves Tip
 1208 the Balance Between Acceleration and Loss of Relativistic Electrons. *Geophys.*
 1209 *Res. Lett.*, *46*(14), 7945-7954. doi: 10.1029/2019GL082681
- 1210 Watt, C. E. J., Degeling, A. W., & Rankin, R. (2013, May). Constructing the fre-
 1211 quency and wave normal distribution of whistler-mode wave power. *J. Geo-*
 1212 *phys. Res.*, *118*, 1984-1991. doi: 10.1002/jgra.50231
- 1213 Wilkins, C., Angelopoulos, V., Runov, A., Artemyev, A., Zhang, X. J., Liu, J.,
 1214 & Tsai, E. (2023, October). Statistical Characteristics of the Electron
 1215 Isotropy Boundary. *Journal of Geophysical Research (Space Physics)*, *128*(10),
 1216 e2023JA031774. doi: 10.1029/2023JA031774
- 1217 Xiang, Z., Tu, W., Ni, B., Henderson, M. G., & Cao, X. (2018, August). A Statis-
 1218 tical Survey of Radiation Belt Dropouts Observed by Van Allen Probes. *Geo-*
 1219 *phys. Res. Lett.*, *45*, 8035-8043. doi: 10.1029/2018GL078907
- 1220 Xu, W., Marshall, R. A., Tyssøy, H. N., & Fang, X. (2020). A generalized method
 1221 for calculating atmospheric ionization by energetic electron precipitation. *Jour-*
 1222 *nal of Geophysical Research: Space Physics*, *125*(11), e2020JA028482.
- 1223 Yahnin, A. G., Yahnina, T. A., Raita, T., & Manninen, J. (2017, September).
 1224 Ground pulsation magnetometer observations conjugated with relativistic elec-
 1225 tron precipitation. *Journal of Geophysical Research (Space Physics)*, *122*(9),
 1226 9169-9182. doi: 10.1002/2017JA024249
- 1227 Yahnin, A. G., Yahnina, T. A., Semenova, N. V., Gvozdevsky, B. B., & Pashin,
 1228 A. B. (2016, September). Relativistic electron precipitation as seen by NOAA

- 1229 POES. *Journal of Geophysical Research (Space Physics)*, *121*(9), 8286-8299.
1230 doi: 10.1002/2016JA022765
- 1231 Zhang, X., Angelopoulos, V., Artemyev, A. V., & Liu, J. (2018, September).
1232 Whistler and Electron Firehose Instability Control of Electron Distributions in
1233 and Around Dipolarizing Flux Bundles. *Geophys. Res. Lett.*, *45*, 9380-9389.
1234 doi: 10.1029/2018GL079613
- 1235 Zhang, X.-J., Angelopoulos, V., Artemyev, A., Mourenas, D., Agapitov, O., Tsai,
1236 E., & Wilkins, C. (2023, January). Temporal Scales of Electron Precipitation
1237 Driven by Whistler-Mode Waves. *Journal of Geophysical Research (Space*
1238 *Physics)*, *128*(1), e2022JA031087. doi: 10.1029/2022JA031087
- 1239 Zhang, X.-J., Angelopoulos, V., Mourenas, D., Artemyev, A., Tsai, E., & Wilkins,
1240 C. (2022, May). Characteristics of Electron Microburst Precipitation Based
1241 on High-Resolution ELFIN Measurements. *Journal of Geophysical Research*
1242 *(Space Physics)*, *127*(5), e30509. doi: 10.1029/2022JA030509
- 1243 Zhang, X. J., Thorne, R., Artemyev, A., Mourenas, D., Angelopoulos, V., Bortnik,
1244 J., ... Hospodarsky, G. B. (2018, July). Properties of Intense Field-Aligned
1245 Lower-Band Chorus Waves: Implications for Nonlinear Wave-Particle Inter-
1246 actions. *Journal of Geophysical Research (Space Physics)*, *123*(7), 5379-5393.
1247 doi: 10.1029/2018JA025390